GROUND USER LOCALIZATION IN UAV-BASED WIRELESS NETWORKS: FROM CHANNEL CHARACTERIZATION TO SYSTEM DESIGN

A Dissertation
Presented to
The Academic Faculty

By

Jianqiao Cheng

Doctor of Philosophy in the
Brussels School of Engineering
BEAMS Department. Embedded Electronics

Université libre de Bruxelles (ULB)

January 2022

GROUND USER LOCALIZATION IN UAV-BASED WIRELESS NETWORKS: FROM CHANNEL CHARACTERIZATION TO SYSTEM DESIGN

Approved by:

Prof. Philippe De Doncker, Chair
Brussels School of Engineering
Université libre de Bruxelles

Prof. François Horlin, Secretary
Brussels School of Engineering
Université libre de Bruxelles

Prof. François Quitin, Supervisor
Brussels School of Engineering
Université libre de Bruxelles

Prof. Ke Guan, Co-supervisor
State Key Laboratory of Rail Traffic Control and Safety
Beijing Jiaotong University

Prof. Danping He
State Key Laboratory of Rail Traffic Control and Safety
Beijing Jiaotong University

Dr. Fernando Rosas
Department of Mathematics
Imperial College London

Abstract

Unmanned aerial vehicles (UAVs) are widely used in numerous applications thanks to their excellent mobility and fast deployments. One promising application is to let UAVs serve as flying base stations for providing reliable and cost-effective wireless communications. Such UAV-assisted communications are interesting for extending the range of an existing network, serving remote areas, or temporarily replacing cellular infrastructure in disaster scenarios. Unlike traditional terrestrial cellular networks where base stations are fixed to the ground and serve nearby cells, a UAV base station can be moved and deployed on demand. Its service coverage area is entirely dependent on the location of the UAV itself. This characteristic leads to a key challenge for UAV-assisted communications: the system should localize ground users before deploying UAV base stations to ensure optimal capacity and energy efficiency.

In this thesis, we focus on an advanced localization technique that has a great potential to help UAV platforms to localize ground targets based on their emitted radio signals. This so-called "virtual antenna array" technique uses bearing measurements to estimate the Direction-of-Arrival (DoA) of the targets. Unlike conventional DoA estimation methods that require large, expensive antenna arrays, the virtual antenna array is implemented with a mobile single-antenna receiver. While the receiver is moving and receiving signals simultaneously, the DoA can be estimated by capturing the phase interferometry of the intercepted signal at several locations along the receiver trajectory.

The first part of this thesis is to verify the suitability of channels in UAV-assisted communication for the application of DoA-based localization methods. We investigate channel characteristics of UAV-assisted communications by performing extensive simulations using ray-tracing simulations. The results show that the angular spread of the UAV platform is very limited, and the power-weighted average angle of all multipath is close to the actual azimuthal angle. Both features are beneficial for DoA estimation, which proves that the

application of virtual array methods on UAV platforms is very promising.

We then focused on improving the accuracy and the robustness of the proposed method. The main difficulties of the virtual array are two-fold: 1) estimate the relative positions of the receiver during its movement to reconstruct the array manifold that is necessary for array signal processing; 2) address the phase distortion caused by the Local Oscillator (LO) frequency offset between the transmitter and the receiver. The first challenge is addressed by implementing inertial navigation with inertial sensors, and the second challenge is addressed by the two frequency offset compensation methods presented in this thesis. We then perform a comprehensive nonlinear observability analysis for the system to provide guidelines for designing feasible and user-friendly receiver trajectories. The proposed system is implemented on a software-defined radio testbed and tested in an indoor environment.

Finally, the proposed virtual array system is implemented and evaluated in UAV-based communication networks. We have performed extensive simulations to investigate the DoA estimation accuracy by considering different system configurations. Parameters including the LO quality, the frequency offset compensation method, the SNR, and the UAV trajectories are evaluated. Simulation results show that the virtual array can be a promising technology for UAVs to localize ground targets.

Keywords: Direction-Finding, Inertial Navigation, Radiogoniometry, Signal-Direction-Tracking, Software Defined Radio, Synthetic Aperture Radar, UAV-assisted Communication, Virtual Antenna Array

ACKNOWLEDGEMENTS

The journey of the Ph.D experience that lead to this dissertation has been rewarding, fulfilling and challenging. Luckily, I got a lot of support and encouragement from many people around me.

I would first like to sincerely thank my Ph.D supervisor, Prof. François Quitin, whom I have had the honor to work with. His academic enthusiasm and inspiring advice have been an inspiration throughout the process. Although conducting research in a challenging field is stressful, he has never lost trust in me. Instead, he helped me to open my eyes to the value of my research and trained my ability to solve struggling problems. Another special thanks to my co-supervisor, Prof. Ke Guan. He is one of the first person that lead me to the world of academic research, when I was just a bachelor student. He also provide many guidance and assist for the whole time.

I also would like to thank the rest members of my jury committee, Prof. Philippe De Doncker, Prof. François Horlin, Prof. Danping He, and Dr. Fernando Rosas. They provided valuable feedback and guidance throughout this process. Conversations with Fernando helped me to build confidence in my early Ph.D stage and I also thank him for introducing me to researchers in similar fields.

The Department of BEAMs-EE is a comfortable and supportive place to work. I would like to express my sincere gratitude to my colleagues and friends, they are George Bousdras, who treated me like a big brother and we discussed a lot of interesting topics; Zohreh Ebadi, for her support and care; Cedric Hannotier, for his help in USRP hardware and support in daily life; Youssef Agram, I enjoy all the academic discussions with him and I also admire his passion in life; Quentin Delhaye, for his help in lab teaching and his humour. I am also especially grateful to Michel OSEE, Amelia Struyf, Axel Dero, and Anne-Cecile Muffat. I would like to thank everyone who helped me during the four years.

I have been fortunate to have many good friends when I was in Bruxelles. I thank Sami

Mezhoud, he made my time much easier when I first arrived Belgium and he also taught a lot about embedded electronics. I also thank Tianran Ding and Yijia Huang, who supported me and encouraged me during hard times. In particular, I thank Yan Liu, Baowen Zhang and Ziying Wei, for all the adventures together.

Last but not least, I am deeply thankful to my family. To Chengfa Du and Jing Yu, for giving me the strength to never give up easily. To my amazing sibling and brother-in-law, Xin Du and Bin Wu, for all the love and support. Greatest thanks go to my girlfriend, Mengkun Zhang, I am proud of her and it is wonderful to be on this life-long journey with her. Our cat, Latte, just bit me but I also love him forever.

TABLE OF CONTENTS

LIST OF TABLES

LIST OF FIGURES

CHAPTER 1
INTRODUCTION: WIRELESS COMMUNICATIONS WITH UAVS

1.1 Unmanned Aerial Vehicles

Unmanned aerial vehicles (UAVs), also known as drones, are aircraft that are piloted by remote controllers or embedded computer programs. Historically, UAVs were mainly used in military applications and aerial inspections. In recent years, there has been a surge of enthusiasm for using UAVs in civil and industrial applications due to the advancement of UAVs' manufacturing technologies and their reducing cost, making them more accessible to the public. Nowadays, UAVs have found numerous applications in many fields, including filmmaking, aerial surveillance, photography, package delivery, and telecommunications [1]. In June 2016, Pricewaterhouse Coopers (PwC) announced that the addressable market value of UAV products is over $127 billion, and the civil infrastructure is dominating with a market value of $45 billion. Besides, more than 100,000 new jobs in the unmanned aircraft industry are expected by 2025 [2]. Therefore, UAVs have become a promising technology that could create abundant business opportunities in the next decade.

UAV configurations are typically split into two categories: fixed-wing UAVs and rotary-wing UAVs, as shown in Figure 1.1. Choosing the right type of UAV is essential for efficient mission accomplishment. The fixed-wing UAVs are good candidates for long-range or long-endurance surveillance missions but inherently suffer from hovering difficulties; The rotary-wing UAVs can take off/land vertically and remain stationary at a hovering location, which has attracted a great deal of attention from the scientific and industrial community [3]. In the remainder of this thesis, we only refer to the multi-copter rotary-wing UAVs unless stated otherwise.

With unique features including excellent mobility in three-dimensional (3D) space, au-

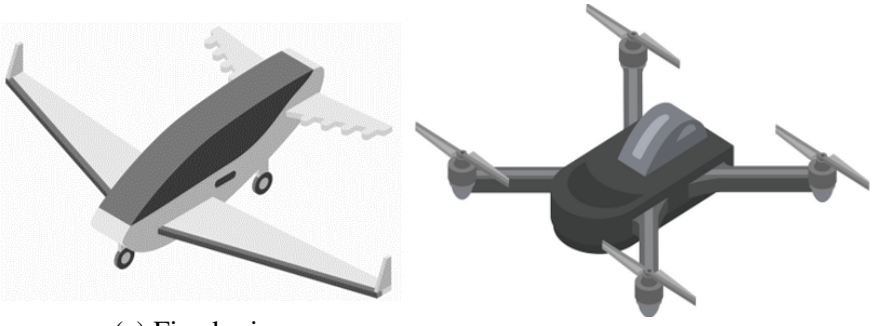

(a) Fixed-wing (b) Rotary-wing

Figure 1.1: Typical UAV categories

tonomous operation, and on-demand deployment, UAVs have the potential to provide appealing solutions for a wide range of applications, including civil, public safety, industrial Internet of Things (IIoT), and surveillance. In these applications, UAVs serve as flying platforms with adaptive altitude support and inherent mobility, and hence require a secure, reliable wireless communication infrastructure for command and control, as well as efficient information dissemination towards the ground control station [4]. Therefore, integrating a suitable wireless communication technology into UAV platforms for ubiquitous connectivity and seamless service is important. Similar technology is also promising in emergency communication, where UAVs can carry commercial base stations and assist in terrestrial wireless networks, especially when ground base stations collapse (e.g., disaster relief, military situations).

1.2 Wireless Communication with UAVs

The integration of wireless communication into UAVs brings both opportunities and challenges. There are different types of communication links in an aerial network, each with its own requirements. As a result, the network modules onboard the UAVs have to satisfy these distinctive requirements. Moreover, proper wireless technologies are also required to support the demand of these identified use cases. For example, in UAV-based surveillance, the wireless communication infrastructure must ensure safe piloting and transmission of

the real-time surveillance video. In the following, we will provide a brief overview of the communication requirements and the applicability of common wireless technologies in UAV networks. Two common paradigms for integrating UAVs into cellular networks are also presented.

1.2.1 Communication Requirements

From the communication viewpoint, the requirements of UAVs can be classified into two broad categories: one should be able to ensure a safe, reliable, and efficient flight operation, commonly known as the control and non-payload communication (CNPC) [5]; the other one refers to all information dissemination activities between the UAV and the ground station pertaining to a UAV mission, known as payload communication [4], as shown in Figure 1.2;. The latency and spectrum requirements for CNPC and payload communications are generally different.

A typical CNPC link is dedicated to maintaining and securing communications between the ground pilot station and the aircraft to ensure safe and effective UAV flight operations. This link can be either a line-of-sight (LoS) air-to-ground (ATG) link between the two platforms or a beyond-line-of-sight (BLoS) link with another entity, such as a satellite or a cellular network [6]. Data rates for such links are expected in the order of Kbps (Kilobits per second). The requirements for reliability and latency are much more stringent, e.g., less than 10^{-3} packet error rate and a latency less than 50 milliseconds (ms) [1]. Since losing the CNPC signal can be catastrophic, the CNPC links must operate over a protected spectrum, allocated by the International Telecommunications Union Radiocommunication Sector (ITU-R) [7]. Actions taken at the ITU World Radio-communication Conference (WRC) in 2012 have established sufficient spectrum resources to meet this requirement, i.e., the L-band spectrum at 960-977 MHz and a portion of C-band at 5030-5091 MHz [8].

Compared to CNPC links, the payload communication link is usually used for data applications. Therefore, it requires much higher throughput and bandwidth [9]. For instance,

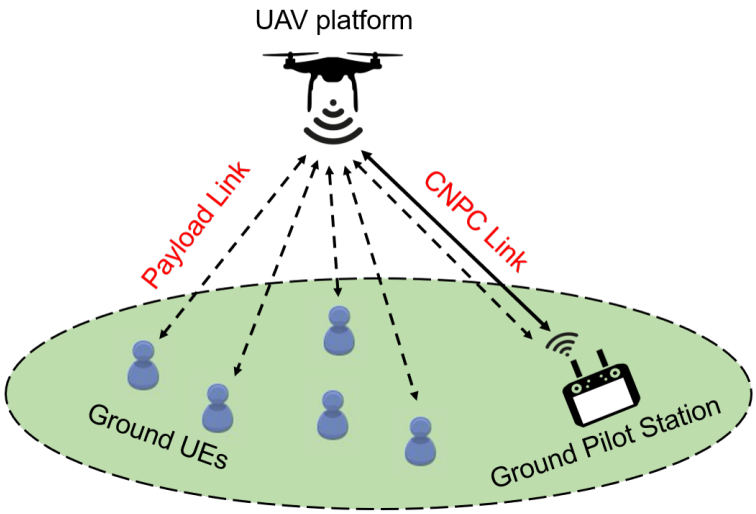

Figure 1.2: UAV Link Type

to support the transmission of real-time high-definition (HD) image/video from the UAV to the ground user, the data rate should keep in the order of Mbps (Megabits per second). The data rate requirement for UAVs serving as aerial platforms can be even higher, e.g., Gbps (Gigabits per second) for data backhauling applications. As a result, proper wireless technologies are required to meet both the CNPC link requirements and the payload link requirements in UAV communication scenarios.

1.2.2 Wireless Technologies in UAV Communication

In UAV wireless applications, four candidate communication technologies are applied to support CNPC and payload requirements:

- **Direct Link:** Traditional UAV systems mainly rely on simple direct communication links between the UAV and the ground pilot station over the unlicensed spectrum (e.g., the Industrial Scientific Medical (ISM) 2.4 GHz). The direct link is typical of low data rate, insecure, short operation range, vulnerable to interference, and relies on the LoS visibility. Due to the above limitations, the direct link cannot be a proper solution for supporting the deployment of UAVs in many wireless communication applications.

- **Satellite Link:** Enabling UAV communications by leveraging satellites is particularly useful for UAVs where the terrestrial network coverage is unavailable. In addition, satellite signals can be used to support CNPC links and payload communications under BLoS conditions, providing maximum coverage. Despite all these advantages, this technology suffers from propagation losses and delays due to the long distances that data packets have to travel [9]. The high operational cost of satellite communications also hinders its widespread deployment in consumer-grade applications.

- **Flying Ad-Hoc Network (FANET):** FANETs can be used to offer easily deployable and self-configured peer-to-peer communications among UAVs. With the help of a multi-hop ad-hoc network schema, FANETs architecture allows all the UAVs to communicate with each other and other base stations simultaneously without having any pre-defined fixed infrastructure [10]. While FANETs are robust and flexible architecture that allow UAV communications to be deployed as a relatively small network, their topology changes rapidly and can cause many routing problems. Moreover, it is generally unable to provide a scalable solution for serving massive UAVs deployed in a wide area.

- **Cellular Network:** While the technologies mentioned earlier have failed to satisfy the critical criterion for UAV communication and networking in a cost-effective manner, integrating UAVs into cellular networks (e.g., 4G networks) has attracted significant interest. Due to the almost ubiquitous coverage of cellular networks, as well as their high throughput and advanced communication technologies, both the CNPC and payload communication requirements of UAVs can be potentially met [1]. For instance, challenges like link reliability can be overcome by exploiting the possible link redundancy in cellular technology, meaning that if one link fails or operates poorly, the system can switch to a better link [6]. This opportunity provides the UAV

network with resilient and seamless connectivity, which is desirable for several applications [11]. Even though cellular technologies for UAV communication sounds promising, it still comes with several disadvantages. First, a single cellular signal tower has a limited service range and needs several handovers during UAV missions. Then, due to the high altitude of UAVs, the UAV causes and suffers more severe inter-cell interference (ICI) from a much larger number of non-associated co-channel base stations in the neighboring area as compared to the terrestrial user equipment, which can result in very poor performance [12]. Besides, there are still scenarios where cellular services are not available, such as in remote areas like the sea, desert [5]. A detailed discussion of the opportunities and challenges has been provided in [13, 14].

In summary, four wireless technologies can be applied to support UAV platforms in emergency communications, and cellular networks have some distinct advantages over the other technologies. Current 4G networks can accommodate most UAV applications. Although there are a number of mission-critical applications that still require higher throughput and stringent latency, these features are expected to be enabled by next-generation mobile technology. In addition, cellular communications are only suitable for UAV platforms flying below 125 meters above the ground due to increased path loss and reduced signal to interference and noise ratio (SINR) [9]. At higher altitudes, satellite data links are more commonly used. In the next section, we will discuss the commonly known paradigms of integrating UAVs into the cellular network.

1.2.3 Integration UAVs with Cellular Network

The integration of UAVs in cellular networks falls under two main categories: UAVs can be employed as aerial communication platforms in which each UAV serves as a flying base station or a mobile relay node by mounting communication transceivers to provide and enhance communication services to ground user equipment (UEs). UAVs can also serve as new UEs in the existing cellular network, supported by the ground cellular base stations, to

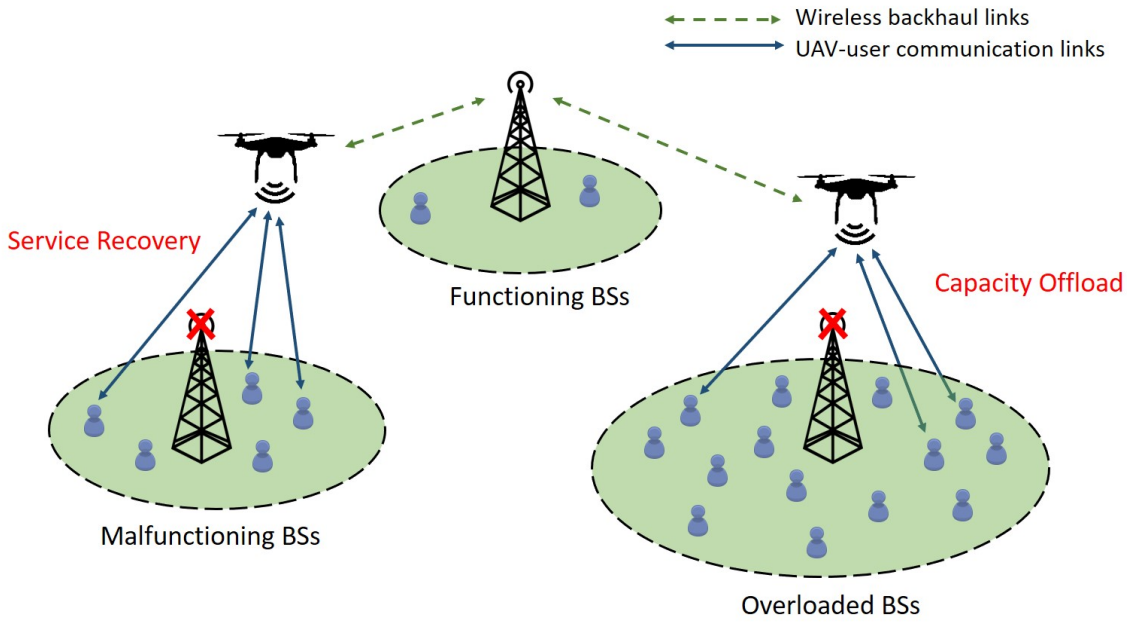

(a) The UAVs operate as base stations for rapid service recovery after disaster situations.

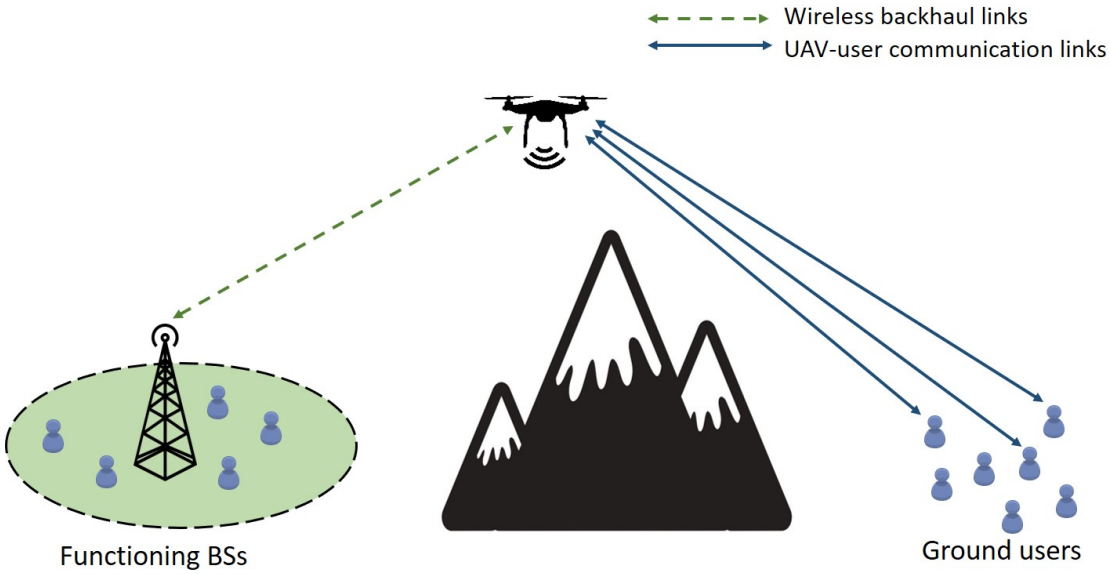

(b) The UAVs function as relay nodes to provide wireless connectivity without direct links.

Figure 1.3: The schematic diagram for UAV-assisted cellular communication networks to provide ubiquitous coverage in the serving area

achieve significant performance improvement and enable many applications ranging from surveillance to navigation. These two paradigm are commonly referred to *UAV-assisted wireless communications* and *Cellular-Connected UAVs*. Most of the existing research is restricted to these two paradigms [1, 3, 4, 11].

- **UAV-assisted wireless communications**

  UAV-assisted wireless communication is achieved by mounting light commercial base stations on UAVs, serving as aerial base stations or aerial relay nodes. The architecture of this application is shown in Figure 1.3. Aerial base stations are typically deployed for emergency communications and require seamless integration with existing cellular networks and ground communication infrastructures; The aerial relay node serves as a bridge between end-users without cellular coverage and the nearest available cell towers [15]. Overall, UAVs are used to assist existing terrestrial wireless communication systems to improve the Quality of Service (QoS) of users, spectral efficiency, and coverage gains. Base stations mounted on UAVs can be deployed on-demand, bringing great opportunities for disaster management, rescue, and emergency response [16]. These advantages will meet the diverse, dynamic, and growing data requirements in 5G cellular systems.

- **Cellular-Connected UAVs**

  In this paradigm, UAVs serve as new UEs that are coworking with terrestrial UEs that access the cellular network infrastructure from the sky, that provide the following opportunities, with the architecture shown in Figure 1.4. First, unlike typical wireless UAV connectivity that relies on short-range communication technologies (e.g., WiFi, radio fingerprints), cellular-connected UAVs allow ground pilots to control UAVs remotely with an unlimited operation range [4]. Thus, they provide an effective solution to maintain wireless connectivity between UAVs and other end-users, regardless of their locations. Secondly, Cellular-Connected UAVs can achieve significant performance gains in terms of reliability, security, and communication

throughput compared to simple direct ground-to-ground UAV communication [5]. In addition, Cellular-Connected UAVs are also cost-effective solutions since they reuse advanced cellular technologies and millions of existing cellular infrastructures deployed worldwide.

The above applications make integrating UAVs into the cellular network a promising new technology to support the data traffic requirements of the current cellular systems. Moreover, the new released 3GPP document has published the enhanced requirements for UAV communications, including new Key Performance Indicators (KPIs) and hobbyist applications relevant to UAVs [17]. The 3GPP also proposed a Non-terrestrial networks in [18], including an airborne or space-borne vehicle to embark a transmission/reception equipment node, for extending service to places without terrestrial coverage. In the following section, we highlight the primary opportunities, design challenges, and perspectives to be considered for UAV-based cellular networks, including solutions that are already available.

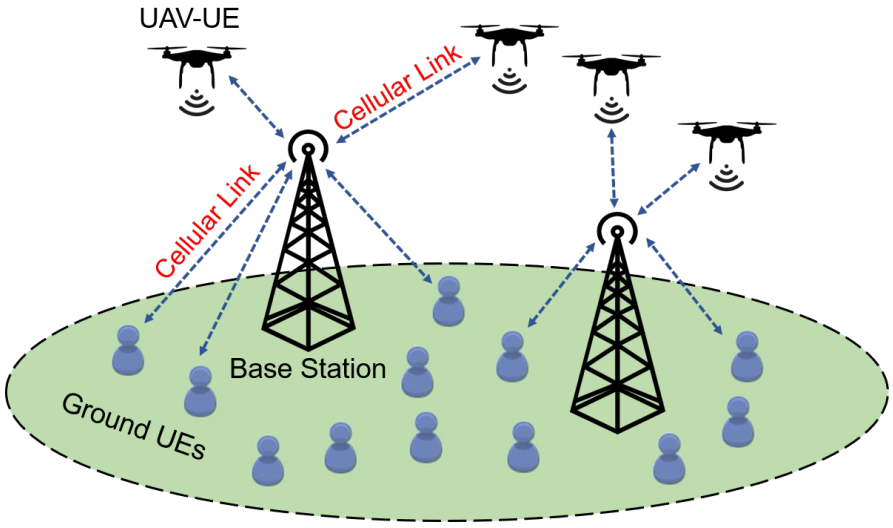

Figure 1.4: The schematic diagram for Cellular Connected UAVs

1.2.4 Opportunities and Challenges

Opportunities

The integration of UAVs into cellular networks is a fundamental shift from terrestrial to airborne networks. It also comes with great opportunities for applications across diverse areas. The characteristics of aerial networks bring the following main advantages [1, 19, 16]:

- **Fast and on-demand deployment:** Conventional ground cellular infrastructures are generally built and distributed based on the user density and geographic conditions [20]. However, the locations and altitudes of the UAV platforms can be dynamically adjusted according to the real-time demand (e.g., user distribution, data traffic, channel condition) [21]. Therefore, UAVs' fast and on-demand deployment makes them an attractive method to provide reliable cellular coverage in time-varying scenarios, without the cost of extra infrastructure.

- **Excellent mobility and flexibility:** Because of the excellent mobility and flexibility of UAV platforms, they can serve as both quasi-stationary aerial base stations/relays and mobile base stations/relays, depending on the mission [22]. At the same time, the ability of the UAV to move in three dimensions removes the need for the network to be affected by wireless channel uncertainty (e.g., a target being blocked by an obstacle). Instead, the network can reduce channel uncertainty to a required low value by reacting to the current channel conditions.

- **LoS-dominant channel:** UAV platforms typically operate at high altitudes, which has several benefits, including a higher possibility to have clear LoS visibility with ground infrastructures. While the terrestrial channels usually suffer from severe attenuation, shadowing, and fading due to multipath scattering, the links in LoS channels are typically more stable and reliable due to the absence of obstacles [23].

Challenges

Despite the numerous advantages of the UAV-integrated cellular network, several key challenges and considerations also arise and need to be considered.

- **Unique Channel Characteristics:** Unlike traditional terrestrial networks, the UAV platforms serve at high altitudes and lead to unique ATG channels. Given the unique propagation nature for UAV communications, the ATG channels are highly dependent on the altitude, the elevation angle, and propagation environment (e.g., urban, suburban, rural) [24]. Accurate ATG channel modeling is of vital importance to enhance the network-related quality-of-service (QoS). However, finding a generic channel model for ATG communications requires comprehensive simulations and measurements in various environments. A detailed state-of-the-art for ATG channel modeling is presented in Chapter 2.

- **Optimal Deployment:** The number of UAV platforms and their respective geographical locations significantly impact various factors such as latency, data rate, and energy consumption. Hence, the optimal placement of UAVs for coverage and capacity maximization is a challenging task as many parameters must be taken into account, including altitude, deployment environment (e.g., geographical area), locations of ground users, channel conditions, etc. In addition, locations of nearby cellular infrastructures also need to be considered to avoid frequent handover and co-channel interference. Among current literature, there are different solutions to solve the optimization problem. Some researchers consider the altitude of the UAV as a variable in their optimization formulation, then treat it as a 3D placement problem, while others work on a 2D placement problem with a constant height. A brief survey about these solutions is presented in [25].

- **Path Planning:** In a UAV-based communication network, optimal path planning for the UAV to travel to its final operating location is another major challenge. It requires

considering many practical constraints, including ground users' demands, flight time, energy consumption, and collision avoidance. A proper dynamic trajectory could increase the probability of link connections while maintaining sufficient coverage of the entire target area. Some work in [26] provides a new paradigm to consider both the communication throughput and the UAV's energy consumption to perform trajectory optimization.

- **Localization of Ground Users:** In traditional cellular networks, base stations are deployed on selected, fixed locations without time or power constraints. The signal coverage range and cell size are also dictated by design. On the contrary, the service coverage of an aerial base station is determined by the geographical location of the UAV itself. As a result, the UAV-enabled communications are much more location-aware than terrestrial networks, i.e., UAVs should actively locate ground users and then fly nearby, thus providing maximum capacity to the target area and being more energy-efficient. This challenge is of critical demand, especially in emergencies where the disaster has damaged other ground facilities used for localization, and we have to locate users quickly and provide rescue services efficiently.

In the literature, practical algorithms and schemes have been proposed for addressing challenges related to ATG channel modeling, UAV deployment, path planning, etc. However, the localization of ground users with UAVs has not received sufficient research focus yet. Most ground user localization methods currently use time-based measurements or received signal strength (RSS) measurements [21, 27], which requires sophisticated time synchronization steps or only provides rough distance estimates. The following section will briefly describe the state-of-the-art of current ground user positioning methods and propose a new paradigm, i.e., UAVs equipped with radio platforms for localizing and serving ground users.

1.3 New Paradigm: UAV-assisted Ground User Localization

1.3.1 Localization Approaches in Cellular Networks

Localization is acknowledged as a fundamental functionality in modern communication systems. The highly accurate location information can be used to provide location-aware services, such as navigation, mapping, social networking, and intelligent transportation systems. In UAV-based aerial networks, the knowledge of the ground user's location is even more important since most UAV applications are location-aware. Moreover, ground user localization is also a key consideration in designing the optimal deployment and flight path of the UAV. In principle, the Global Positioning System (GPS) can be applied in many outdoor scenarios to support ground users in calculating their location. However, users need to actively broadcast their location to inform the UAV base station, which may not always be feasible in practical situations. GPS is also known for its high cost and vulnerability to jamming. Therefore, alternative localization techniques in UAV-based communication networks are essential.

As UAVs are integrated into cellular networks in UAV-assisted communications and cellular-connected UAVs applications, localization methods in conventional cellular networks are also promising in aerial networks. Various localization approaches have been devised for each generation of cellular technology, from the first generation (1G) to the fifth generation (5G), and they utilize cellular infrastructures based on uplink and downlink communications. More specifically, localizing a target with these approaches in cellular networks is a two-step process. First, a set of signals are exchanged between the target and a sufficient number of base stations. Then, approaches with different metrics, including the RSS, the time of arrival (ToA), the time difference of arrival (TDoA), and the direction of arrival (DoA), are used to compute the location of the target [28]. More specifically, ToA, TDoA, and RSS provide the distance information between the target and receivers, while DOAs estimate the source bearings relative to the receivers.

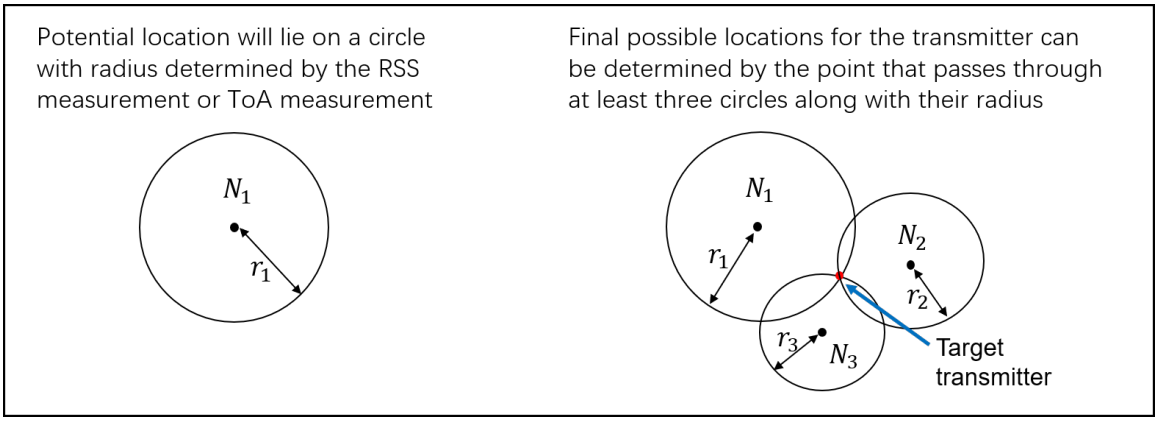

(a) RSS and ToA Principle

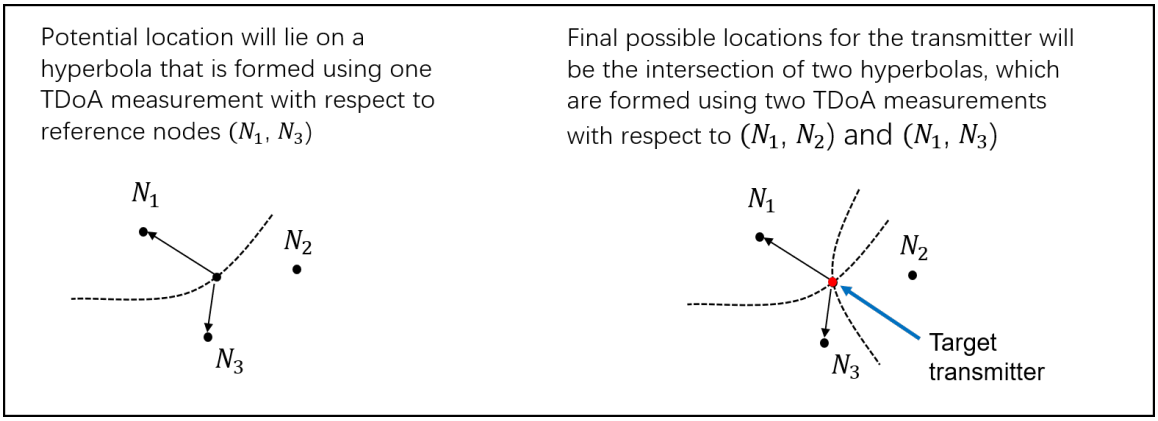

(b) TDoA Principle

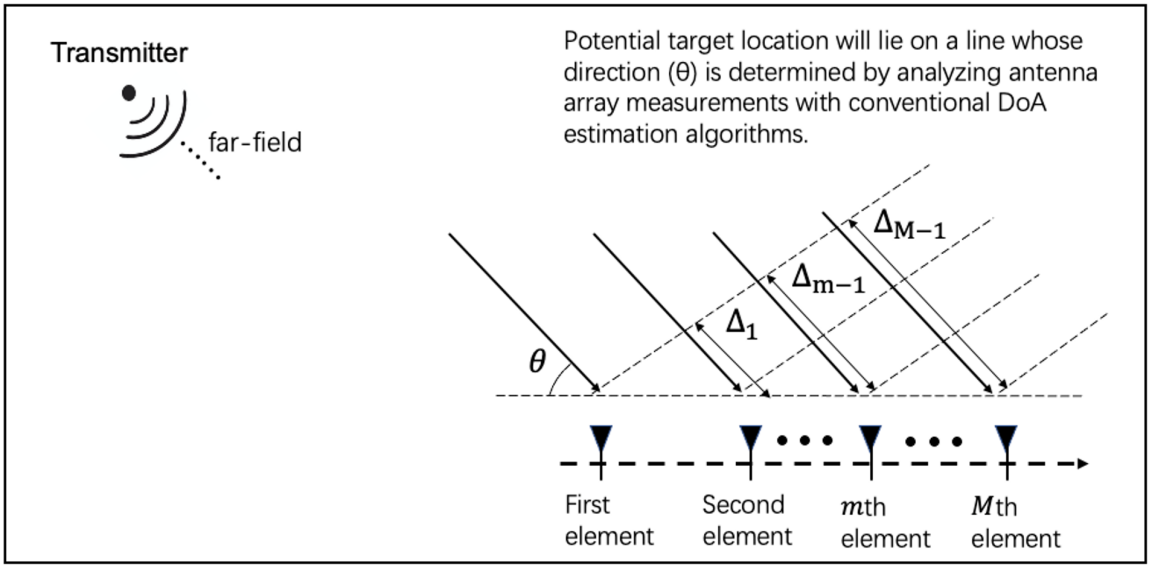

(c) DoA Principle

Figure 1.5: Passive Localization Concept [28]; (a) Trilateration for RSS and ToA technique; (b) TDoA localization; (c) DoA Estimation with Antenna Array;

- **RSS technique:** this method relies on the physical principle that the received strength of a radio signal is inversely proportional to the increase in propagation distance. The RSS is the actual signal power strength received at the receiver, usually measured in decibel milliwatts (dBm) or milliWatts (mW). The absolute distance between the target transmitter and a receiver can be estimated via several different signal propagation models, given that the transmission power or the power at a reference point is known [29]. Then, basic trilateration algorithms are applied for the target transmitter to obtain its location relative to the multiple reference points, as shown in Figure 1.5a. Additionally, the RSS technique works under non-line-of-sight (NLoS) conditions when a specific propagation model is used.

- **ToA technique:** also known as Time of Flight (ToF), which exploits the signal propagation time to calculate the distance between the target transmitter and the receiver. The distance is provided by the ToA value multiplied by the speed of electromagnetic waves (approximately 3×10^8 m/s). Similar to the RSS, each ToA corresponds to a circle centered at a reference node, and the ToA from at least three different reference nodes is required to calculate the unique location of the target device with respect to these reference nodes. In general, ToA technology requires high precision time synchronization between the transmitter and receiver, as a synchronization deviation of a few nanoseconds can lead to positioning errors of several meters [30]. Moreover, the accuracy of ToA relies on the LoS visibility since the multipath caused by obstacles will travel through a longer path, causing an increased propagation time.

- **TDoA technique:** TDoA is the difference in signal propagation time from the target transmitter to two reference nodes. A single TDoA measurement can be used to determine the position of the target on a hyperbola, with foci on these two reference nodes. Then, at least two TDoA measurements from three reference nodes (with known positions) are required to calculate the exact location of the target transmitter

as the intersection of the two (or more) hyperbolas, as shown in Figure 1.5b. In TDoA-based localization, clock synchronization is only required across all reference nodes, which gives more flexibility than ToA, where all transmitters and nodes need to be synchronized [31]. The TDoA estimation accuracy depends on the reliability of TDoA measurements and the existence of the LoS path.

- **DoA technique:** DoA-based approaches use antenna arrays to estimate the angle at which the transmitted signal impinges on the receiver, as depicted in Figure 1.5c. The received signals are delayed versions of the transmitted signal where the delays are functions of the emitter direction θ and the array geometry. As a result, the received signal phase is the sum of the geometry/direction-related phase and a random phase component common to all antennas. Several direction-finding algorithms are proposed to estimate the θ by analyzing the received phase at the array elements [32]. The accuracy of DoA estimation depends on the physical size of the antenna array, array element imperfections (mutual coupling, manufacturing inaccuracies), multipath effect, interference, and signal-to-noise ratio. In other words, to realize a satisfying localization, the DoA estimation generally requires a clear LoS visibility and an antenna array with reasonable physical size. Moreover, the DoA estimation does not need synchronization among nodes, and the system complexity is simple, which is extremely valuable in many industries (e.g., cellular networks, radar, industrial IoT).

The above localization metrics differ in terms of positioning accuracy, system complexity, and requirements for collaborating users. The trade-off between each technique's positioning accuracy and implementation complexity is a significant factor when deciding which method to use. For example, localization based on the RSS measurement requires no specialized hardware or signal processing, which is one of the simplest and widely used approaches for indoor localization [33]. Methods based on ToA or TDoA generally provide high accuracy, but they require precise time-synchronization between sensors, which often complicates the system design [28]. The DoA method determines the angle of the arriving

signal, and it has great potentials for feasibility without synchronization requirements or prior knowledge from the environment. However, to allow base stations to estimate the DoA, they should be equipped with multi-antenna arrays, which incurs high price, significant form factors, and power consumption [34].

In real-world scenarios, the performance of different localization methods is also sensitive to the LoS visibility, i.e., the estimation accuracy can be significantly biased due to multipath and shadowing. While LoS connections are easy to establish with UAV platforms, it is still challenging to implement conventional cellular localization approaches into aerial networks directly due to the distinctive characteristics of UAVs and ATG channels. In the following, a state-of-the-art for UAV-assisted passive localization is presented.

1.3.2 State of the Art

There are a wide variety of technical challenges that must be addressed in UAVs for localization. The first difficulty is the uncertainty and characteristics of the ATG channel, which may plague the metrics designed for terrestrial positioning. Secondly, the localization-relevant module should not add too much weight and physical size for the aerial platform due to UAVs' payload and battery constraints. Besides, the mobility and 3D operation range make UAVs extremely difficult to be clock synchronized. Last but not least, the number of UAV platforms required for ground user localization should be minimal to maintain the system's cost and efficiency.

Attempts to use UAVs to assist localization have been documented since the early 21st century. In [35], a control architecture that allows multiple UAVs to detect mobile radio frequency (RF) emitting ground targets is presented. The UAVs are equipped with low-precision RF detecting sensors, and the targets are emitting specific signals randomly with variable time duration. In [36], researchers provide a prototype for UAVs to localize a stationary radio source with ranging measurements and bearing measurements. The flight test in this research provides good accuracy in a small search area (9m$\times$9m); however,

it only works for a specially designed signal beacon. The UAV platforms used in these experiments are also customized quadrotor helicopters, thus significantly increasing the cost of the system. After that, most relevant literature focuses on using existing cellular network infrastructure and algorithms.

After 2008, considerable research focus appeared on the fields of ground source localization with RSS measurement. In [37], authors provide a new method to exploit the RSS measurements. The UAV rotates once to make a bearing estimate, then flies to the direction with the strongest transmit power and rotates again for a new bearing estimate. Instead of using the maximum RSS over a single rotation, authors in [38] perform a correlation over the RSS measured over a single rotation and the radiation pattern measured in an anechoic chamber, thereby requiring shorter times to reach the transmitter. However, these control strategies are challenging to design in practice, and they require the UAV to make some specific trajectories or maneuvers, which puts an additional latency on mission time or flight time. In [39, 40], authors propose a method of tracking wild animals by attaching signal beacons to them, then measuring RSS by implementing directional antennas to fixed-wing UAVs to enable localization.

In [41], authors present a localization method based on RSS from terrestrial nodes when UAVs serve as base stations; a specific path loss model is also proposed for range estimation by considering height-dependent exponent and shadowing effect. Localization error versus UAV altitudes, number of UAVs, and UAVs' inter-distance are also studied with simulations. In [42], an RSS-based UAV localization model has been proposed to jointly exploits the UAV trajectory information and RSS measurements from multiple base stations. Similar research can be found in [43], where a localization scheme was developed for multiple RF source positioning by using two UAVs equipped with multiple RSS sensors. The RSS measurement subjected to each source was applied as an input for the developed Kalman Filter. However, this model-based research only provides a theoretical basis without experimental verification. Overall, as RSS measurements usually significantly degrade with

distance due to the increasing shadowing effect, the accuracy of RSS-based localization methods is not guaranteed.

Time-based localization methods (e.g., ToA and TDoA) usually require a complex time synchronization process. More specifically, TDoA measurements require synchronization between base stations (i.e., UAVs), while ToA measurements require synchronization between base stations and targets [28]. Those requirements are challenging to achieve and maintain in UAV networks. Researchers in [30] proposed a time synchronization-free ToA method to locate the source position, and the synchronization error is compensated by employing a multivariate linear model. However, such a method requires at least four UAV platforms and transceivers with excellent clock stability; otherwise, the localization error will be unacceptable. In [44], the localization of a stationary emitter by two UAVs measuring the ToA of the radio signal has been investigated; a trajectory control algorithm is also provided to minimize the ToA estimation uncertainty. In [45], a scheme for ToA localization using pseudo-range measurements from satellites with a single UAV is proposed. However, its accuracy is unsatisfying. Besides, the possibility of indoor ToA localization by using UAVs is studied in [46]. The results proved that the localization accuracy could be improved with an increasing number of anchor nodes and optimal UAV locations. Overall, ToA technology usually requires multiple UAV platforms and is more suitable in cooperative scenarios, which may not be available in emergency scenarios.

TDoA localization utilizes the time delay between the emitter signals received at multiple UAVs. As a result, at least three UAV-mounted sensors are necessary to perform the required hyperbola positioning. A detailed literature review could be found in [21, 47]. In [48], an approach for UAV indoor navigation using a TDOA-based ultra-wideband (UWB) indoor localization system is presented, a complex wireless clock synchronization method is also provided to overcome the time offset between multi UAV limitations. The TDOA localization of a stationary emitter by a swarm of UAVs is provided in [49], where a UAV trajectory optimization method is applied. Besides, researchers in [50] performed target

localization with a combination of TDoA measurements and RSS measurements, where TDOA measurements are obtained from multiple moving sensors over time intervals along a UAV flight path. A simple Least-Squares solution to determine target localization is derived based on the TDOA measurements combined with known sensor locations. However, the synchronization challenge is not considered. Therefore, the accuracy of time synchronization in UAV platforms is still the bottleneck of ToA/TDoA localization techniques.

Localizing a target via DoA measurements is widely used previously in ground mobile sensor networks and cellular networks. The ground targets' position can be determined by utilizing its one-dimensional DoA measurements (only the azimuth angle) measured at a multi-antenna array with prior known locations. In UAV-based scenarios, the localization of ground emitters can be obtained by analyzing the paired two-dimensional DoA measurements (i.e., azimuth and elevation angles), measured by antenna arrays from the sky. For example, a localization scheme is proposed in [51] by mounting multiple sensors on a UAV swarm. In [52], a method for locating GPS jamming transmitters is proposed by jointly using DoA and TDoA measurements collected by smart antennas mounted on multiple UAVs. Since the cost of multiple UAVs is prohibitive, performing localization with a single UAV is more convenient and cost-effective. Some researchers choose to mount or hang multi-antenna arrays on the bottom of the UAV; however, they suffer from the significant payload and form factor constraints. In [53], a circular microphone array is hung from the UAV with nylon cords of 1 m length. However, this method is only possible for acoustic source localization. In [54], a linear array of 2 m length is mounted on a UAV, and the localization is performed outdoors. Although the accuracy seems good, such architecture design is hard to implement in practice. Other researchers focus on using the nested array in UAV-based localization [55, 56], while the sensitivity and spatial resolution is not satisfying due to limited array size.

In summary, DoA-based localization keeps a good balance between the accuracy and the system complexity among all the localization metrics, without requirements for syn-

chronization. These features lead to significant potential in UAV-based communication networks to provide a solution for the power and payload constraints. In this thesis, we are trying to improve the DoA estimation accuracy in ground users localization by exploiting the benefits and mobility of the UAV networks. Instead of using a multi-antenna array, which caused high power consumption and significant form factors, we provide a DoA estimation method using a single-antenna device called the "virtual multi-antenna array". While the device is moving and continuously receiving signals, the DoA can be estimated by analyzing the intercepted signals at several positions along the receiver's trajectory.

In addition, the term "localization" in target scenarios with DoA measurements refers to two different applications of source localization. The first application is to find the location of a source from a sensor array's point of view, where only the direction towards the source can be estimated. This is equivalent to estimating the parameter θ from the far-field sensor array model in chapter 3. The second application is to find the spatial location of a source in a physical environment. The mapping from the spatial source location to the corresponding DoA vector is unique, and the reverse is not true. This means that multiple DoA estimation have to be taken to disambiguate the location of the source. In the rest of this thesis, the term "localization" refers the first application only, i.e., only the direction of the source is estimated.

1.4 Contributions and Outline of the Thesis

This thesis proceeds in Chapter 2 with a detailed channel characteristics analysis of the ATG channel using ray-tracing simulations to determine whether the DoA-based metrics are suitable for performing the DoA localization in UAV-based networks. Important factors corresponding to the DoA estimation accuracy, including the angular spread (AS) and power-weighted mean DoA, are investigated to describe the channel's spatial properties. Our major contributions in this chapter are:

- In UAV-based communications, the angular spread at the UAV platform is very lim-

ited; the weighted mean AOA and EOA are also close to the actual bearing angles with respect to ground targets. Such channel characteristics are beneficial for applying DoA-based localization methods on UAV platforms.

- Contrary to conventional ground cellular channels, the angular spreads, and delay spread at the MT are larger in LoS than NLoS situations, which could be explained by the particular geometry of the ATG channels.

- The delay spread in LoS scenarios and NLoS scenarios vary substantially with increasing UAV altitudes. In LoS scenarios, the delay spread shows a decreasing trend with increasing UAV altitudes. On the contrary, in NLoS scenarios, the delay spread tends to increase monotonically with the UAV.

Chapter 3 proceeds with the design and system model of the Virtual Multi-antenna Array. Two algorithms are provided to eliminate the bias introduced by imperfect hardware. A detailed observability analysis is also provided for improving its robustness by providing solutions when the receiver positions are unknown. The whole system is proved to be feasible in UAV communications, consumer electronics, industrial IoTs, and other applications with form factor constraints. Our major contributions in this chapter are:

- The concept for DoA estimation with the conventional array processing method and the proposed virtual array method is explained in detail. The Main difficulties with virtual array systems are discussed: 1) the relative position of the receiver needs to be estimated with high accuracy; 2) phase distortions caused by the LO frequency offset need to be addressed.

- Two methods are provided to compensate for the phase distortions due to the LO frequency offset: the SAS method and the joint estimation method. Their advantages and disadvantages are both presented.

- Receiver trajectory reconstruction with inertial sensors is realized by implementing

a nonlinear Kalman filter. Constraints regarding the receiver movement (maximum velocity, maximum trajectory size, etc.) are also discussed.

In Chapter 4, the proposed virtual array system is implemented on a software-defined radio testbed to verify its feasibility in real-world scenarios. The proof of concept is designed with common commercial electronics that contain significant hardware bias. In addition, we use the nonlinear observability analysis method to design user-friendly trajectories that are feasible for DoA estimation. In this chapter:

- A comprehensive nonlinear observability analysis is performed for the virtual array system. Results show that the azimuth angle of arrival and the LO frequency offset can be estimated with linear trajectories if the movement contains accelerations. Also, the azimuth angle can be estimated by measuring the accelerations.

- Extensive simulations are performed to confirm the theoretical observations provided by the observability analysis.

- The proposed system is implemented on a software-defined radio that integrates off-the-shelf components. Experiments are performed in an indoor multipath environment with designed trajectories. DoA estimations are realized by tracking the positions and accelerations of the receiver, which proves the feasibility of the virtual array system.

In Chapter 5, we aim to implement the virtual array system in UAV-based communication networks. The original system (estimate azimuth angle only) expands to a high dimension (estimate both azimuth angle and elevation angle); thus, we make necessary adaptations for the corresponding signal model and the LO frequency offset compensation methods. Extensive simulations are then performed to investigate the effects of UAV channels and UAV movements. The results show that the accuracy of DoA estimation in UAV-based communications can be improved by using better LO quality configurations

and shorter UAV flight times. In addition, high SNR and large UAV trajectory sizes also help in providing better DoA estimation results.

Finally, the thesis is concluded with Chapter 6, where the major results of the previous chapters are reminded. Some future work directions are also presented.

CHAPTER 2
AIR-TO-GROUND CHANNEL CHARACTERISTICS

2.1 Motivation

In conventional localization methods, the DoA is usually estimated based on antenna measurements with array processing algorithms (e.g., MUSIC, Beamforming). Nearly all of these algorithms assume that the source signal arrives at UAV with a discrete, distinct angle. Such assumption leads to a signal subspace of low rank, and the low-rank property is exploited to find the impinging direction [34]. A more detailed discussion is given in Chapter 3.

However, multipath propagation is common in real-world cellular networks, i.e., several signal replicas will generally be incident on the receiver array. If the LoS connection exists between the transmitter and receiver, most of the incident energy will likely concentrate in a single plane wave (usually indicating the target DoA). When there is no LoS visibility or weak LoS visibility, the received signals are mostly multipath components with different reception angles and propagation delays. If the angle dispersion (i.e., the angular spread) and delay dispersion (i.e., the delay spread) is severe, the channel will directly degrade the antenna array correlation and cause large DoA estimation errors, as signals incident on the receiving array can be seen as distributed sources emitting at different times [57]. In addition, a large angular spread means that the multipath DoAs deviate significantly from the power-weighted mean DoA; a small angular spread indicates that the multipath DoA is concentrated around the power-weighted mean DoA. If the power-weighted mean DoA is close to the actual bearing DoA, the channel can be considered suitable for DoA-based localization [58].

Therefore, it is important to properly understand the propagation characteristics (es-

pecially the spatial and temporal information) of the multipath components (MPCs). The spread of MPCs in time and angular domains serves as an indicator for the effectiveness of DoA-based localization methods. For this reason, geometry-based stochastic channel models have been extensively investigated in the literature for conventional cellular networks in which a fixed base station (BS) communicates with a mobile terminal (MT). Since geometric channel models inherently establish probabilistic relations between spatial locations of the transmit (Tx), receive (Rx), and scatterers to model wireless propagation, it is vital to investigate the distributions of the angular spread and delay spread to gain insights into the nature of the target channel model [59].

In conventional cellular infrastructures, the BS antennas are usually mounted above signal towers or rooftops, thereby reducing the near-field scattering. This propagation environment leads to many investigations into 3D channel characterization and modeling. For example, azimuth angles at MTs in urban city scenarios are modeled as lognormal distribution; elevation angles are modeled as laplacian distribution in [60]. Subsequent investigations have derived the connection between link performance and angular/delay spreads in different frequencies and environments, e.g., COST2100 [61], WINNER II [62] and 3GPP [63]. In addition, spatial parameters in 3D models are defined, including the root-mean-square (RMS) delay spread, the RMS azimuth spread of arrival/departure (ASA/ASD), and the RMS elevation spread of arrival/departure (ESA/ESD). They are applied to describe the power dispersion in the azimuth domain of arrival/departure (AOA/AOD) and power dispersion in the elevation domain of the arrival/departure (EOA/EOD) domain, respectively.

However, only limited research has thoroughly investigated the spatial and temporal properties in UAV channels, especially from a localization perspective. The dynamic of the angular spread for a UAV platform and the effect of the surrounding environments also require more in-depth investigation to ensure the effectiveness of DoA-based approaches in localization and communication. The delay spread should also be considered, as large delay spreads usually imply complex multipath environments that make the localization

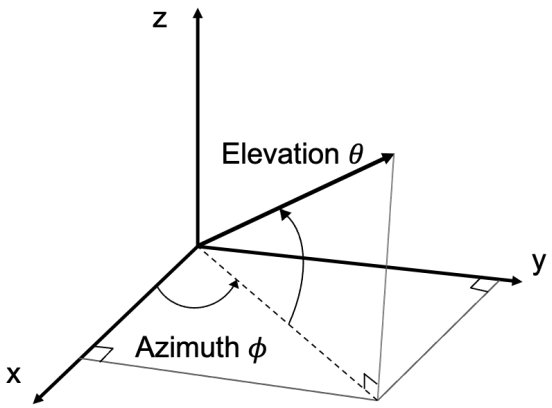

Figure 2.1: Defination of azimuth and elevation

more challenging. Since installing channel sounders on UAVs is very difficult due to on-board space constraints and payload limitations, we conducted extensive ray tracing (RT) simulations to study the ATG channel characteristics of an urban city environment. The ground users serve as mobile terminals (MTs) in our simulation configurations, and the UAV serves as an aerial receiver. The UAV aims to localize MTs based on their emitted signal. When the carrier frequency does not change (which is our case), the angular spreads in the uplink and downlink are equivalent due to the channel reciprocity [64]. Therefore, although the signal travels from MT to UAV, the channel can still be referred to as the ATG channel.

Conventions: In this section, azimuth is defined as the angle of the projection of the vector in the xy-plane w.r.t. the x-axis, and elevation is the angle between the vector and the xy-plane [60], as shown in Figure 2.1.

2.2 Simulation Setup

The RT is a powerful map-based approach to predict the channel characteristics for a given environment model and deployment configuration, which has been applied for field prediction in indoor and urban environments since the early 1990s [65]. The RT simulator applied in this thesis is CloudRT, a 3D ray-tracing software developed by Beijing Jiaotong

University, which can simulate propagation rays from any arbitrary and reasonable transmitter and receiver positions [66]. Different rays that correspond to different MPCs are traced from the transmitter to the receiver. Each MPC is characterized by several parameters: time of arrival; real part of the field intensity; imaginary part of the field intensity; angular of arrival; angular of departure; and type of the MPC (including the LoS rays, first and second-order reflections, diffracted rays along building edges, and diffuse scatterings from rough surfaces). The validation and calibration of the CloudRT simulator has been provided in [67, 68, 69], where the parameters of the simulated MPCs are compared with those of the corresponding MPCs in the channel measurements.

The UAV-communication environment considered in this chapter is a typical 3D urban city, with 137 buildings under different heights going from 5 m to 70 m, as shown in Figure 2.2a. Its specifications meets the statistical standards of typical urban city model proposed by the ITU, including the built-up land area ratio, the number of buildings per unit area, and the buildings heights distribution [70]. The total dimensions of the 3D environment model are 650 m by 500, with 250 ground mobile terminals (MT) distributed uniformly over the whole map, and the MT height is set to 2 m above ground. The UAV is equipped with a downwards-facing patch antenna, and MTs are equipped with vertically-oriented dipole antennas. It is worth mentioning that the tilts of MTs antenna are randomly distributed but deviate no more than $\pm$ 45 $^{\circ}$ from the vertical direction. The UAV and MT antenna are vertically polarized with 0 dBi gain, and the transmission power is set to 0 dBm. The simulation is conducted by fixing the MT while changing the position of the UAV along four linear trajectories. Each trajectory has a length of 450 m and contains 50 UAV positions, with a resolution of 9 m. Figure 2.2b demonstrates the traced rays of a snapshot between a single MT position and a single UAV position.

Considering that Long-Term Evolution (LTE) is a reliable technology to support the required link performance of UAV networks [5], we set the carrier frequency at 2.6 GHz, corresponding to the LTE carrier frequencies. As the ATG channel characteristics are re-

lated to the altitude of the UAV, simulations are conducted at 60 m, 80m, 100 m, 120 m, and 140m, respectively. For each snapshot, rays are collected until up to 250 dB loss, and then a channel impulse response (CIR) is calculated by the software, including received power strength, phase, propagation time, angle of arrival, and angle of departure (for both azimuth and elevation). Also, the direct path between the UAV and MTs can be obstructed by obstacles; thus, we have a collection of the LoS and the NLoS cases. For example, when the UAV altitude in the simulation is set to 100 m, we collected $250 \times 50 \times 4$ channels in total, containing 28626 LoS cases and 21374 NLoS cases.

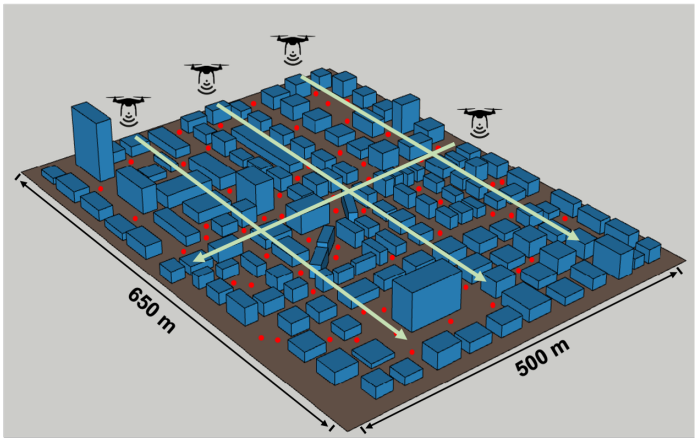

(a) Ray-tracing simulation scenarios

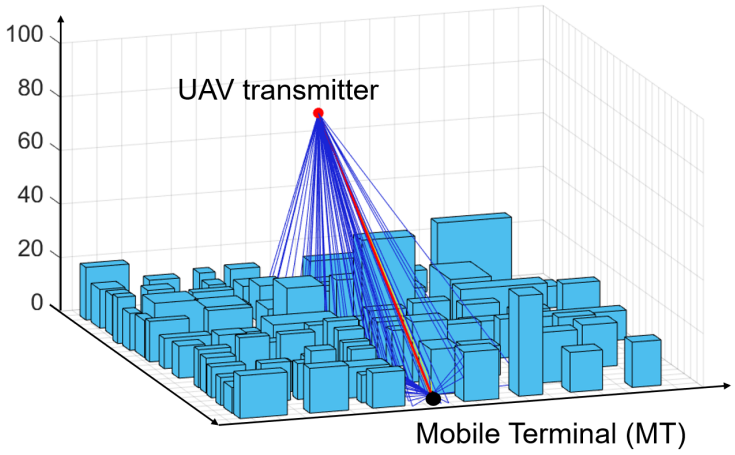

(b) One example snapshot from ray-tracing simulations

Figure 2.2: The Ray-tracing simulations. (a) The scenario contains 4 linear UAV trajectories, and 250 MTs randomly distributed on the ground. (b) Traced rays of a snapshot in UAV-based communication. The solid red line represents the line-of-sight path, the blue lines represent all the multipath components.

2.3 Derivation of Angular/Delay spread

In this simulation, the ray-tracing results provide detailed information of multipath components between the UAV and the MT. The CIR calculated by the software is expressed as:

$$h(\tau,\varphi,\theta)=\sum_{k=1}^{N_{mpc}}\alpha_k e^{j\varphi_k}\cdot\delta(\tau-\tau_k)\,\delta(\phi_{AoD}-\phi_{AoD,k})\,\delta(\theta_{EoD}-\theta_{EoD,k})\cdot\delta(\phi_{AoA}-\phi_{AoA,k})\,\delta(\theta_{EoA}-\theta_{EoA,k}) \tag{2.1}$$

where N_{mpc} is the number of generated paths, $\alpha_k e^{j\varphi_k}$ is the complex gain of ray k while φ_k denotes for the phase; τ is the excess delay; $\phi_{AoA,AoD}$ and $\theta_{EoA,EoD}$ are the azimuth and elevation angle of azimuth/departure. Spatial parameters including ASD, ESD, ASA, and ESA can be extracted from the simulated multipath information. As angular spreads are significant indicators related to the DoA estimation accuracy, they are calculated following the definition in [63]. For example, the RMS azimuth spread at arrival, ASA, quantifies angular dispersion in the omnidirectional azimuth plane, computed as:

$$\sigma_{ASA}=\sqrt{\frac{\sum_{k=1}^{N}\left[mod\left((\theta_{AoA,k}-\mu_m,2\pi)\right)\right]^2\cdot\alpha_k^2}{\sum_{l=1}^{N}\alpha_k^2}} \tag{2.2}$$

where μ_m is the power-weighted mean AOA and calculated by:

$$\mu_m=\sqrt{\frac{\sum_{k=1}^{N}\theta_{AoA,k}\cdot\alpha_k^2}{\sum_{l=1}^{N}\alpha_k^2}} \tag{2.3}$$

and ESA is defined similarly by replacing the azimuth angle θ_{AoA} with the elevation angle θ_{EoA}.

The RMS delay spread is frequently used to characterize the time dispersion of the channel. It is a vital parameter for the design of wireless transceivers and localization applications, including to select transmission bandwidth, digital modulation, equalization

methods, and ToA estimation [28]. Generally speaking, the Power Delay Profile (PDP) gives the distribution of signal power received over a multipath channel as a function of propagation delays. The derivation of RMS delay spread is defined as the square root of the second central moment of the PDP:

$$\tau_{RMS} = \sqrt{\frac{\sum_{k=1}^{N} \left(\tau_k - \tau_m\right)^2 \cdot \alpha_k^2}{\sum_{l=1}^{N} \alpha_k^2}} \tag{2.4}$$

where the mean excess delay τ_m is defined as the first moment of the PDP:

$$\tau_m = \sqrt{\frac{\sum_{k=1}^{N} \tau_k \cdot \alpha_k^2}{\sum_{l=1}^{N} \alpha_k^2}} \tag{2.5}$$

In summary, angular spread and delay spread are measures of the multipath richness of a communications channel, and they denote the spatial/temporal dispersion of propagated signals [71]. Based on the definition in equation (2.2) and (2.4), their value depends on the ratio between the power of the strongest MPC (e.g., the LoS path) and the power of other MPCs. In principle, when the strongest path is dominant among the received power, the angular/delay spread will be small; when other scattered MPCs make a considerable contribution to the total received power, and their angles differ from the LoS path, the angular spread will be significant.

2.4 Results and Discussions

In this section, we calculate the angular spread, the mean angle, the delay spread and the mean excess delay from the simulated data. Their variation with the LoS visibility, the UAV altitude, and the UAV-MT distance is also analyzed with respect to the unique propagation environment of the ATG channel. By using statistical modeling methods, the analysis and results for angular and delay spread are presented below.

2.4.1 Distribution of ASA/ESA

As presented in Section 2.2, we collected 50000 snapshots for ASA and ESA at a given UAV altitude. Here we take trajectories at 100 m as an illustrative example. The probability density function (PDF) of the angular spreads in the LoS scenario and the NLoS scenario are plotted in Figure 2.3. The PDF function is used to specify the probability of an angular spread falling within a particular range of values.

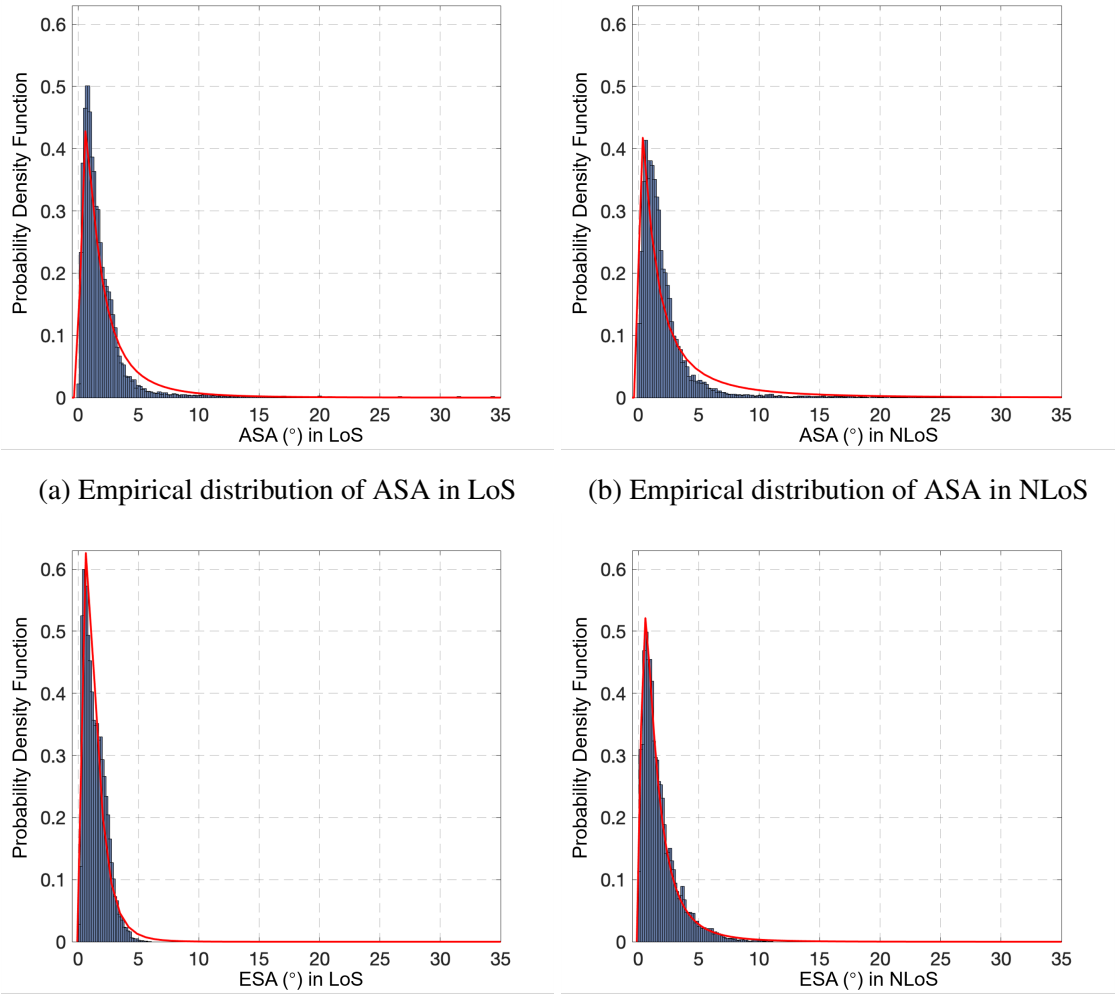

(a) Empirical distribution of ASA in LoS

(b) Empirical distribution of ASA in NLoS

(c) Empirical distribution of ESA in LoS

(d) Empirical distribution of ESA in NLoS

Figure 2.3: Distributions of ASA/ESA in LoS scenarios and NLoS scenarios. The superimposed red curves are lognormal distributions used to model the PDF.

To better characterize the distribution of angular spreads at the UAV, we have used the Akaike information criterion (AIC) method in [64] to evaluate the candidate distribution functions in fitting the probability histograms, including Normal, Lognormal, Rician, and weibull, etc. The AIC results have shown that the Lognormal distribution is the most appropriate distribution to describe the PDF of ASA and ESA, where the same observations are provided in [64]. For example, in LoS scenarios, the PDF of the ASA can be mathematically expressed by:

$$f_{ASA}(x) = \frac{1}{\sqrt{2\pi}x\sigma_{ASA}} exp\left[\frac{-(\ln x - \mu_{ASA})^2}{2\sigma_{ASA}^2}\right] \tag{2.6}$$

where μ_{ASA} and σ_{ASA} are the mean and standard deviation (STD) of the fitting PDF, respectively. The fitting of ESA is similar by replacing parameters μ_{ASA}, σ_{ASA} with μ_{ESA}, σ_{ESA}. The value of μ and σ for ASA/ESA spreads in both LoS and NLoS scenarios are provided in Table 2.1.

Parameters	ASA		ESA	
	LoS	NLoS	LoS	NLoS
μ	0.42	0.52	0.15	0.24
σ	1.01	1.29	0.68	0.91

Table 2.1: Lognormal Distribution Modeling Parameters

By comparing the PDF distribution and the established statistical model, the spatial multipath propagation characteristics can be observed as follows.

- The first observation from Figure 2.3 is that the ESA and ASA are distributed over a narrow range of less than 10° (with an average angular spread around 2.5°), for both LoS and NLoS scenarios. These magnitudes are much smaller than the ESA and ASA in conventional 3D cellular channels, e.g., average ASA around 9° and average ESA around 15° in [64]. Such observations indicate that the spatial dispersion of received power at the UAV side is very limited, and all the multipath components arrived at the UAV with similar incident angles. Therefore, the power-weight mean

AoA/EoA is a good representation of the real bearing to the ground MT.

- In Figure 2.3, the histograms for both ASA and ESA are steeper in the LoS scenarios than the NLoS scenarios. The μ and σ in LoS are also smaller than NLoS. Therefore, the angular spread in NLoS scenarios tends to be slightly larger than in the LoS scenarios. This phenomenon is expected and can be explained by the fundamentals of angular spread: When scattered MPCs contribute considerably to the total received power, the angular spread will be large; When the LoS path is dominant among the received power, the angular spread will be small. In NLoS scenarios where obstacles have blocked the LoS path, the direct signal will be attenuated; Thus, MPCs will make more significant contributions in the total received power, caused a bigger angular spread in both azimuth and elevation domain.

- For both the LoS scenarios and the NLoS scenarios, the histograms of ESA are steeper than the ASA. The μ and σ of ESA is also smaller than the ASA, under the same LoS visibility. In other words, the dispersion of ASA is more severe than ESA. This is because of the lack of scatterers in the air and the MPCs all reach the UAV from the ground, as shown in Figure 2.2b, which limited the elevation angle at the UAV to $(0^\circ, 180^\circ)$. On the other hand, the azimuth angle of MPCs at the UAV may come from any direction among $(0^\circ, 360^\circ)$, depending on the distribution of ground scatterers. As a result, the power can spread in a broader range in the azimuth domain than the elevation, causing a bigger angular spread for ASA.

The analysis above demonstrates that the angular spread at the UAV is minimal, which means most of the received power at the UAV comes from approximately the same direction. Such a direction is usually approximated by the power-weighted average angle of arrival (AOA and EOA) in Eq. (2.3). If these approximate directions are close to the true bearing directions, the DoA-based estimation usually provides accurate localization results [58]. Therefore, the cumulative distribution functions (CDFs) of variations between the

mean angle and the true angle are provided in Figure 2.4. It can be seen from the figure that the mean AOA and EOA are a good representation of the real bearing to the ground user.

As a result, the DoA-based estimation has a great potential in UAV-based cellular networks to localize ground targets since the estimated DoA should be close to the true DoA. Also, beamforming (or highly directional antennas) can be a simple strategy to achieve appropriate link performance between the UAV and MTs, focusing power towards the target terminal.

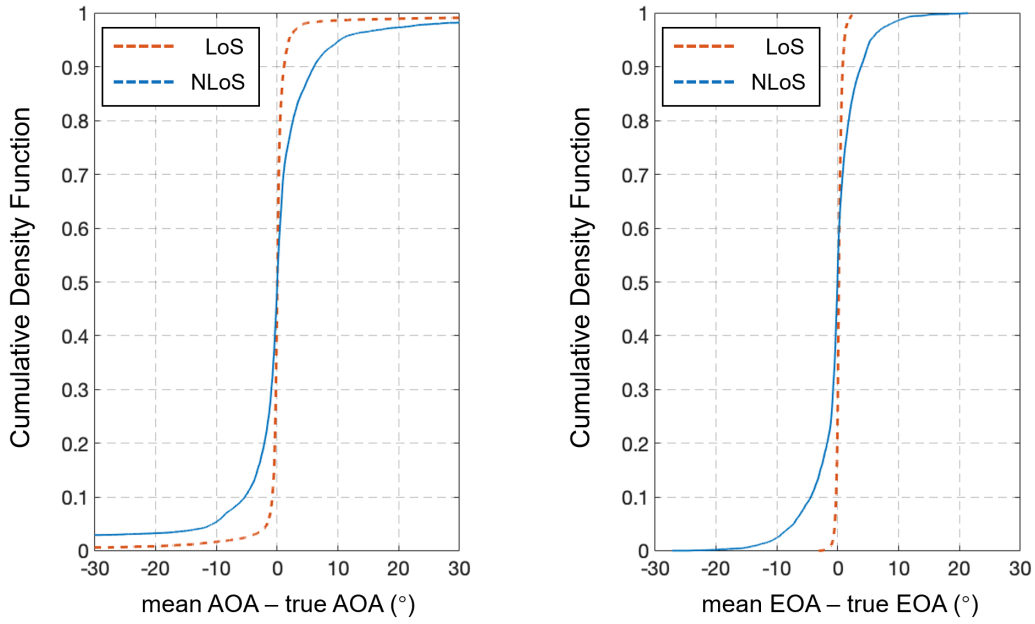

(a) (b)

Figure 2.4: Mean AOA and EOA relative to the true bearing angle

2.4.2 ASA/ESA Variation with UAV Altitude

As introduced earlier, the spatial characteristic of the ATG channel is a function of UAV altitudes [1]. To investigate the correlation between the ASA/ESA and the UAV altitudes, we first calculate the median value of the collected ASA/ESA, under different UAV altitudes and LoS visibility. To highlight their variations with altitudes, we use relative median values rather than absolute values, which is done by considering the median value of

ASA/ESA at 60 m as a reference and calculating median values relative to it. The angular spread at 60 m is thus assumed to be zero. Figure 2.5 shows the relative variation of these median angular spreads at UAV altitudes from 60 m to 140 m.

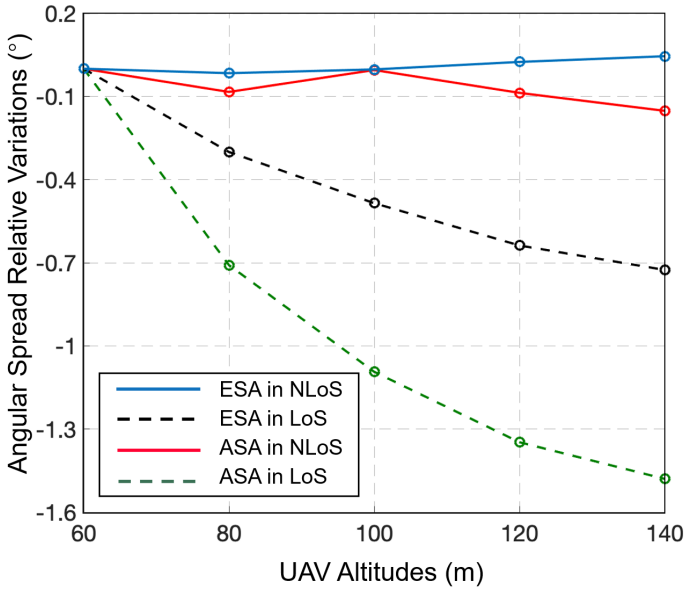

Figure 2.5: ASA/ESA Variation with UAV Altitude

It can be seen from the figure that the ASA and ESA in LoS scenarios show a decreasing trend with an increasing UAV height, and this trend is not observable in NLoS scenarios. The fluctuation of angular spreads in the LoS scenario can be explained as follows: When the UAV serves at low altitudes, The LoS path is dominant and the MPCs reflected or scattered from surrounding scatterers also contribute considerable power to the total received signal. When the UAV flies higher above the ground, both the received power through the LoS path and MPC paths decrease due to a larger path loss [64]. However, the power of the MPC may decay more quickly and significantly than the LoS path. Therefore, as the altitude of the UAV increases, the portion of the LoS power among total received power at the UAV increases monotonically, caused the angular spreads to drop. In the case of NLoS scenarios, the strongest MPC has a higher impact on the angular spread due to the missing dominating LOS, and the incident power of MPCs also decreased in higher UAV altitudes.

However, more scatterers are also observed for the UAV base station, and they provide rich multipath. As a result, the portion of the strongest MPC power in the total received power may remain roughly the same; thus, the angular spread variation is not apparent.

2.4.3 Distribution of ASD/ESD

Unlike UAV base stations that serve in altitudes up to hundreds of meters, the antenna height of ground MTs is expected to be much lower than the surrounding scatterers, e.g., buildings, walls, and trees, especially in an urban city scenario. Therefore, the distribution features for both ASD and ESD may be unique. The PDF of azimuth and elevation spread with and without LoS connection is calculated and shown in Figure 2.6.

It can be clearly observed from the figure that the PDF of ASD and ESD has different features compared with ASA and ESA. The difference between the LoS scenarios and the NLoS scenarios is also apparent. Similar to subsection 2.4.1, we have used the AIC method to find the most appropriate distribution in fitting the histograms of ASD and ESD. The results have shown that the Normal distribution is suitable to model the PDF of ASD and ESD in LoS scenarios. Since all spread values in our simulations are positive, we use the truncated normal distribution in [72] to model the distribution of ASD and ESD in LoS scenarios of the urban city channel:

$$f_{ASD_{LoS}}(x) = \frac{1}{\sigma}\frac{\phi(\frac{x-\mu}{\sigma})}{1-\Phi(\frac{-\mu}{\sigma})} \quad \text{for } x > 0 \tag{2.7}$$

where $\phi(\xi)$ is the probability density function of the standard normal distribution, defined as:

$$\phi(\xi) = \frac{1}{\sqrt{2\pi}} exp(-\frac{1}{2}\xi^2) \tag{2.8}$$

and $\Phi(\cdot)$ is its cumulative distribution function, defined as:

$$\Phi(\chi) = \frac{1}{2}(1 + erf(\frac{\chi}{\sqrt{2}})) \tag{2.9}$$

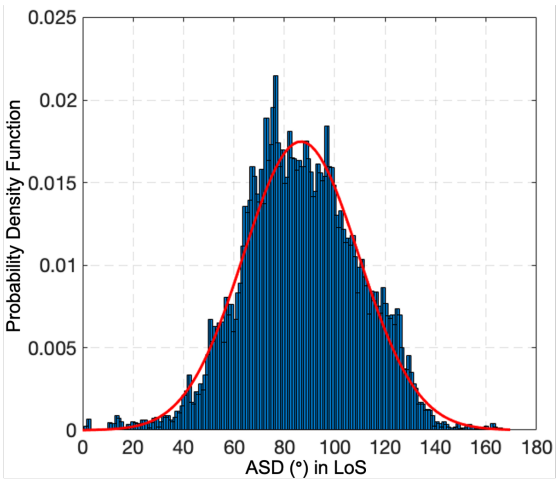

(a) Empirical distribution of ASD in LoS

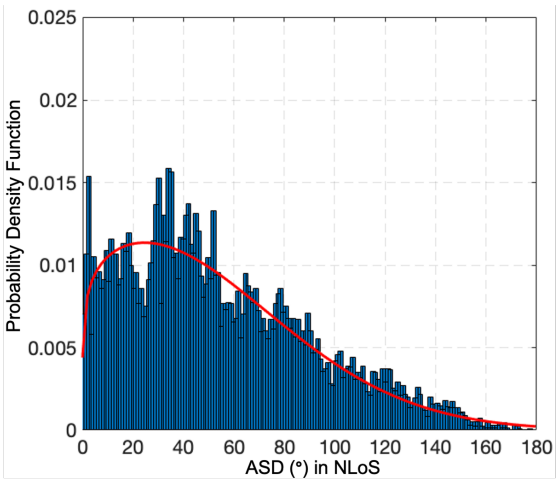

(b) Empirical distribution of ASD in NLoS

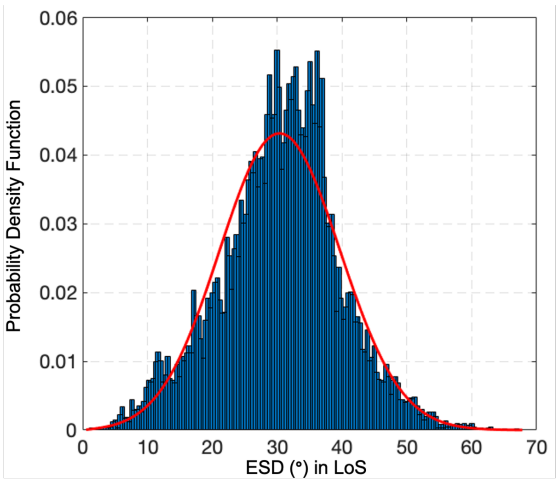

(c) Empirical distribution of ESD in LoS

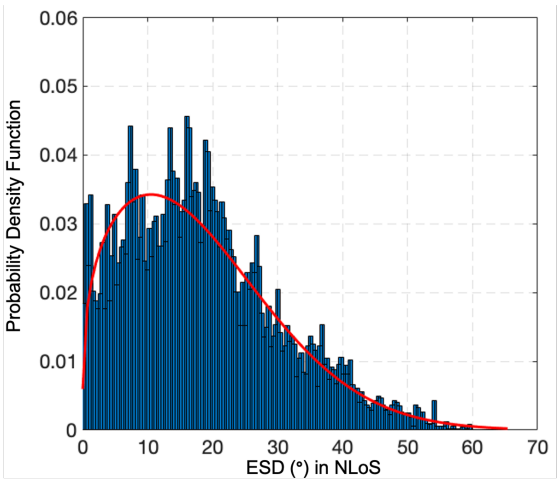

(d) Empirical distribution of ESD in NLoS

Figure 2.6: Distributions of ASD/ESD in LoS scenarios and NLoS scenarios

where the value of these parameters are provided in Table 2.2.

	ASD in LoS (°)	ESD in LoS (°)
μ	86.87	30.56
σ	22.76	9.18

Table 2.2: Truncated normal distribution in LoS scenarios

With similar methods, the Nakagami model is found suitable to model the PDF of ASD and ESD in NLoS scenarios. The general form of the PDF expressed as:

$$f_{ASD_{NLoS}}(x) = \frac{2m^m}{\Gamma(m)\,\Omega^m} x^{2m-1} exp\left(-\frac{m}{\Omega}x^2\right) \tag{2.10}$$

where m is a shape parameter, $\Gamma(m)$ is the Gamma function and Ω controls the spread of the distribution. These two parameters are calculated as:

$$m = \frac{\left(E\left[X^2\right]\right)^2}{Var\left[X^2\right]}$$
$$\Omega = E\left[X^2\right] \tag{2.11}$$

where E denotes the expectation and Var denotes the variance. Values of m and Ω for the PDF of ASD and ESD in NLoS scenarios are provided in Table 2.3.

	ASD in NLoS (°)	ESD in NLoS (°)
m	0.58	0.65
Ω	4332.69	483.76

Table 2.3: Distribution parameters for ASD and ESD

By comparing the PDF distribution and the established statistical model, the following observations can be made:

- For both LoS and NLoS scenarios, the average value of the ASD is obviously larger than the ESD. Therefore, the power dispersion in the azimuth domain is more severe than the elevation domain, where similar results are also observed for ASA and ESA. The reason behind this observation is straightforward: in the ATG channel, the elevation angle for UAV and MT mostly depends on the UAV altitudes. Instead, the azimuth angle depends on the distribution of local scatterers, which potentially allows MPCs to arrive at any azimuth angle. Therefore, the received power is possible to spread over a larger range in the azimuth domain.

- The difference between the angular spread in LoS scenarios and NLoS scenarios is clear: most angular spread in the LoS scenarios is larger than the NLoS scenarios for ASD and ESD. The CDF of angular spreads is provided in Figure 2.9. It can be seen that the median value of ESD is around 32° in LoS scenarios and only 18° in NLoS scenarios. Also, the median value of ASD is around 85° in LoS scenarios

and only 46° in NLoS scenarios. Such a phenomenon is quite interesting since, in typical ground channels, the angular spreads in NLOS are usually larger than in LOS [60]. The physical explanation for this counter-intuitive result is explained in the following.

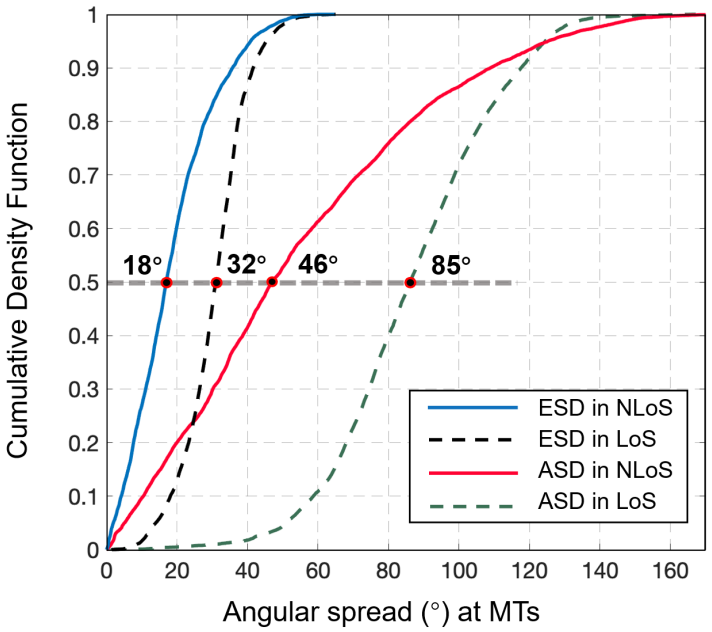

Figure 2.7: CDF of ASD and ESD

The angular spread is the metric to characterize the energy spread of the incoming signal in the spatial domain around its mean direction; it is not concerned with the absolute amount of incident power, but the angular distribution [64]. In traditional ground communications, the LoS path contains the largest power when compared with other scattered paths. Therefore, the mean AoD is approximately equal to the angle of the LoS path, thus caused low angular spreads. However, this is not the case for ATG channels. We isolated a representative example from our simulation database, then plot local scatterers and multipath rays. Figure 2.8a and Figure 2.8b shows the multipath components (MPCs) of two snapshots for two successive UAV locations, one NLoS and one LoS. The LoS path in both figures is shown in red, while the green lines indicate other MPCs. Figure 2.8c and

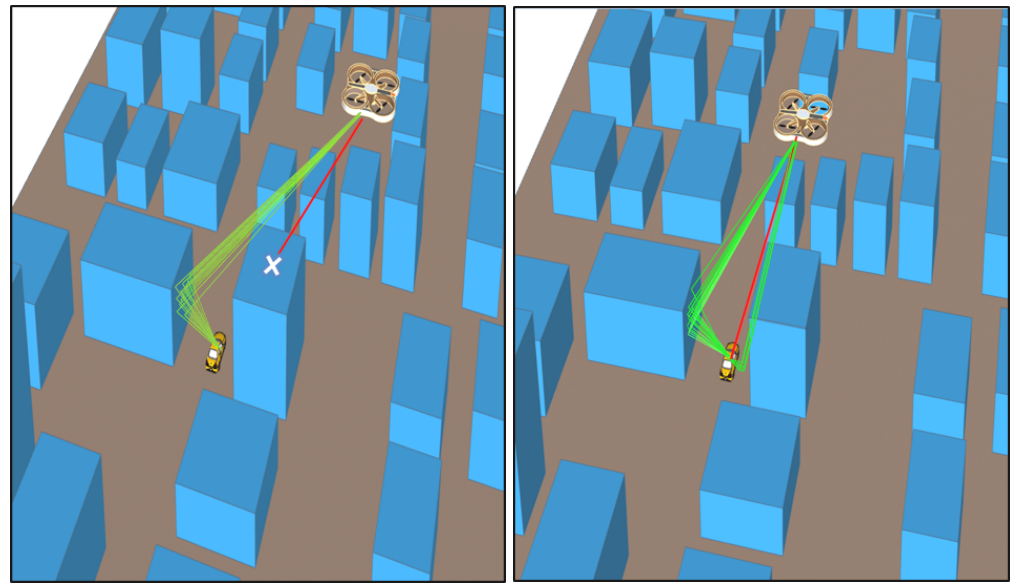

(a) Traced Rays in NLOS

(b) Traced Rays in LOS

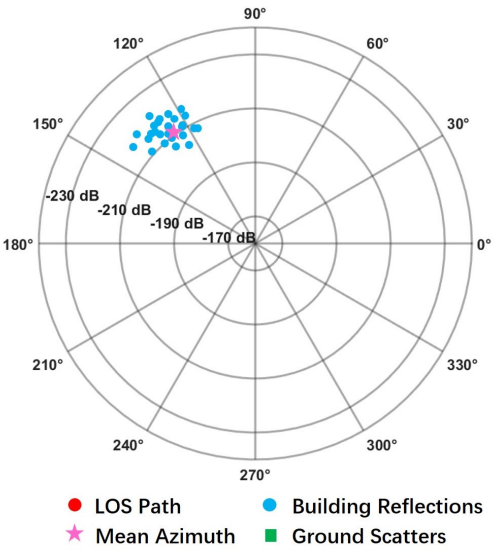

(c) AoD Distribution in NLOS

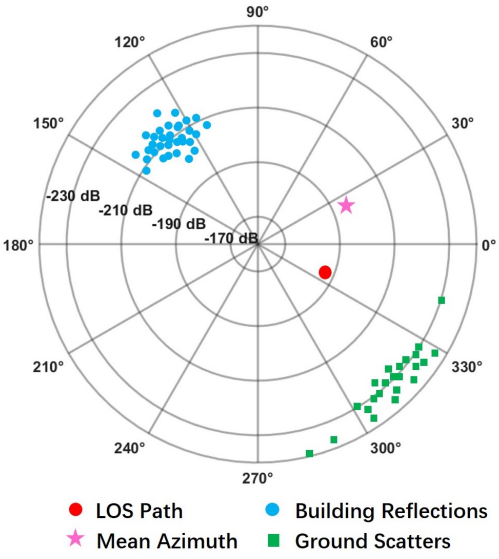

(d) AoD Distribution in LOS

Figure 2.8: Traced Rays and AoD Distribution. In NLOS, the multipath concentrate in a close range, caused a small azimuth spread. In LOS, the multipath and LOS path arrived with different azimuth angle, caused a larger azimuth spread [73].

Figure 2.8d plots the azimuth angle and received power of MPC paths in an 2D polar grid (angle/power), for these two UAV positions.

Our explanation below focuses on the reason that caused the azimuth angular spreads at the MT higher in LoS condition than NLoS, and a similar argument can be made for elevation spreads. In the NLoS snapshot, it can be seen that most of the strong multipath are reflected from the buildings located at the west side of the MT, while there is no LoS path between the UAV and the MT. Therefore, the mean AOA angle is roughly the direction of the building (west). The azimuth spreads will be relatively small since all strong paths come from roughly the same azimuth angle. In the LoS snapshot, there are two major contributions in the AOA domain: 1) the LoS path, with an AOA angle at around 330°, directly from the UAV to the MT, and 2) the multipath components, with a mean AOA angle at around 120°. The new mean AOA angle will be somewhere between these two major contributions, near 30° (the power of ground scattering paths is relatively small in this case). The azimuth spreads will then be higher since the power in the AOA domain is spread due to those two components.

2.4.4 ASD/ESD Variation with UAV Altitude

The distribution of spatial angular spreads at the MT is also affected by the UAV altitude. Therefore, we calculate the median value of the collected ASD/ESD under different UAV altitudes. Figure 2.9 shows the relative variation of these median angular spreads with respect to the value at 60 m, similar to the subsection 2.4.2. The median ASD increased up to 8° between altitudes in the LOS scenarios, while the ESD increased to 4°. In the NLoS scenarios, it can be seen that the difference in median ASD spread is up to 14°, while ESD values also increase by 4°. In summary, the value of ASD and ESD increases monotonically with the UAV altitudes for both LOS and NLOS scenarios. Also, the increase in ASD is more significant than ESD.

This behavior can be explained as follows. The existing literature has clearly shown

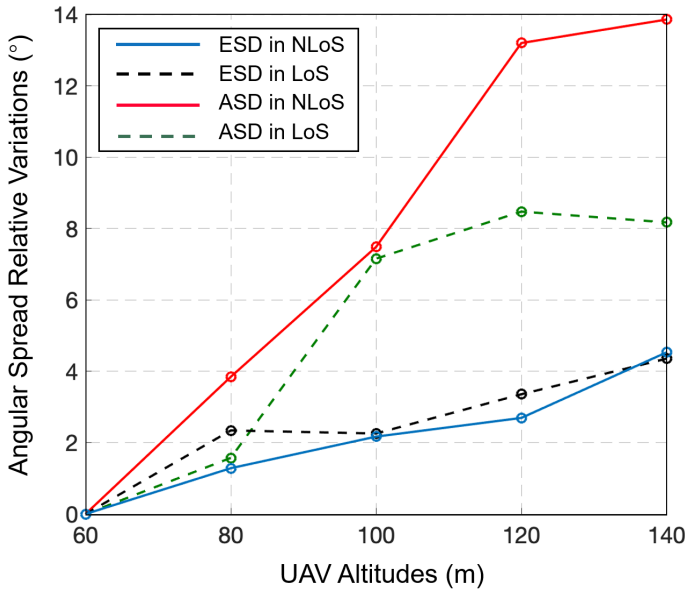

Figure 2.9: ASD/ESD Variation with UAV Altitude

that the link between ground MTs and UAVs has a higher probability of LoS visibility [19], due to fewer obstacles at higher altitudes. Additionally, when the UAV is at higher altitudes, more scatterers between the MT and the UAV are visible. Therefore, when the altitudes of UAV increases in a reasonable range, two things may happen: 1) the snapshot changes from NLOS to LOS; 2) the snapshot holds their original LOS visibility, with mew MPCs appear between the MT and the UAV.

In the first case, similar to subsection 2.4.3, most of the MPCs are came from roughly the same direction, opposite the UAV, causing a small AOA spread. When the LOS path appears at a higher UAV altitude, the received power is contributed by two major clusters, the power of the LOS path and the power of scattering paths. Therefore, the AOA spread at the MT gets higher since the power spreads in the angular domain. In the second case, the visibility of the LOS path does not change, and some MPCs may vanish due to path loss. However, there will be new MPCs emerging between the UAV and MT. Those multipath usually come from border directions due to new scatterers (which is different from ASA/ESA that MPCs arriving at similar angles), resulting in increased AOA spreads.

Therefore, the value of ASD/ESD increases monotonically with the UAV altitudes for both LOS and NLOS scenarios. Again, due to limited scatterers in the air, the power dispersion in the azimuth domain is also more significant.

2.4.5 Delay spread in ATG channel

To investigate temporal features that characterize the time dispersive nature of the ATG channel, the RMS delay spread of the urban city model under different UAV altitudes is calculated from the simulation results. Figure 2.10 shows the CDF distribution of the delay spread for both LoS and NLoS cases. The subfigure at the bottom right shows the median value of delay spread as a function of UAV altitudes. As can be seen, there is a difference between the distributions of the delay spreads in LoS and NLoS scenarios. Up to 90% of the cases, the delay spreads are less than 21.5 ns for NLoS and 25 ns for LOS scenarios, respectively. Therefore, the delay spread in LOS scenarios is slightly higher than in NLOS scenarios compared to conventional ground channels. The second observation is, in LoS and NLoS scenarios, the delay spread vary substantially with increasing UAV altitudes. In LoS scenarios, the delay spread shows a decreasing trend with increasing UAV altitudes, from 17 ns at 60 m to 15.7 ns at 140 m. On the contrary, in the NLoS environment, the delay spread tends to increase monotonically with increasing UAV altitudes, from 12.6 ns at 60 m to 14.7 ns at 140 m.

The first observation can be explained by the same phenomenon as explained in subsection 2.4.3. In the LoS environment, the delay spread is pretty high since the received power has two main contributions: the LoS path and the MPCs. The MPCs arrive at the receiver with a longer propagation time, so the total received power dispersed in the time domain, resulting in a high delay spread. In the NLoS environment, most strong MPCs come from close clusters, causing a decreasing delay spread due to limited power dispersion. As a result, at a reasonable UAV altitude, the delay spread of the ATG channel in LoS scenarios is larger than the delay spread in NLoS scenarios.

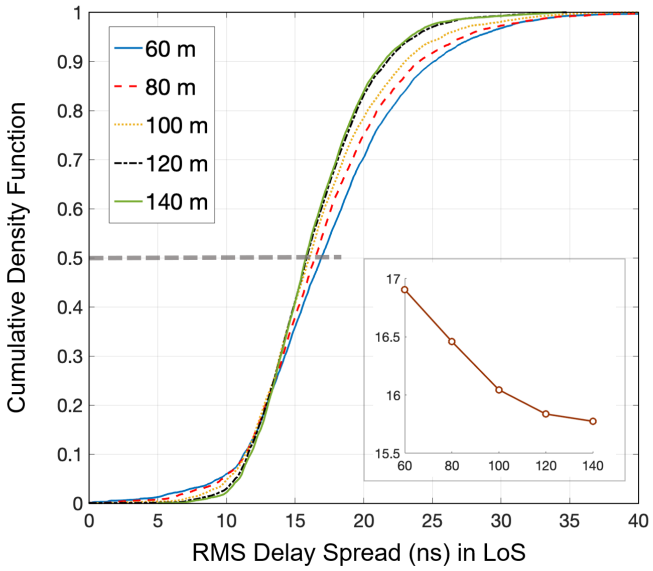

(a) CDF of delay spread in LoS

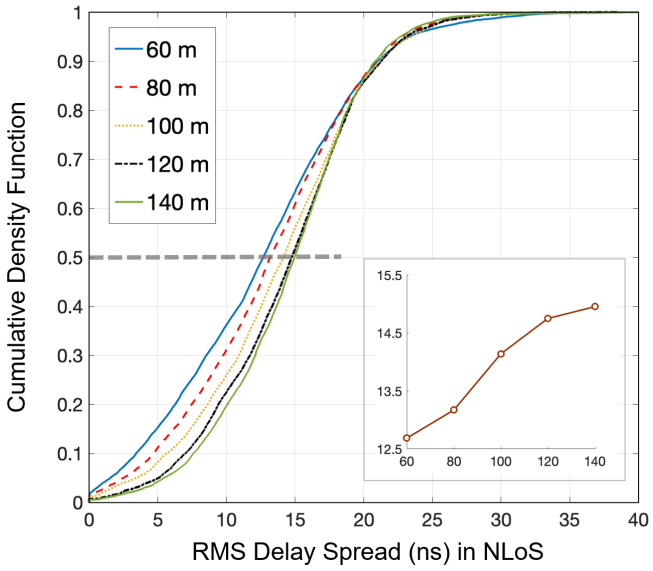

(b) CDF of delay spread in NLoS

Figure 2.10: CDF of delay spread in both LoS and NLoS scenarios, and the gray dash line marks the median value of delay spread. The subfigure highlights the variation of these median value as a function of UAV altitudes.

The second observation is caused by the particular geometry of the ATG channels. In LoS scenarios, both LoS power and MPC power are attenuated severely due to the higher path loss at higher UAV altitude. However, the energy loss of the MPC is more significant

compared to the LoS path. Consequently, the portion of the power from multipath in the total received power decreased, the LoS component is getting more dominant, leading to a reduction in delay spread. In NLoS scenarios, the delay spread increases as UAV height increases since it becomes visible to more scattering objects at greater altitudes. Although all MPCs suffer from high path loss, the emerging multipath still contributes a significant amount of energy. Therefore, the portion of scattered power in the total received power increased, resulting in a higher delay spread.

Noted that the delay spread above corresponds to measurements made with infinite bandwidth (i.e. each received ray corresponding to a perfect impulse in the time domain). Since the use of a finite bandwidth in real-world scenarios may introduces some variability into the measured delay profile, we also compute the delay spread with a finite bandwidth (for 30 MHz and 100MHz) and displayed in Figure 2.11.

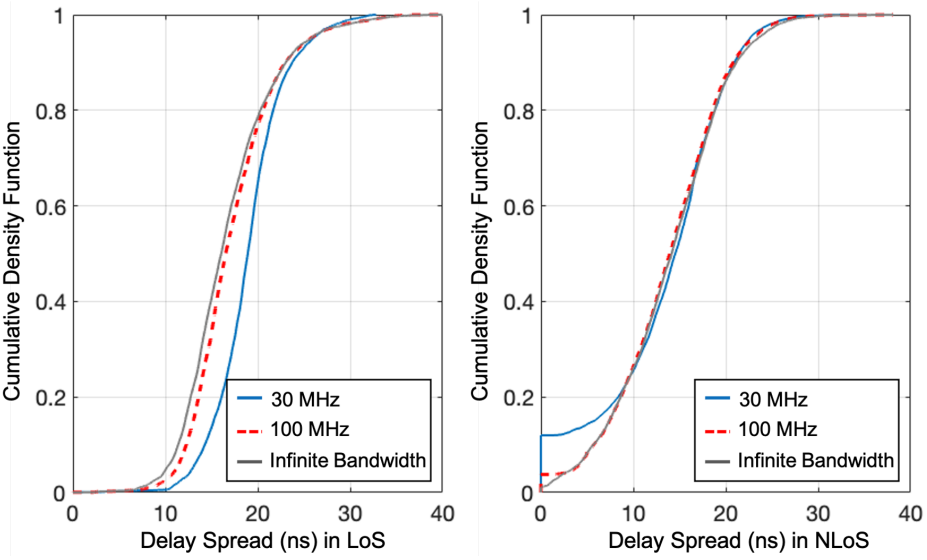

(a) (b)

Figure 2.11: CDF of delay spread with a finite bandwidth

Figure 2.11 shows that in LoS scenarios, the delay spreads with a finite bandwidth slightly increases than the infinite bandwidth. The median delay spread varies from 16.04 ns at infinite bandwidth to 18.92 ns at 30 MHz. This can be explained by the fact that the finite bandwidth leads to limited time resolution. Although we see a slight increase

in the delay spread, this increase remains rather limited. In NLoS scenarios, the delay spreads with a finite bandwidth does not differ significantly in both their shape and value. In addition, the delay spreads in LoS scenarios are still larger than the delay spreads in NLoS scenarios.

2.4.6 Angular/Delay spread versus UAV-MT distance

In conventional cellular networks, the dependence of angular spread and delay spread on BS-MT distances is well studied in the literature [74, 75, 76]. For example, the delay spreads vary monotonically with increasing link distance in urban microcells [74]. Motivated by these observations, we have investigated the correlation between angular/delay spread on UAV-MT distances. As mentioned in section 2.2, a total of 50000 snapshots have been collected for a given UAV altitude. Here we take the UAV altitude at 100 m as an example: the UAV-MT Euclidean distance varies from 112 m to 644 m. First, we collect the snapshots under different UAV-MT distances from 120 m to 630 m, with a resolution of 30 m. For both LoS and NLoS scenarios, a total of 18 clusters are created, and all snapshots in each cluster have the same propagation distance. There is a minimum of 20 snapshots in each cluster to avoid statistic bias. Next, we calculate the absolute median value of angular and delay spread for each cluster. The variations with UAV-MT distance, for both LoS and NLoS scenarios, are plotted in Figure 2.12.

It can be seen from the figure that all curves behave randomly with increasing UAV-MT distance. Therefore, although a similar consistent correlation between the angular/delay spread and the UAV-MT distance (or large scale fading such as path loss) is expected, our simulation results suggest that this correlation in the ATG channel may not be straightforward as found in ground channels. In other words, the dependence of the angular/delay spread on the UAV-MT distance is not clear. Moreover, angular spreads at the arrival vary slightly within the range of $[0.5^\circ \sim 3.5^\circ]$, where angular spreads at the departure vary much more significantly, up to $\pm 20^\circ$. These observations are analyzed in the following.

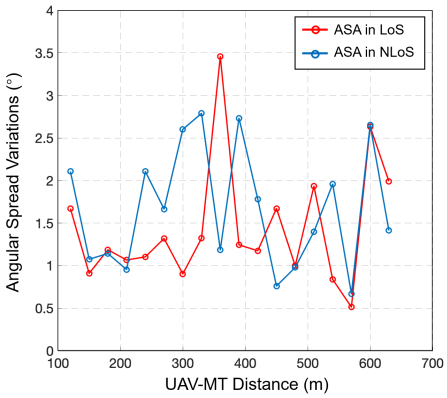

(a) ASA Variation with Distance

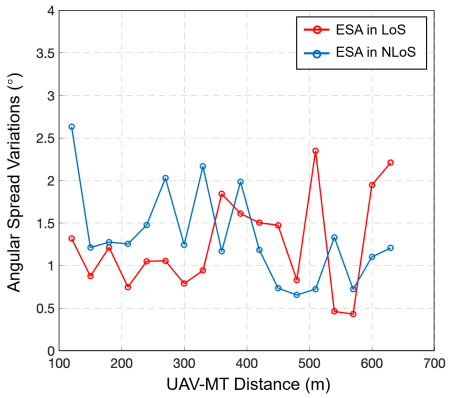

(b) ESA Variation with Distance

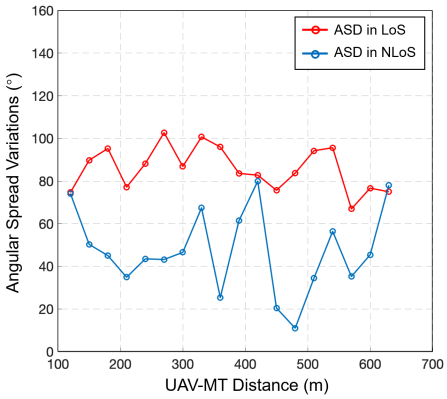

(c) ASD Variation with Distance

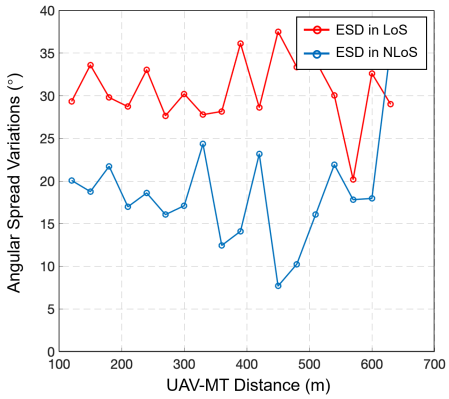

(d) ESD Variation with Distance

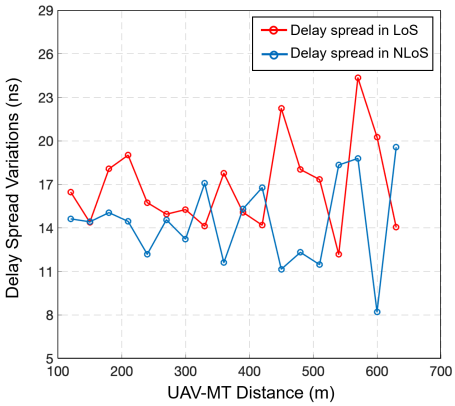

(e) Delay Spread Variation with Distance

Figure 2.12: Median value of angular/delay spreads with a function of UAV-MT Distance.

For a fixed UAV altitude, a shorter UAV-MT distance usually indicates a higher received power intensity due to limited path loss. However, the value of angular spread and

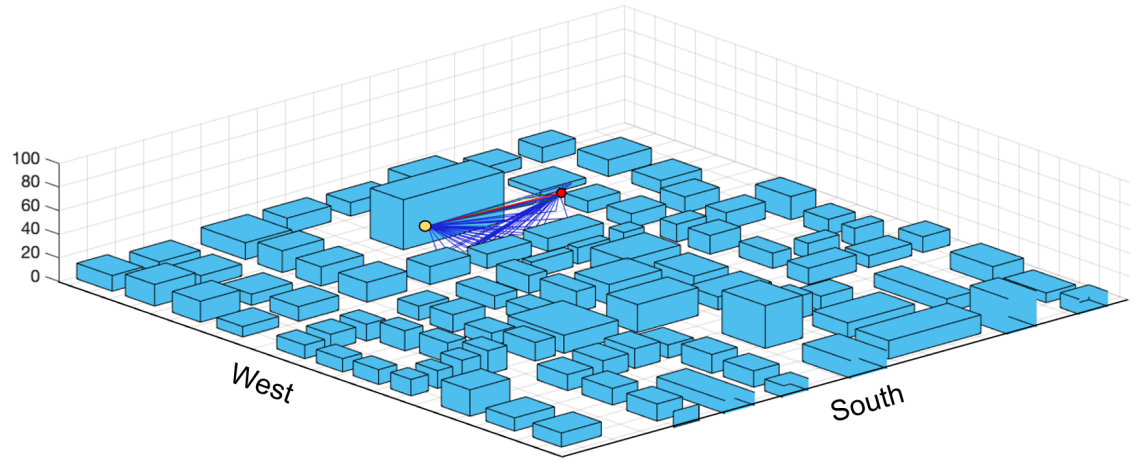

(a) Ray Distribution under near UAV-MT distance (269.7 m)

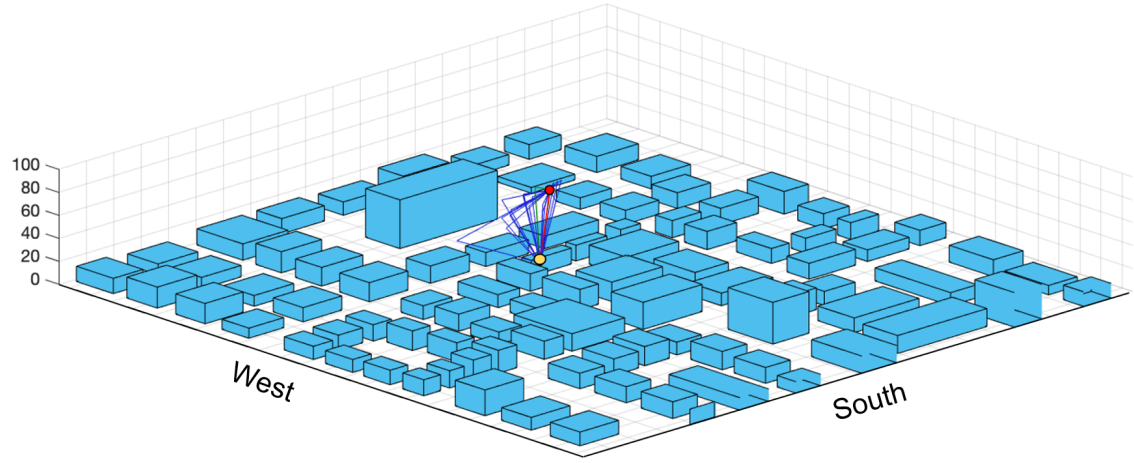

(b) Ray Distribution under medium UAV-MT distance (403.8 m)

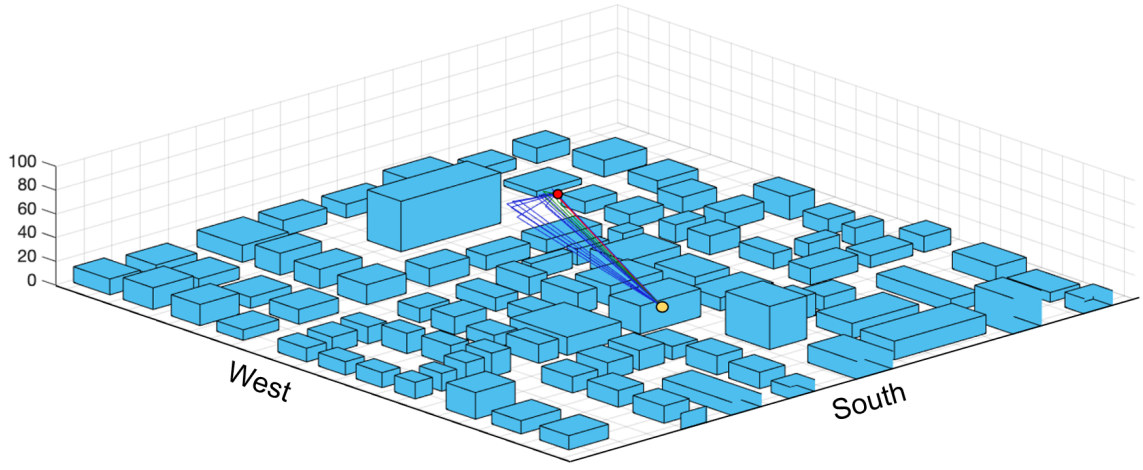

(c) Ray Distribution under far UAV-MT distance (487.6 m)

Figure 2.13: The change of ray distribution with increasing UAV-MT distance, where the red solid circle represents the MT and the yellow solid circle represents the UAV. The solid red line is the simulated line-of-sight path and the blue lines are multipath components

delay spread represents the angular/delay dispersion and multipath richness of the channel, which is not concerned with the absolute amount of incident power; The incident angle and propagation time of individual MPCs are not distance-dependent only but rely on many complex factors, including the position of scatterers, the height of walls, etc. Thus, the power distribution of the total received signal in the angular and time domain is dominated by the propagation environment, and a strong fluctuation of angular spread can occur even for very similar distances. Therefore, it is difficult to depict the tendency of their variations with increasing UAV-MT distance.

To explain this observation, Figure 2.13 displayed the simulated snapshot for a fixed MT position with UAV-MT distance at 269.7 m, 403.8 m and 487.6 m, respectively. When the UAV serves at a near position, as shown in Figure 2.13a, it can be seen that the multipath components are received from a broad angular range: a significant amount of MPC is generated due to scattering from the adjacent wall and ground surface, at the south side of the transceiver, where some extra MPCs are contributed by the buildings on the north side of the MT. Since the power of LoS is dominating, the portion of the power from the scattered MPCs in the total received power is limited, resulting in a relatively small angular spread at (ASD, ESD) = $(95.56^\circ, 28.85^\circ)$. When the UAV serves at 403.8m, as shown in Figure 2.13b, the power arrival through the direct ray decreased due to a larger path loss. Besides, MPCs provided by buildings on the south side are blocked, and only a handful of paths reflected from scatterers on the north side of the MT. These MPCs arrive with less divergent azimuth directions and create a strong cluster, which spans the power profile into two main parts among the azimuth domain. Therefore, the MPCs gain a higher relative impact in the total received power, which caused the ASD to increase to 105.57°. On the other hand, due to the distinctive features of the ATG channel geometry, the elevation angle of the MPCs becomes increasingly close to that of the LoS ray with increasing UAV-MT distance. As a result, the elevation spread ASD behaved differently and kept a similar value at 28.51°. While the UAV-MT distance increases to 487.6 m, the MPCs path becomes longer relative

to the LOS and is attenuated more, which provides less contribution for the total power and makes the angular spread drop to (ASD, ESD) = $(101.42^{\circ}, 14.63^{\circ})$. Therefore, the variation of angular/delay spread with increasing distance is significantly affected by local scatterers. Therefore, the correlation between the spatial/temporal dispersion and UAV-MT distance does not show a systematic trend.

2.5 Conclusion

In this chapter, we performed a detailed investigation of the ATG channel characteristics for UAV-based communication networks. To study the spatial and temporal properties of the urban city environment, we modeled a UAV-based wireless channel by using ray-tracing simulation tools. We focus on the parameters including angular spreads and delay spreads (at the UAV and the MT) as functions of LoS visibility, UAV altitudes, and UAV-MT distances. Some interesting observations are found and are summarized as follows:

1) In urban environments, the angular spread at the UAV is minimal. Also, the weighted mean AOA and EOA are a good representation of the real bearing to the ground user. Therefore, DoA-based estimation is suitable for UAVs to locate ground targets since the estimated DoA is close to the true DoA due to small angular spreads.

2) The PDF of ASA and ESA can be modeled with Lognormal distributions for both LoS and NLoS scenarios. Also, the value of ASA and ESA in NLoS scenarios is slightly larger than in the LoS scenarios.

3) In LoS scenarios, the value of ASA and ESA drops with increasing UAV altitudes, while this trend is not found in NLoS scenarios.

4) Contrary to conventional ground cellular channels, the angular spreads and delay spread at the MT are larger in LoS than NLoS situations, which could be explained by the particular geometry of the ATG channels.

5) The PDF of ASD and ESD in LoS scenarios can be modeled with Truncated normal distributions, while the ASD and ESD in NLoS scenarios can be modeled with Nakagami distributions.

6) Contrary to conventional ground cellular channels, the angular spreads and delay spread at the MT are larger in LoS than NLoS situations, which could be explained by the particular geometry of the ATG channels.

7) The delay spread in LoS scenarios and NLoS scenarios vary substantially with increasing UAV altitudes. In LoS scenarios, the delay spread shows a decreasing trend with increasing UAV altitudes. On the contrary, in NLoS scenarios, the delay spread tends to increase monotonically with the UAV altitudes.

8) The dependence of the angular/delay spread on the UAV-MT distance does not show a particular trend since the multipath distribution is significantly affected by local scatterers.

Based on these observations, we consider the DoA estimation has excellent potential in UAV-based localization. The next chapter proposes a novel DoA-based localization method without the requirements for multiple antenna arrays. This approach is suitable for platforms with significant form factor constraints, including UAVs, autonomous cars, and portable electronic devices.

CHAPTER 3

VIRTUAL ANTENNA ARRAY SYSTEM FOR DOA ESTIMATION

Estimating the DoAs of impinging wavefronts based on the set of signals received at an antenna array is important in fields such as radar, sonar, electronic surveillance, and wireless communication. Emitter localization based on DoA estimates usually provides good accuracy when the line-of-sight (LoS) visibility is guaranteed [34]. It also has good potential for feasibility without time synchronization requirements among transceivers [77]. Chapter 2 has shown that the angular spreads at aerial base stations are negligible, which is promising for applying DoA-based approaches to localize ground users.

Despite numerous attractive applications, accurate DoA estimation is challenging to realize with commodity mobile RF devices due to its requirement for large antenna arrays. In principle, an antenna array consists of a group of similar antennas that are spaced in a regular manner, where the element spacing is usually smaller than half a wavelength [28]. While the resolution of an antenna array increases with the number of antenna elements, it also leads to higher cost and physical size [78]. In addition, each antenna in an antenna array needs its own RF front-end and analog-to-digital converters (ADC), which increases the power consumption of the overall device. However, most commercial mobile devices are installed with only a limited number of antennas due to form factor limitations, such as wearable customer electronics, mobile phones, and UAVs, making it impractical to carry heavy antenna arrays and derive precise phase measurements directly [51, 79].

In this thesis, we propose a novel DoA estimation method called "virtual antenna array". Compared with conventional direction-finding systems relying on physical multi-antenna arrays, this method only utilizes a single-antenna device to estimate DoA. The system assumes that an unknown source periodically broadcasts an RF signal while the receiver antenna moves to various locations and measures the radio signal at those loca-

tions. Hence a virtual antenna array is implicitly created, and the DoA can be estimated by analyzing the phase differences along the receiver's trajectory. A comparison between the conventional antenna array and the proposed virtual antenna array is depicted in Figure 3.1.

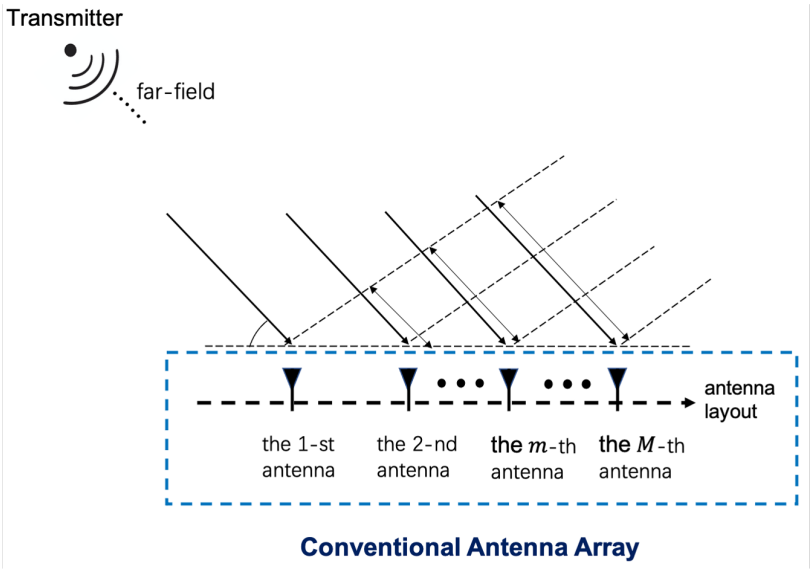

(a)

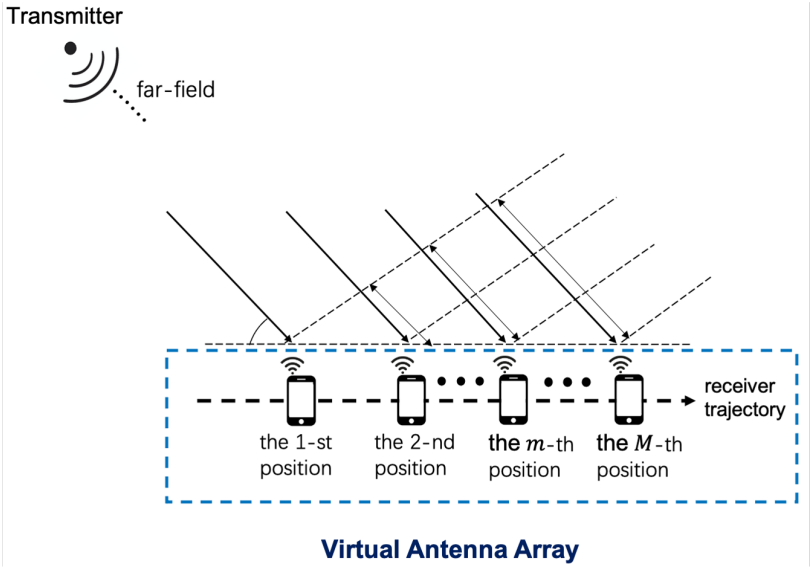

(b)

Figure 3.1: Comparison between Conventional Array and Virtual Array

The difficulty of the virtual array system is twofold: 1) the relative positions of the receiver need to be estimated with high accuracy (a fraction of a wavelength) to know

the location of the virtual antenna elements; 2) the cumulative phase distortions caused by imperfect oscillators in transmitters and receivers need to be addressed, i.e., the local oscillator (LO) frequency offset [80]. Detailed explanations and solutions are provided in Section 3.2.

The concept of virtual arrays has many similarities with Synthetic Aperture Radar (SAR). The SAR transmitters are mounted on a moving platform, such as an aircraft, or a satellite, where a static receiver uses the received signal to reconstruct the radar image of the illuminated environment [81, 82]. The direct signal between the radar transmitter and the receiver is used to calibrate for the LO frequency offset. Instead of using radar imaging, the proposed virtual array system aims to implement SAR with cellular technology. Another closely related technology is the wireless channel sounding measurements [56, 83, 84, 85], where the receiver is mounted on linear or rotational stages to create re-configurable, arbitrary 3D arrays. In these papers, the transmitter and receiver are synchronized through cables to avoid phase drifts due to LO offset, which is unsuitable for portable electronics. The array movement is precisely performed with dedicated turntables to get receiver trajectories.

Some prior research on virtual arrays can be found in [79, 86, 78], where arbitrary movements are considered to create the antenna elements of the virtual array. The relative coordinates of the virtual array elements are estimated from receiver-embedded IMUs, similar to what will be proposed in our work. However, the LO offset in these papers is considered to be a negligible value, resulting in a relatively small phase drift. This assumption can be achieved when both transmitter and receiver are equipped with expensive, high-stability rubidium local oscillators which are impossible in low-cost consumer electronics.

Compared with conventional multi-antenna arrays, the virtual array DoA estimation method presented in this thesis aims at being feasible with cheap, off-the-shelf hardware, which typically has a significant LO frequency offset between the transmitter and the re-

ceiver. The proposed approach is suitable for portable electronics and UAV-based communications as it does not require time synchronization and complex hardware modifications.

The work in this chapter progresses as follows. Section 3.1 introduces the concept of traditional DoA estimation techniques, including the subspace-based algorithm called MUSIC (Multiple Signal Classification). The MUSIC algorithm is the DoA estimation algorithm we use in this thesis, although other methods could be used as well. The system design and problem statement for the virtual antenna array system are presented in Section 3.2. The two main difficulties of the virtual antenna array, i.e., LO frequency offset compensation and receiver trajectory reconstruction using IMU sensor measurements, are discussed in Section 3.2 and Section 3.3, respectively. In Section 3.4, we present a proof-of-concept model designed in previous publications. The conclusion is summarized in Section 3.5.

3.1 Principle of DoA Estimation

3.1.1 Problem Formulation

The principle of general DoA estimation problems is to extract DoA information from the phase response measured by the sensor array [87]. A representative example is depicted in Figure 3.2, where there are N signal sources and an array with M antenna elements. The objective is to estimate the azimuth angle of the emitted signal when it arrives on the array. For simplicity, the signal sources are in far-field; hence the wavefronts generated by each source arrive at all the elements from an identical direction. The receiver antennas are assumed to be aligned uniformly along a line. Moreover, we will focus on the narrowband case, where the envelope of the signal remains approximately constant as the signal wavefront propagates through the array. This assumption is often satisfied when the highest frequency in propagated signals is much less than the carrier frequency [34].

Assuming the plane wave signal generated by the n-th source impinges on the array at an angle θ and the propagated narrowband signal is $s(t)$. It travels a certain distance to

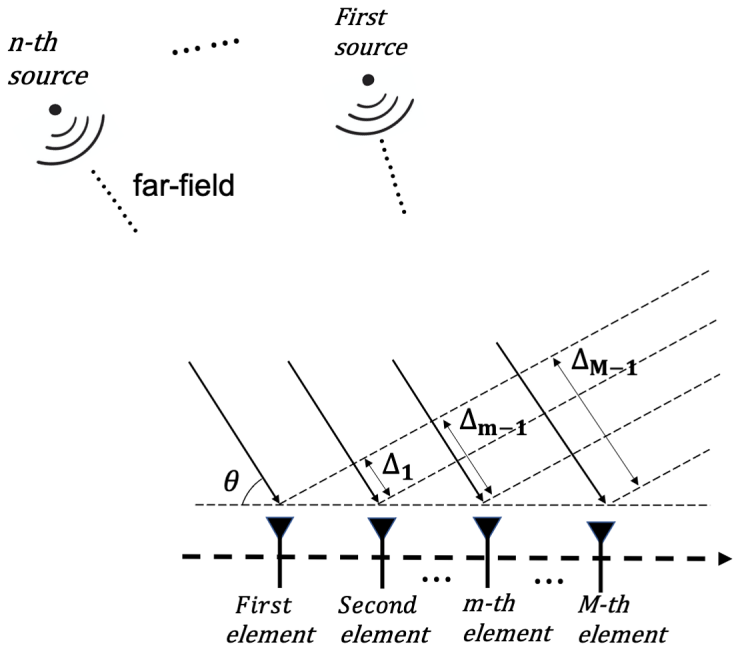

Figure 3.2: Model for DoA estimation of N sources with a linear array of the M elements.

reach the leftmost antenna as the reference element. The complex RF signal received at the reference element can be written as:

$$r(t) = s(t) \cdot e^{j \cdot 2\pi f_c \cdot t} \tag{3.1}$$

where f_c represents the carrier frequency and t represents the propagation time. Since other array elements are distributed on a line, the signal traveling to the m-th element will take an extra distance Δ_{m-1} and therefore a corresponding delay. The delay τ_m is a function of the source direction θ of the n-th signal and the position of the m-th array element with respect to the reference element. Therefore, τ_m can be driven as:

$$\tau_m = \frac{\Delta_{m-1}}{c} = \frac{d_{m-1} \cdot \cos\theta}{c} \tag{3.2}$$

The d_{m-1} is the spacing between the m-th element and the reference element, which is usually known when designing the antenna array. By considering the phase of the reference

antenna to be zero, the τ_m introduces an additional phase shift $e^{j\cdot 2\pi f_c \cdot \tau_m}$ to the received signal on the m-th element. By taking into account the above assumption, the received signal at the output of the m-th element can be written as:

$$\begin{aligned} x_m(t) &= r(t) \cdot e^{j\cdot 2\pi f_c \cdot \tau_m} \\ &= r(t) \cdot e^{j\cdot \frac{2\pi}{\lambda} \cdot d_{m-1} cos\theta} \end{aligned} \tag{3.3}$$

where the λ is the signal wavelength. Using vector notation, the output from all the M array elements due to the n-th source can be expressed as:

$$\begin{aligned} \mathbf{x(t)} &= [x_1(t), x_2(t), \cdots, x_M(t)]^T \\ &= r(t) \cdot \begin{bmatrix} e^{j\cdot \frac{2\pi}{\lambda} \cdot d_0 cos\theta} \\ e^{j\cdot \frac{2\pi}{\lambda} \cdot d_1 cos\theta} \\ \cdots \\ e^{j\cdot \frac{2\pi}{\lambda} \cdot d_{M-1} cos\theta} \end{bmatrix} \\ &= \mathbf{a}(\theta) \cdot r(t) \end{aligned} \tag{3.4}$$

The vector $\mathbf{a}(\theta)$ is referred as the "array manifold", which characterizes the array response to a unit amplitude signal [88]. It is clear from Eq. (3.5) that the $\mathbf{a}(\theta)$ contains information about the geometry of the array and the direction of the incident waves. The graphical representation of $\mathbf{a}(\theta)$ with respect to the depicted case is shown in Figure 3.3: a curve lying in a one-dimensional surface, and the curve returns to its starting point when θ returns to its initial value [89]. As for cases when there are multiple unknown elements (e.g., the elevation angle, the signal carrier frequency) that make contributions to the phase shift, the array manifold will be a continuum which lies in a multiple-dimensional space. Most subspace-based direction-finding algorithms involve searching over the array manifold for response vectors that satisfy a given criterion. For example, in the case of the MUSIC algorithm, the manifold is searched to find vectors that are orthogonal to the esti-

mated noise subspace [58], which will be explained in subsection 3.1.2.

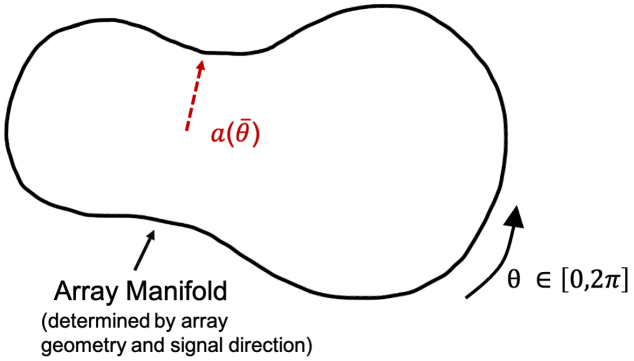

Figure 3.3: One-dimensional array manifold [89].

With no loss of generality, the total complex output of an M-element array $\mathbf{X(t)}$ due to the N sources can be described by the following equation:

$$\begin{aligned} \mathbf{X(t)} &= [\mathbf{a}\,(\theta_\mathbf{1}), \ldots, \mathbf{a}\,(\theta_\mathbf{N})]\, s(t) \\ &= \mathbf{A}\,(\theta) s(t) \end{aligned} \tag{3.5}$$

and $\mathbf{A}\,(\theta)$ is a $M \times N$ matrix, which is composed of the array manifolds associated with N emitters, and often named as "steering vector".

Based on the structure of Eq. (3.5), it can be seen that when N emitters are present, the array output $x_m(t)$ from the m-th array element is a linear combination of the columns of $\mathbf{A}\,(\theta)$. Figure 3.4 depicted a case where two emitters and an array of four antenna elements are present. The four array outputs $x_1(t), \cdots, x_4(t)$ both lie in a subspace spanned by $\{\mathbf{a}\,(\theta_\mathbf{1}), \mathbf{a}\,(\theta_\mathbf{2})\}$. In other words, the array manifold intersects the subspace at only two points, each corresponding to a response vector of one of the emitters. As indicated in the figure, the term **signal subspace** is used to denote this subspace [88]. The description above can be concluded as follows: for N uncorrelated emitters, the signal component of the array output is confined to a N dimensional subspace which is determined by the N emitter positions. The parameter of interest θ can be estimated as long as the signal

subspace is determined.

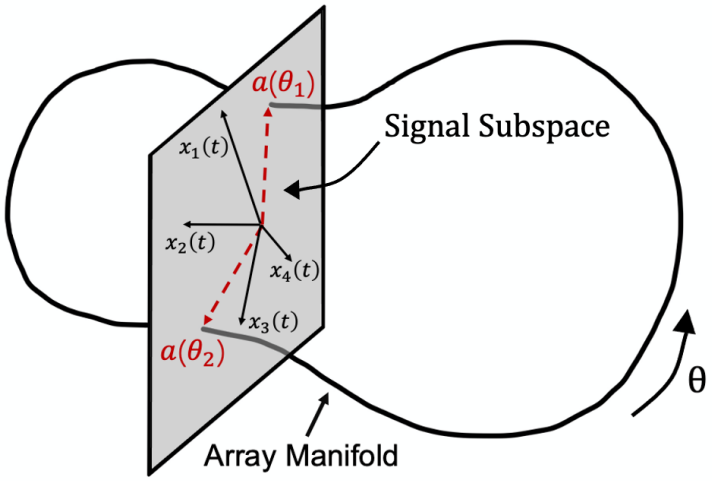

Figure 3.4: A Geometric View of Signal Subspace

In real-world applications, the array output $\mathbf{X(t)}$ usually contains additional noise introduced through hardware [89] as :

$$\mathbf{X(t)} = \mathbf{A}\,(\theta)s(t) + \mathbf{n(t)} \tag{3.6}$$

where $\mathbf{n(t)} = [n_1(t), n_2(t), \cdots, n_M(t)]^T$. As the noise is usually assumed to possess energy in all dimensions of the observation space, the matrix $\mathbf{X(t)}$ defined above will be full rank (although the signal components are still restricted to N-dimensional subspaces).

3.1.2 Subspace Estimation and MUSIC algorithm

The estimation of the signal subspace is usually based on the spatial array covariance matrix with respect to the measured array output [32]. Considering that the noise is spatially white and statistically independent of the source signals, then the $M \times M$ theoretical covariance matrix $\mathbf{R_{xx}}$ of the array output vector $\mathbf{X(t)}$ can be written as:

$$\begin{aligned} \mathbf{R_{xx}} &= E\left\{\mathbf{X(t)X^H(t)}\right\} \\ &= \mathbf{A}\,(\theta)\mathbf{R_{SS}}\mathbf{A}^H(\theta) + \sigma^2 I \end{aligned} \tag{3.7}$$

where the $N \times N$ matrix $\mathbf{R_{SS}} = E\left\{s(t)s^H(t)\right\}$ is the source covariance matrix, which is diagonal in the case of uncorrelated signals [87]. The rank of the matrix $\mathbf{A}(\theta)\mathbf{R_{SS}}\mathbf{A}^H(\theta)$ is $M - N$. The σ^2 represents the additive noise variance where I is a $M \times M$ identity matrix, $E\{\cdot\}$ denotes the statistical expectation and $(\cdot)^H$ is the Hermitian transpose. The eigendecomposition of $\mathbf{R_{xx}}$ is provided by:

$$\mathbf{R_{xx}} = \sum_{k=1}^{M} \lambda_k e_k e_k^H \tag{3.8}$$

where λ_k and e_k are the eigenvalues and corresponding eigenvectors of $\mathbf{R_{xx}}$. Let the eigenvalues λ be sorted in descending order, since the structure of $\mathbf{R_{xx}}$ given in Eq. (3.7) is bascially a $M-N$ matrix plus a identity matrix scaled by σ^2, the $M-N$ smallest eigenvalues are approximately repeated, i.e., $\lambda_{N+1} \approx \cdots \approx \lambda_M \approx \sigma^2$. The N largest eigenvalues λ_k, $1 \leq k \leq N$, are referred to as the signal eigenvalues where the rest λ_k, $N+1 \leq k \leq M$, are refered to as the noise eigenvalues [34]. We define $\mathbf{E_S} = [e_1, e_2, \cdots, e_N]$ and $\mathbf{E_N} = [e_{N+1}, e_{N+2}, \cdots, e_M]$. In this case, the column span of $\mathbf{E_S}$ is the signal space eigenvectors, and the $\mathbf{E_N}$ is the noise subspace eigenvectors which are orthogonal to $\mathbf{E_S}$ [88, 58].

The target DoA is determined by searching over the array manifold vectors to find $\hat{\theta}$ which allows $\mathbf{A}(\hat{\theta})$ belonging to the estimated signal space (or orthogonal to the estimated noise subspace) [32]. The Multiple Signal Classification (MUSIC) estimator is one of the most well-known methods to find the parameter estimate $\hat{\theta}$, with the advantage of high-resolution capability and robustness to array geometry [90]. More specifically, MUSIC is a scalar measure of the distance between the array manifold and the estimated noise subspace [87]. The reciprocal of this distance can be written as:

$$P_{MUSIC}(\theta) = \frac{1}{\mathbf{A^H}(\theta)\,\mathbf{E_N}\mathbf{E_N^H}\mathbf{A}(\theta)} = \frac{1}{\mathbf{A^H}(\theta)\,(\mathbf{I} - \mathbf{E_S}\mathbf{E_S^H})\mathbf{A}(\theta)} \tag{3.9}$$

and the locations of the N largest peaks of the so called MUSIC spectrum P_{MUSIC} give the

best estimates for the target $\hat{\theta}$:

$$\hat{\theta} = argmax \frac{\mathbf{A^H}(\theta)\,\mathbf{E_S}\mathbf{E_S^H}\mathbf{A}(\theta)}{\mathbf{A^H}(\theta)\,\mathbf{A}(\theta)} \tag{3.10}$$

In summary, the solution for the parameters of interest (e.g., θ) can be found as the intersection of the array manifold and the determined subspace, as depicted in Figure 3.4. In practical scenarios where the noise is present, the fundamental principle of DoA estimation becomes searching over the array manifold $\mathbf{A}(\theta)$ to find a vector that is orthogonal to the estimated noise subspace. The accuracy of the DOA estimates is dependent on how accurately the signal/noise subspace is estimated [58]. For the sake of clarity, the approach taken by conventional subspace-based DoA estimation algorithms can be concluded as a three-step procedure:

(1) Construct a suitable parametrization steering vector A for all parameters of interest (e.g., θ) based on the knowledge of the array geometry;

(2) Estimate the signal subspace and the noise subspace based on the array output.

(3) Estimate θ based on the MUSIC spectrum.

3.2 System Design of Virtual Antenna Arrays

In this section, we present the system model used for DoA estimation with the virtual antenna array. We briefly cover the different algorithms used for DoA estimation proposed in [80, 91] that will be used in this thesis.

3.2.1 System model

The system model of the virtual antenna array is the following. We consider a simple case where a single source broadcasts an RF signal periodically while the receiver is moving along a linear trajectory, as shown in Figure 3.5. The source is located far from the receiver,

and the signal impinges on the virtual array elements at an equal direction θ (far-field approximation). The periodically transmitted signal is in the form of digital data packets. Both the source and the receiver know the preamble of these packets. Those preambles are defined by common communication standards, e.g., the Primary Synchronization Signal (PSS) broadcast by the base stations in Long-Term Evolution (LTE) standard [92]. The receiver can correlate its received baseband samples with the known preamble sequence to determine the boundaries and the phase of the received packets.

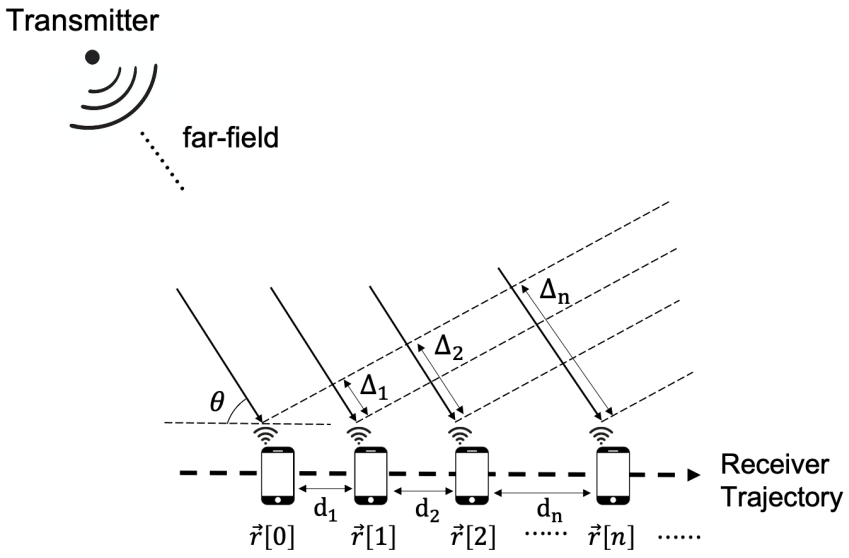

Figure 3.5: Virtual array concept for DoA estimation. A single receiver moves along its trajectory (e.g., from $\vec{r}[0]$ to $\vec{r}[n]$) and captures multiple transmitted signals, thereby creating a virtual array.

Let us denote $s\big[m\big]$ the baseband representation of the transmitted packet preamble (for $m = 1, ..., M$) and $r\big[n, m\big]$ the m-th baseband sample of the n-th received packet (for $n = 1, ..., N$). We take the receiver position when receiving the initial packet as the reference array element $\vec{r}[0]$; the position of the receiver (x_n, y_n) when receiving the n-th packet depends on the movement of the receiver, denoted as the array element $\vec{r}[n]$.

For simplicity, we focus on a narrowband, line-of-sight (LoS) channel, therefore the

received signal at the reference element can be represented as:

$$r[0,m] = \alpha \cdot s\,[m] \cdot e^{j\psi_0} + \omega\,[n,m] \tag{3.11}$$

where α is complex amplitude of the channel; ψ_0 is the phase of the first received packet and remains constant between multiple received packets; $\omega\big[n,m\big]$ is an independent and identically distributed Gaussian noise with distribution $\omega\big[n,m\big] \sim \mathcal{CN}(0,\sigma^2)$. As shown in Figure 3.5, when the receiver moves from $\vec{r}\,[0]$ to $\vec{r}\,[n]$, the signal will experience an extra distance Δ_n, as well as an additional delay $\tau_n = \frac{\Delta_n}{c}$. The additional delay leads to a phase shift for the received signal as:

$$\begin{aligned} r[n,m] &= \alpha \cdot s\,[m] \cdot e^{j\psi_0} \cdot e^{j\cdot 2\pi f_c \cdot \frac{\Delta_n}{c}} + \omega\,[n,m] \\ &= \alpha \cdot s\,[m] \cdot e^{j(\psi_0 + \frac{2\pi}{\lambda}\cdot\Delta_n)} + \omega\,[n,m] \end{aligned} \tag{3.12}$$

where $\lambda = c/f_c$ denotes the wavelength corresponding to the carrier frequency f_c.

Ideally, the phase difference of the observed signal between each virtual array element is equal to the phase shift due to Δ_n in Eq.(3.12). In other words, the DoA could be estimated by measuring the phase difference of the received signal if Δ_n is known. In conventional DoA estimation systems, antenna positions are fixed and Δ_n can be easily calculated according to the array geometry [93]. For example, antenna elements in Figure 3.5 are arranged in a straight line, the extra distance Δ_n can be calculated as:

$$\Delta_n = x_n cos(\theta) + y_n sin(\theta) \tag{3.13}$$

As for the virtual array system, the array does not have a constant geometry and the Δ_n depends on the movement of the receiver. Therefore, it is necessary to estimate the relative position of the receiver with high accuracy (usually a fraction of a wavelength), which is the first difficulty of our proposed system.

The other difficulty is the actual phase difference measured on the virtual array element includes not only the phase shift as described above. The transmitter and the moving receiver obtain their RF carrier signal from a separate local oscillator. These two oscillators usually have a non-zero frequency offset f_0 with respect to each other due to manufacturing tolerances and temperature variations. In addition, all oscillators undergo random phase and frequency drifts over time. Therefore, with the presence of f_0, the real output at the virtual array element in realistic scenarios is expressed as:

$$r\left[n,m\right] = \alpha \cdot s\left[m\right] \cdot e^{j(\psi_0 + \frac{2\pi}{\lambda} \cdot \Delta_n + 2\pi f_0 \cdot (t_n + mT_s))} + \omega\left[n,m\right] \tag{3.14}$$

where t_n is the elapsed time between the initial packet and the n-th packet, T_s is the receiver sample period.

Our system assumes that the value of f_0 does not change over time, which is approximately true for only short periods: a few seconds for low-quality temperature-controlled crystal oscillators (TCXO) and a few tens of seconds for high-quality oven-controlled crystal oscillators (OCXO) [80]. Moreover, the effect of LO phase noise is negligible compared to the LO frequency offset (LO phase offset can be dozens or hundreds of times higher than LO phase noise) [94]. As a result, the main difference between the received signal in a virtual array system and the received signal in a conventional antenna array is the LO frequency offset f_0 and its corresponding phase distortion.

To summarize, the goal of the proposed virtual array system is to leverage conventional DoA estimation techniques that are readily available for conventional multi-antenna arrays. Therefore, two main difficulties need to be addressed:

1. The relative position of the receiver needs to be estimated with an accuracy of a few fractions of a wavelength.

2. The frequency offset f_0 needs to be estimated and compensated for the received signal.

The algorithms and techniques to deal with these two challenges are provided in the following subsections. Note that while we use the MUSIC algorithm in this thesis, the virtual array signal model could be applied to a number of other DoA estimation algorithms, such as beamforming, root-MUSIC, etc.

3.2.2 Local Oscillator Frequency Offset Compensation Methods

To estimate and compensate the LO frequency offset in Eq. (3.14), we proposed two methods, based on our previous research in [80]. The first method is the Stop-and-Start (SaS) approach, where the receiver first stands still before moving. During standstill, only the LO frequency offset causes the phase in Eq. (3.14) to change with time and can therefore be easily estimated. This estimated value f_0 is then used during the movement of the receiver to compensate the LO frequency offset, where each received subsequent packet can be expressed as follows:

$$r'\left[n,m\right] = r\left[n,m\right] e^{-j2\pi f_0 \cdot (t_n + mT_s)} \tag{3.15}$$

The compensated signal $r'\left[n,m\right]$ contains the phase interferometry and can be used directly in conventional DoA estimation techniques. Although the SaS approach is straightforward and easy to implement, it suffers from two disadvantages. The most obvious disadvantage is that the SaS approach restricts the movement of the receiver, as the receiver first needs to stand still before moving. The second disadvantage is that the LO frequency offset should not change too much between the moment the receiver stands still and the moment the receiver moves, which might not always be verified in practice (especially for low-quality LOs).

The other method is called the joint estimation approach, which has more advantages in practical applications for providing higher usage flexibility and no need to stop the receiver before the movement. In this method, we apply the MUSIC algorithm with an adapted

signal model by including the LO phase offset into the array manifold of the virtual array. Let us rewrite Eq. (3.14) by stacking the N received packets in a column vector:

$$r\left[m\right] = \mathbf{a}\left(f_0, \theta\right) X\left[m\right] + \omega\left[m\right] \tag{3.16}$$

with the array manifold lies in a two-dimensional space over f_0 and θ and defined as:

$$\mathbf{a}\left(f_0, \theta\right) = \begin{bmatrix} e^{j(2\pi f_0 t_1 + \frac{2\pi}{\lambda}(x[1]\cos(\theta) + y[1]\sin(\theta)))} \\ e^{j(2\pi f_0 t_2 + \frac{2\pi}{\lambda}(x[2]\cos(\theta) + y[2]\sin(\theta)))} \\ \vdots \\ e^{j(2\pi f_0 t_N + \frac{2\pi}{\lambda}(x[M]\cos(\theta) + y[M]\sin(\theta)))} \end{bmatrix} \tag{3.17}$$

and $X\left[m\right]$ is constant for all virtual antennas, defined as

$$X\left[m\right] = \alpha_0 \cdot s\left[m\right] \cdot e^{j(\psi_0 + 2\pi f_0 m T_s)} \tag{3.18}$$

By developing the eigen-decomposition of the covariance matrix of $r\left[m\right]$, we can find the corresponding noise subspace $\mathbf{E_S}$ and define the MUSIC spectrum as:

$$P_{MU}\left(f_0, \theta\right) = \frac{1}{\mathbf{a}^H\left(f_0, \theta\right) \mathbf{E_S} \mathbf{E_S}^H \mathbf{a}\left(f_0, \theta\right)} \tag{3.19}$$

then the nominal DoA and frequency offset $\left(\hat{f}_0, \hat{\theta}\right)$ can be estimated with a two-dimensional MUSIC search. The major drawback of the joint estimation is that certain receiver trajectories do not allow to estimate DoA jointly with LO offset f_0, as will be investigated in more detail in Chapter 4.

3.2.3 Receiver Trajectory Reconstruction Methods

The second challenge of virtual antenna arrays lies in estimating the relative position of the receiver along its trajectory, which requires an accuracy of a fraction of a wavelength. The

orientation of the receiver also needs to be estimated to account for non-isotropic antenna radiation patterns. Such limitations rule out conventional GNSS systems, which do not meet the required accuracy and do not provide orientation information. In this thesis, we use a 3D inertial measurement unit (IMU) to estimate the position and orientation of the receiver.

IMUs are basic components commonly found in modern electronic devices (e.g., smartphones, vehicles, UAVs). The integration of IMUs is essential for application areas in which orientation information is indispensable and rapid collection of geographic information is required [95]. A typical commercial IMU consists of a triaxial accelerometer, a triaxial gyroscope, and sometimes a magnetometer. The triaxial accelerometer measure three-dimension linear accelerations (change of velocity) of an object. The gyroscopes measure the three-dimension angular rate of the object. The magnetometer measures the earth's gravitational and magnetic fields and can be fused in conjunction with accelerometer and gyroscope data to determine absolute heading [96]. With the knowledge of these inertial sensor measurements, the traveled distance and direction of the IMU can be determined by applying basic kinematics equations, and therefore the new position can be estimated [97]. Then the trajectory of the IMU can be reconstructed by integrating these estimated positions. The detailed IMU processing methods are illustrated in Section 3.3.

The major drawback of the IMU-based position estimation is the accumulation of sensor biases during processing, which makes the navigation solution obtained from sensor measurements drift from the real trajectory, i.e., the error of the navigation solution will increase over time. However, the movement range (and hence duration) for the virtual array should be quite limited to stay in the Wide-Sense Stationary Uncorrelated Scattering (WSSUS) assumptions required for multi-antenna array processing (typically less than ten wavelengths) [98]. As a result, for the WSSUS assumptions to hold, the time over which the receiver forms the virtual array should be short so that the navigation error incurred by the IMU is also limited. For typical pedestrian or vehicular speed, the movement duration

is typically limited to a few seconds.

3.2.4 Receiver Movement Constraints

Similar to conventional multi-antenna arrays, the virtual array systems also need to satisfy the spatial aliasing criterion, i.e., the distance between the two adjacent array elements (d_n in Figure 3.5) must be no larger than $\lambda/2$ to avoid DoA ambiguity [99]. By considering the signal model (3.14) in the proposed virtual multi-antenna system, the distance traveled by the receiver between two successive packets must be smaller than $\lambda/2$ as well. This translates to the velocity constraint for receiver as $v_n\left(t_n - t_{n-1}\right) \leq \lambda/2$, where v_n is the speed of the receiver and $(t_n - t_{n-1})$ indicates the broadcast period for the transmitted packets. In that case, the constraint becomes:

$$v_n \leq \frac{\lambda}{2\left(t_n - t_{n-1}\right)} \tag{3.20}$$

As an illustration, when a 3G base station sends a PSS sequence every 0.667 ms under a carrier frequency of 2.1 GHz [100], the maximum receiver speed is up to 385 km/h. When it comes to 5G millimeter-wave spectrum, e.g., 28 GHz defined by 3GPP-band-n257 with reduced wavelength at around 10 mm [101], the maximum receiver speed is around 29 km/h. Finally, note that non-stationary channels will cause distortion of the multipath components, which cannot be recovered with a virtual array. However, as long as the transmitter remains static during the receiver movement and only the transmitter's direction is estimated, this should not cause severe problems for the proposed system.

In summary, the DoA estimation in the virtual array is only feasible after the LO phase offset caused by f_0 is eliminated, and the relative array element positions x_n are known. The block diagram of the entire system structure is summarized in Figure 3.6. The algorithms and techniques to reconstruct trajectories and to estimate x_n are provided in the next section.

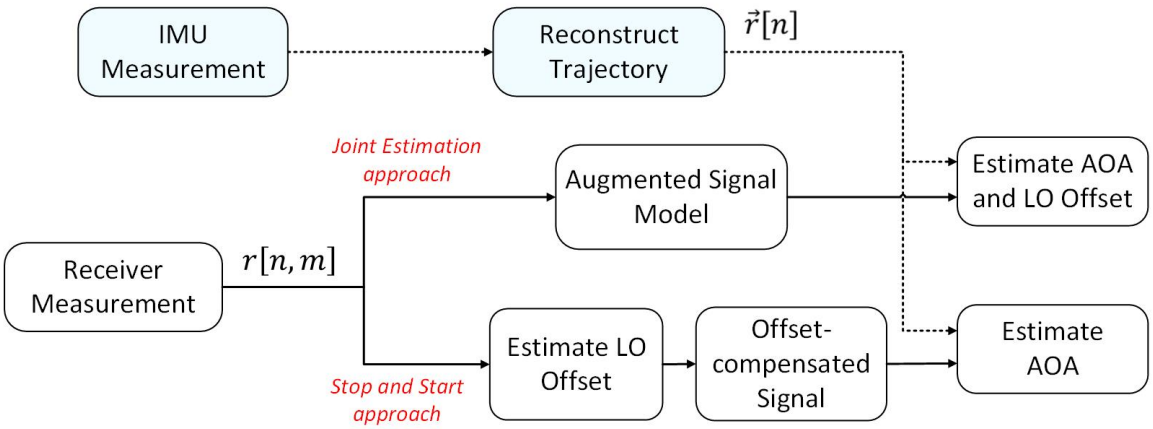

Figure 3.6: The flow diagram of the virtual antenna array system [91].

3.3 IMU processing with Non-linear Kalman Filter

The fundamental idea of IMU processing is to provide accurate and precise estimations of hidden variables (i.e., the relative position) in the presence of system uncertainty [95]. The uncertainty includes hardware biases (e.g., sensor calibration errors) and stochastic measurement errors (e.g., noisy sensor measurements) [102]. The hardware biases can be measured and accurately calibrated before the movement; the stochastic errors are difficult to compensate but can be considered as random processes [103]. Due to the accumulation of these errors, the reliability of the IMU decreases significantly over time. As a result, the Kalman Filter (KF) is widely used in IMU processing as an important estimation algorithm that estimates hidden variables based on inaccurate and uncertain measurements and reduces uncertainty or noise [104].

The KF is first proposed by Rudolph E. Kalman in 1960 [105] and is described as a recursive solution to the discrete data linear filtering problem. Its first implementation in the inertial navigation system is with a military aircraft [106]. After that, the KF has been used extensively for tracking and data fusion problems [104]. However, while the standard KF serves as the optimal linear estimator for linear system models, the system dynamics and observation equations in many real-world applications of interest are nonlinear. Thus, two extensions to the KF with respect to nonlinear systems have been proposed: the Extended

Kalman Filter (EKF) [107] and the Unscented Kalman Filter (UKF) [108]. The EKF applies the KF to nonlinear systems by simply linearizing all the nonlinear models so that the traditional linear Kalman filter algorithms can be applied [107]. The UKF uses a deterministic sampling approach to capture the mean and covariance estimates with a minimal set of sample points. It also provides superior performance at an equivalent computational complexity than the EKF [109, 110]. In the virtual array systems, the IMU measurements are converted to a relative position by using a UKF. The basic system concept of KF and the UKF derivation is given in the following subsections.

3.3.1 Basic concept of Kalman Filter

Derive System State Space Model

Assume that we want to estimate a hidden state of a system by observing some other information, e.g., estimating the position of a vehicle by observing the measurements of an IMU. Without loss of generality, the system should be able to be described by a discrete-time linear state space model as [105]:

$$\mathbf{x}_k = \mathbf{F}_{k-1}\mathbf{x}_{k-1} + \mathbf{G}_{k-1}\mathbf{u}_{k-1} + \mathbf{w}_{k-1} \tag{3.21}$$

where $\mathbf{x}_k$ is the state vector of the system at time k, which contains states that will be estimated by the KF [111]. The state vector includes the states of interest (e.g., the position) and other states that may be necessary to describe the system (e.g., the acceleration and orientation). The matrix $\mathbf{F}$ is the state transition matrix applied to the previous state vector $\mathbf{x}_{k-1}$ that represents the dynamic behavior of the system (is usually assumed stationary over time). The matrix $\mathbf{G}$ is the control-input matrix applied to the control vector $\mathbf{u}_{k-1}$; $\mathbf{w}_{k-1}$ is the uncertainty of the state space model, also called the process noise vector, and is assumed to be zero-mean Gaussian with the covariance matrix $\mathbf{Q}$ [97]. In other words, $\mathbf{w}_{k-1}$ represents the level of confidence that we have regards the state space model since

modeling errors are inevitable when deriving physical principles in equations.

Estimating the state of interest are based on observing the measurements of the sensors, and the measurements can be described by:

$$\mathbf{y}_k = \mathbf{H}_k \mathbf{x}_k + \mathbf{v}_k \tag{3.22}$$

where $\mathbf{y}_k$ is the measurement vector that are able to measure; $\mathbf{H}_k$ is the measurement matrix, and $\mathbf{v}_k$ is the measurement noise vector that is assumed to be zero-mean Gaussian with the covariance $\mathbf{R}$, which can be used to include the errors due to the sensor measurements [109].

The system state space model in Eq. (3.21) defines the dynamic of the states from time $k-1$ to time k. The output model in Eq. (3.22) describes the relationship between the states and the measurements at the current time k. Once the system state space model has been derived, it is ready to implement the KF system. Note that $\mathbf{w}$ and $\mathbf{v}$ are only used in the state space model to describe the statistics of the noises, and they typically do not appear directly in KF. Instead, the covariance matrices $\mathbf{Q}$ and $\mathbf{R}$ are used in KF to represent the process and measurement uncertainty.

Kalman Filter Algorithm

The goal of the KF is to take a probabilistic estimate of states and update them in real-time using two steps: prediction and correction. For the prediction process, the KF uses the previously estimated state $\hat{\mathbf{x}}_{k-1}$ and the previous measurement $\mathbf{y}_{k-1}$ to predict the state in time k, named as $\hat{\mathbf{x}}_{k|k-1}$ and calculated by:

$$\hat{\mathbf{x}}_{k|k-1} = \mathbf{F}_{k-1} \hat{\mathbf{x}}_{k-1} + \mathbf{G}_{k-1} \mathbf{u}_{k-1} \tag{3.23}$$

where the $\hat{\mathbf{x}}_{k|k-1}$ is called the prior estimate [105]. The subscript $k|k-1$ indicates the corresponding estimate is made for the time k based on owned information at the time

$k-1$.

The error of the prior estimate $\hat{\mathbf{x}}_{k|k-1}$ compared to the true state $\mathbf{x}_k$ is represented by a new term $\mathbf{P}_{k|k-1}$. It encrypts the error covariance that the filter thinks the prior estimate has [111]. Again, the subscript $k|k-1$ is indicating that the $\mathbf{P}_{k|k-1}$ is the expected error covariance matrix at k based on the system model and the covariance at $k-1$. The $\mathbf{P}_{k|k-1}$ can be computed during the prediction step by:

$$\mathbf{P}_{k|k-1} = \mathbf{F}_{k-1}\mathbf{P}_{k-1}\mathbf{F}_{k-1}^T + \mathbf{Q}_{k-1} \tag{3.24}$$

After the prediction process, the system performs measurement at time k and gets the measurement $\mathbf{y}_k$. The $\mathbf{y}_k$ contains some uncertainty due to imperfect sensors, with the measurement noise covariance $\mathbf{R}$ defined in Eq. (3.22). Now the KF can evaluate how "wrong" the previous estimated state $\hat{\mathbf{x}}_{k|k-1}$ is, by calculating the difference between the expected output $\mathbf{H_k}\hat{\mathbf{x}}_{k|k-1}$ and the true measured output $\mathbf{y}_k$ (this difference is called "innovation") [110]. Then, the KF corrects the previously estimated state $\hat{\mathbf{x}}_{k|k-1}$ by adding it with the innovation (scaled by a vector $\mathbf{K}_k$) as:

$$\hat{\mathbf{x}}_k = \hat{\mathbf{x}}_{k|k-1} + \mathbf{K}_k(\mathbf{y}_k - \mathbf{H_k}\hat{\mathbf{x}}_{k|k-1}) \tag{3.25}$$

where the $\hat{\mathbf{x}}_k$ is the corrected estimate for time k (is also called posterior estimate); the scale vector $\mathbf{K}_k$ is called the Kalman Gain and determined by:

$$\mathbf{K}_k = \frac{\mathbf{P}_{k|k-1}\mathbf{H}_k^T}{\mathbf{H}_k\mathbf{P}_{k|k-1}\mathbf{H}_k^T + \mathbf{R}_k} \tag{3.26}$$

Based on its definition, the Kalman gain is the ratio between the uncertainty of the estimate and the uncertainty of the whole system, which determines how the filter wants to "correct" the prior estimate. When the measurement uncertainty is significant and the estimate uncertainty is limited, the Kalman Gain is close to zero. Hence the KF gives more trust to

the estimate and less trust to the measurement. In contrast, when the measurement uncertainty is negligible and the estimate uncertainty is significant, the Kalman Gain is close to one, and the KF gives bigger weight to the measurement [105]. The last step during the correction is to update the state error covariance after the gain $\mathbf{K}_k$ is confirmed:

$$\mathbf{P}_k = (\mathbf{I} - \mathbf{K}_k\mathbf{H}_k)\mathbf{P}_{k|k-1} \tag{3.27}$$

where $\mathbf{I}$ is an identity matrix. The updated $\mathbf{P}_k$ and $\hat{\mathbf{x}}_k$ are both used as input for the next filter iterations.

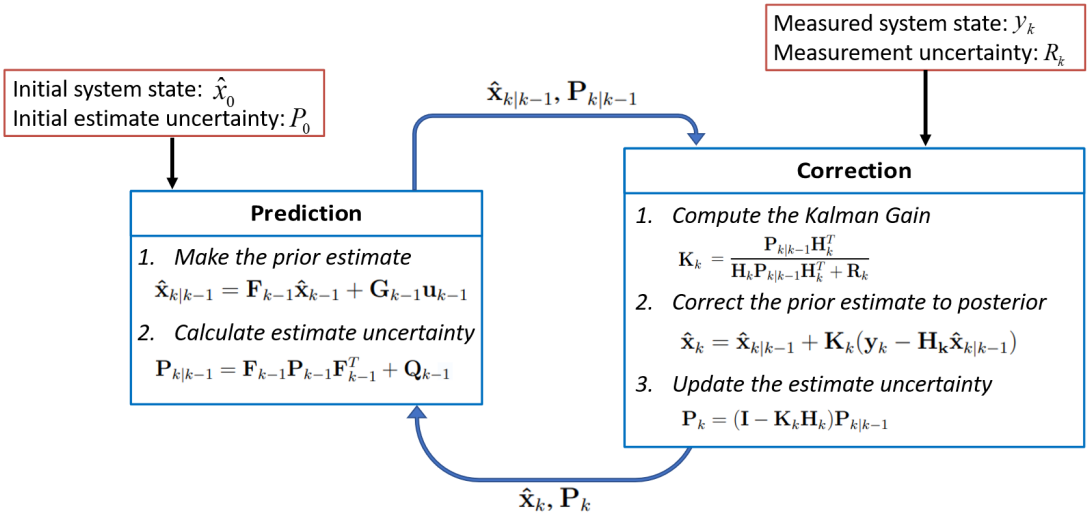

Figure 3.7: Kalman Filter Diagram

To summarize, the KF performs as a "prediction-correction" loop. It is first assumed that the initial state, $\hat{\mathbf{x}}_0$, is known with corresponding uncertainty given by the initial error covariance matrix $\mathbf{P}_0$. Once initialized, the KF predicts the system state based on the system state space model and provides the uncertainty of this prediction. Then, the system performs a measurement. After the KF received the measurement, it compares the measurement uncertainty and the estimate uncertainty, then figures out how to correct the prior estimate (put more weight on the measurement or the estimate, depending on the Kalman Gain). After that, the KF updates the estimate uncertainty of the corrected pos-

terior estimate, then puts the updated uncertainty and corrected estimate as inputs for the next prediction. In principle, the estimate uncertainty is getting smaller with each filter iteration, since $(\mathbf{I}-\mathbf{K}_k\mathbf{H}_k) < 1$, and the designed KF is becoming unbiased when the estimate uncertainty converges to zero. The diagram of the standard KF is provided in Figure 3.7.

3.3.2 Extended Kalman Filter (EKF)

The IMU processing generally requires the estimation of nonlinear quantities, such as the pose, position, and orientation. However, the standard KF applies only to linear systems. In order to use the KF in nonlinear systems, the first approach is the EKF method, which linearizes the nonlinear system, i.e., find a linear system that is approximately equal to the nonlinear system.

Same as the standard KF, the first step in implementing an EKF model is to describe the discrete-time nonlinear system in terms of a state space model and a measurement model:

$$\begin{aligned} \mathbf{x}_k &= f(\mathbf{x}_{k-1}, \mathbf{u}_{k-1}, \mathbf{w}_{k-1}) \\ \mathbf{y}_k &= h(\mathbf{x}_k, \mathbf{v}_k) \end{aligned} \tag{3.28}$$

where $f(\cdot)$ is the vector-valued nonlinear state dynamic function and $h(\cdot)$ is the vector-valued nonlinear output function; $\mathbf{w}$ and $\mathbf{v}$ again represent the process and measurement noise, with covariance Q and R, respectively [112]. The EKF is also consists of two steps: prediction and correction, except the model in Eq. (3.28) should be linearized.

Mathematically, the linearization of a nonlinear function, e.g., $g(x)$, around an operating point a requires a first-order Taylor series expansion [113]:

$$\begin{aligned} g(x) &\approx g(a) + \frac{\partial g(x)}{\partial x}\bigg|_{x=a}(x-a) + \frac{1}{2!}\frac{\partial^2 g(x)}{\partial x^2}\bigg|_{x=a}(x-a)^2 + \cdots \\ &\approx g(a) + T(x-a) \end{aligned} \tag{3.29}$$

where T is the matrix defined by $\frac{\partial g(x)}{\partial x}\ |_{x=a}$ and the higher-order terms are considered

negligible. Therefore, the linerarization of the nonlinear state space function $f(\cdot)$ at time k shoule be the first-order taylor expansion of $f(\cdot)$ around its operating point $\mathbf{x}_k$. Since the term $\mathbf{x}_k$ is an unknown vector to be estimated, the best substitute is the most recent posterior estimate $\hat{\mathbf{x}}_{k-1}$ at time $k-1$ [109]. As a result, the linearized state space model is approximated as:

$$\mathbf{x}_k \approx f_{k-1}(\hat{\mathbf{x}}_{k-1}, \mathbf{u}_{k-1}, 0) + \underbrace{\left.\frac{\partial f_{k-1}}{\partial x_{k-1}}\right|_{\hat{\mathbf{x}}_{k-1},\mathbf{u}_{k-1},0}}_{\mathbf{F}_{k-1}} (\mathbf{x}_{k-1} - \hat{\mathbf{x}}_{k-1}) + \underbrace{\left.\frac{\partial f_{k-1}}{\partial w_{k-1}}\right|_{\hat{\mathbf{x}}_{k-1},\mathbf{u}_{k-1},0}}_{\mathbf{L}_{k-1}} \mathbf{w}_{k-1} \tag{3.30}$$

and the output model is linearized as:

$$\mathbf{y}_k \approx h_k(\hat{\mathbf{x}}_{k|k-1}, 0) + \underbrace{\left.\frac{\partial h_k}{\partial x_k}\right|_{\hat{\mathbf{x}}_{k|k-1},0}}_{\mathbf{H}_k} (\mathbf{x}_k - \hat{\mathbf{x}}_{k|k-1}) + \underbrace{\left.\frac{\partial h_k}{\partial v_k}\right|_{\hat{\mathbf{x}}_{k|k-1},0}}_{\mathbf{M}_k} \mathbf{v}_k \tag{3.31}$$

where the matrices $\mathbf{F}_{k-1}$, $\mathbf{L}_{k-1}$, $\mathbf{H}_k$ and $\mathbf{M}_k$ are called the Jacobian matrices of the system [114]. The matrices $\mathbf{F}_{k-1}$ and $\mathbf{H}_k$ are differentiated with respect to the state estimate, and $\mathbf{L}_{k-1}$ and $\mathbf{M}_k$ are differentiated with respect to the process and measurement uncertainty, respectively [112]. Once the Jacobian matrices have been calculated, the operation of the EKF technique is nearly the same as the linear KF algorithms, with its complete diagram shown in Figure 3.8. The biggest difference is the prior estimate $\hat{\mathbf{x}}_{k|k-1}$ and the measurement innovation $\mathbf{y}_k - \mathbf{h}_k(\hat{x}_{k|k-1}, \mathbf{u}_{k-1}, 0)$ are calculated by propagating the mean of $\hat{\mathbf{x}}_{k-1}$ through the original nonlinear model in Eq. (3.28) rather than the linearized model in Eq. (3.30).

Although the EKF is straightforward and easy to implement, it suffers from the costly calculation of Jacobian matrices [114]. Moreover, an EKF is not suitable for highly nonlinear systems since the covariance is calculated through the first-order linearization of the system model, which may introduce significant errors in the updated posterior error covariance and severely degrade the filter performance [109]. In the following sections, the UKF

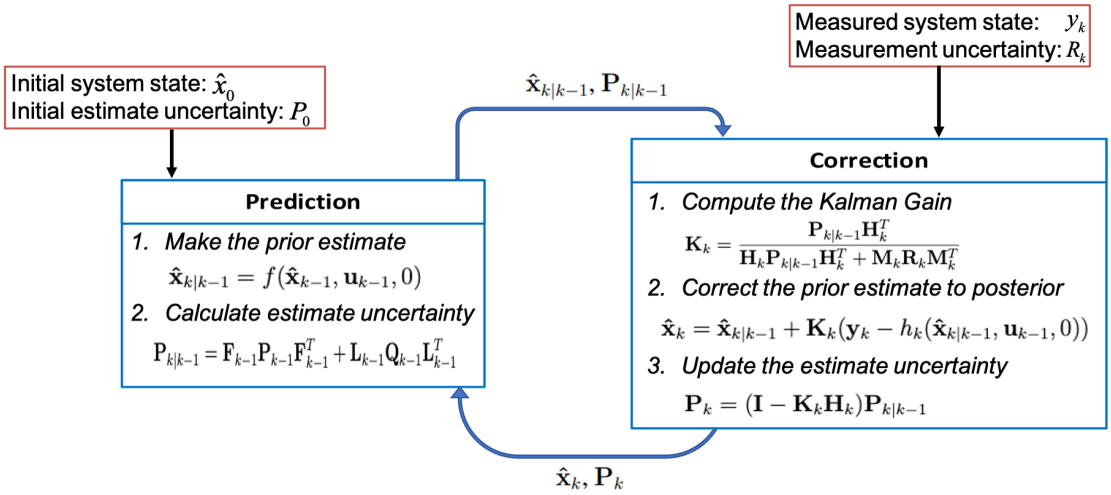

Figure 3.8: Extended Kalman Filter Diagram

is applied to overcome the disadvantages of EKF.

3.3.3 Unscented Kalman Filter (UKF)

The UKF is a common alternative to the EKF, also referred to as the Sigma-Point Kalman Filter (SPKF). The UKF uses an Unscented Transformation (UT) to computes the statistics of a random variable undergoing nonlinear transformation [110]. Instead of linearizing the Jacobean matrices to handle the nonlinearity in the system, the UKF captures the mean and covariance of the state vector $\mathbf{x}_k$ with a minimal set of $2L+1$ chosen sample points (L is the number of states in $\mathbf{x}_k$) [113]. These chosen sample points are called "sigma points," and they are calculated based on a square-root decomposition of the prior mean and covariance. Once produced, these sigma points are propagated through the nonlinear function to find the mean and covariance of the posterior state estimates [114]. The concept of UT and its implementation on UKF are explained in the following two subsections.

Unscented Transformation

Considering propagating a random variable $\mathbf{x}$ with mean $\bar{\mathbf{x}}$ and covariance $\mathbf{P}_x$ through a nonlinear function $g(\mathbf{x})$. The objective of the UT algorithm is to estimate the statistics of

the transformed variable. The intuition behind the UT is straightforward: *it is much easier to approximate a probability distribution than approximate an arbitrary nonlinear function* [108].

The first step is to approximate the variable $\mathbf{x}$ with $2L+1$ weighted sigma points given by:

$$\begin{aligned} \chi_0 &= \bar{\mathbf{x}} \\ \chi_i &= \bar{\mathbf{x}} + (\sqrt{(L+\kappa)\mathbf{P}_x}) \quad i = 1, \cdots, L \\ \chi_{i+L} &= \bar{\mathbf{x}} - (\sqrt{(L+\kappa)\mathbf{P}_x}) \quad i = 1, \cdots, L \end{aligned} \tag{3.32}$$

where the term κ is a scaling parameter to change the higher order moments of the approximation with respect to the distribution of $\mathbf{x}_k$ [110]. When $\mathbf{x}_k$ is assumed gaussian, a suitable argument is to set $L + \kappa = 3$ [115]. To calculate the matrix square root $\sqrt{\mathbf{P}_x}$, a promising method is using the Cholesky Decomposition approach [114]. Let $\mathbf{S} \in \Re^{L \times L}$ satisfy $\mathbf{S}\mathbf{S}^T = \mathbf{P}_x$ and $\mathbf{S}$ is a lower triangular matrix, the $\mathbf{s}_i$ is the ith column of $\mathbf{S}$ for all $i = 1, \cdots, L$. Therefore, the sigma points in Eq. (3.32) transformed to:

$$\begin{aligned} \chi_0 &= \bar{\mathbf{x}} \\ \chi_i &= \bar{\mathbf{x}} + \sqrt{(L+\kappa)}\mathbf{s}_i \quad i = 1, \cdots, L \\ \chi_{i+L} &= \bar{\mathbf{x}} - \sqrt{(L+\kappa)}\mathbf{s}_i \quad i = 1, \cdots, L \end{aligned} \tag{3.33}$$

Once the $2L+1$ sigma points have been generated from the prior statistics as shown above, each point is propagated through the nonlinear function:

$$\mathbf{y}_i = h(\chi_i) \quad i = 0, \cdots, 2L \tag{3.34}$$

and then compute the mean and covariance of the transformed sigma points [116]. Each of

the sigma points gets a specific weight during the calculation, as:

$$\begin{aligned}
\bar{\mathbf{y}} &= \sum_{i=0}^{2L} \omega_i \mathbf{y}_i \\
\mathbf{P}_y &= \sum_{i=0}^{2L} \omega_i (\mathbf{y}_i - \bar{\mathbf{y}})(\mathbf{y}_i - \bar{\mathbf{y}})^T \\
\omega_i &= \begin{cases} \frac{\kappa}{L+\kappa} & i = 0 \\ \frac{1}{2}\frac{\kappa}{L+\kappa} & i = 1, \cdots, 2L \end{cases}
\end{aligned} \tag{3.35}$$

where $\bar{\mathbf{y}}$ is the estimated mean of $\mathbf{y}$ and $\mathbf{P}_y$ is the estimated covariance matrix of $\mathbf{y}$ [115]. These two parameters represent the posterior statistics of $\mathbf{x}$ after the nonlinear transformation.

UKF Implementation

The UKF can be implemented using UT by expanding the nonlinear system to include the noise component. Similar to Eq. (3.28), the first step to design a UKF is to describe the nonlinear system in terms of a state space model and a measurement model:

$$\begin{aligned}
\mathbf{x}_k &= f(\mathbf{x}_{k-1}, \mathbf{u}_{k-1}, \mathbf{w}_{k-1}), x \in \Re^L \\
\mathbf{y}_k &= h(\mathbf{x}_k, \mathbf{v}_k)
\end{aligned} \tag{3.36}$$

where L is the dimension of the state vector. The UKF also operates under the "prediction-correction" pattern. Starting with an assumed initial guess $\hat{\mathbf{x}}_0$ and $\mathbf{P_0}$, the UKF is executed recursively. For the prediction process, the UKF uses the previous posterior state estimate

$\hat{\mathbf{x}}_{k-1}$ and covariance estimate $\mathbf{P_{k-1}}$ to generate the $2L+1$ sigma points as [114]:

$$\begin{aligned} S_{k-1}S_{k-1}^T &= \mathbf{P}_{k-1} \\ \chi_{k-1}^0 &= \hat{\mathbf{x}}_{k-1} \\ \chi_{k-1}^i &= \hat{\mathbf{x}}_{k-1} + \sqrt{(L+\kappa)}col_i(S_{k-1}) \quad i = 1, \cdots, L \\ \chi_{k-1}^{i+L} &= \hat{\mathbf{x}}_{k-1} - \sqrt{(L+\kappa)}col_i(S_{k-1}) \quad i = 1, \cdots, L \\ \chi_{k-1} &= [\chi_{k-1}^0 \qquad \chi_{k-1}^i \qquad \chi_{k-1}^{i+L}] \end{aligned} \tag{3.37}$$

Then, each sigma point in χ_{k-1} is propagated through the nonlinear function, and the transformed sigma points $\chi_{k|k-1}$ are calculated as in:

$$\chi_{k|k-1}^i = f(\chi_{k-1}^i, \mathbf{u}_{k-1}, 0) \quad i = 0, \cdots, 2L \tag{3.38}$$

where the process noise is omitted during the propagation process. The mean and covariance for the propagated sigma points are calculated following the weighting equations in Eq. (3.35). In other words, the predicted mean and covariance for state $\mathbf{x}_k$ is:

$$\begin{aligned} \hat{\mathbf{x}}_{k|k-1} &= \sum_{i=0}^{2L} \omega_i \chi_{k|k-1}^i \\ \mathbf{P}_{k|k-1} &= \mathbf{Q}_{k-1} + \sum_{i=0}^{2L} \omega_i (\chi_{k|k-1}^i - \hat{\mathbf{x}}_{k|k-1})(\chi_{k|k-1}^i - \hat{\mathbf{x}}_{k|k-1})^T \\ \omega_i &= \begin{cases} \frac{\kappa}{L+\kappa} & i = 0 \\ \frac{1}{2}\frac{\kappa}{L+\kappa} & i = 1, \cdots, 2L \end{cases} \end{aligned} \tag{3.39}$$

Now the process noise covariance matrix Q is added to the predicted error covariance matrix $\mathbf{P}_{k|k-1}$ as the additive process noise component [95]. By far, the prediction process is finished, and the system performs measurement at time k and gets the measurement vectors $\mathbf{y}_k$.

To correct the prior state estimate $\hat{\mathbf{x}}_{k|k-1}$ using measurements $\mathbf{y}_k$, the transformed sigma

points are propagated through the output function to predict the measurements:

$$\hat{\mathbf{y}}_k^i = h(\chi_{k|k-1}^i, 0) \quad i = 0, \cdots, 2L \tag{3.40}$$

where the measurement noise is omitted for the prediction. The mean and covariance of these predicted measurements are calculated using:

$$\begin{aligned} \hat{\mathbf{y}}_k &= \sum_{i=0}^{2L} \omega_i \hat{\mathbf{y}}_k^i \\ \mathbf{P}_k^{yy} &= \mathbf{R}_k + \sum_{i=0}^{2L} \omega_i (\hat{\mathbf{y}}_k^i - \hat{\mathbf{y}}_k)(\hat{\mathbf{y}}_k^i - \hat{\mathbf{y}}_k)^T \end{aligned} \tag{3.41}$$

where $\mathbf{R}_k$ is the additive measurement noise assumption. The Kalman Gain K_k in UKF is calculated based on the cross-covariance between the predicted states $\hat{\mathbf{x}}_{k|k-1}$ and the predicted measurements $\hat{\mathbf{y}}_k^i$ as:

$$\begin{aligned} \mathbf{P}_k^{xy} &= \sum_{i=0}^{2L} \omega_i (\chi_{k|k-1}^i - \hat{\mathbf{x}}_{k|k-1})(\hat{\mathbf{y}}_k^i - \hat{\mathbf{y}}_k)^T \\ \mathbf{K}_k &= \mathbf{P}_{\mathbf{k}}^{\mathbf{xy}} (\mathbf{P}_k^{yy})^{-1} \end{aligned} \tag{3.42}$$

The UKF Kalman Gain is then applied to correct the prior state estimates and to update the covariance estimates, as:

$$\begin{aligned} \hat{\mathbf{x}}_k &= \hat{\mathbf{x}}_{k|k-1} + \mathbf{K}_k(\mathbf{y}_k - \hat{\mathbf{y}}_k) \\ \mathbf{P}_k &= \mathbf{P}_{k|k-1} - \mathbf{K}_k \mathbf{P}_k^{yy} \mathbf{K}_k^T \end{aligned} \tag{3.43}$$

where the updated $\mathbf{P}_k$ and the corrected $\hat{\mathbf{x}}_k$ are the posterior vectors for the next UKF iterations. The diagram of the UKF is provided in Figure 3.9.

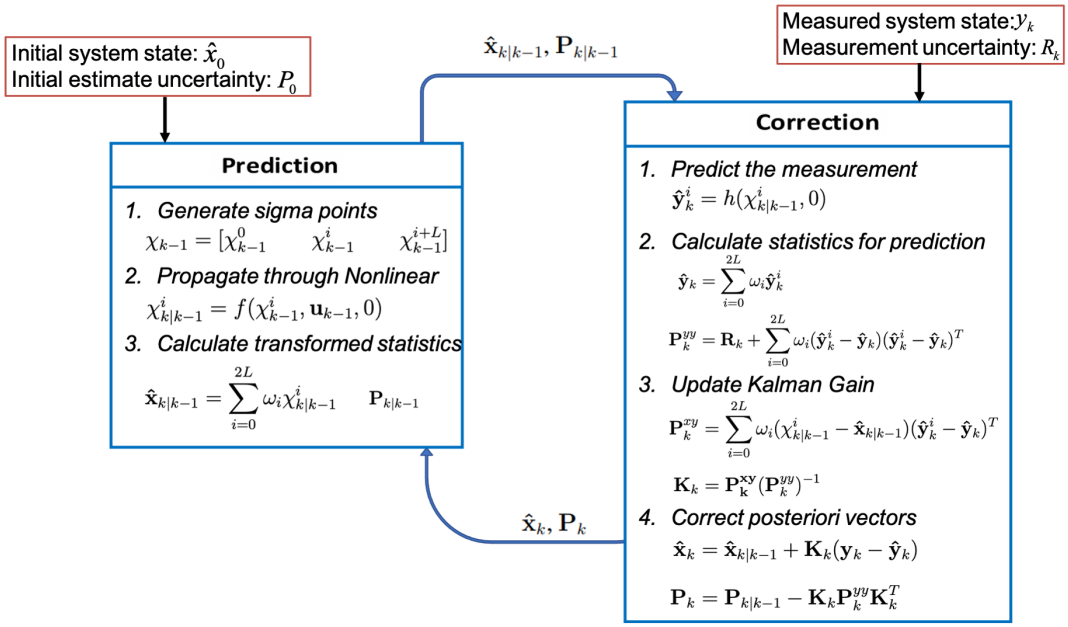

Figure 3.9: Unscented Kalman Filter Diagram

3.3.4 IMU Trajectory Reconstruction with UKF

The trajectory reconstruction in the virtual array system is realized by integrating IMU measurements with an UKF. An IMU is typically composed of gyroscopes and accelerometers, while the gyroscopes measure angular rotation rates and the accelerometers measure linear accelerations [112]. All inertial measurements are measured in the sensor body frame (b-frame), which is a frame rigidly attached to the sensor with its origin at the center of mass of the sensor [115]. For practical navigation and positioning applications, these measurements should be projected onto the local NED (North-East-Down) navigation frame (n-frame), which is a fixed reference frame relative to the ground [115].

By applying the dead-reckoning integration methods through a UKF tool, the position of the mobile receiver is estimated by accumulating the transformed inertial measurements. Note that using an UKF requires knowing the initial orientation of the receiver, as well as the initial velocity of the receiver [80]. In this thesis, these are available through continuous tracking from an initial stand-still position with accelerometers. The origins of the

coordinate system are considered to be the initial position, as only the relative position is required. Besides, a calibration procedure is also required to compensate gyroscope and accelerometer biases, which may result in an unbounded accumulation of errors.

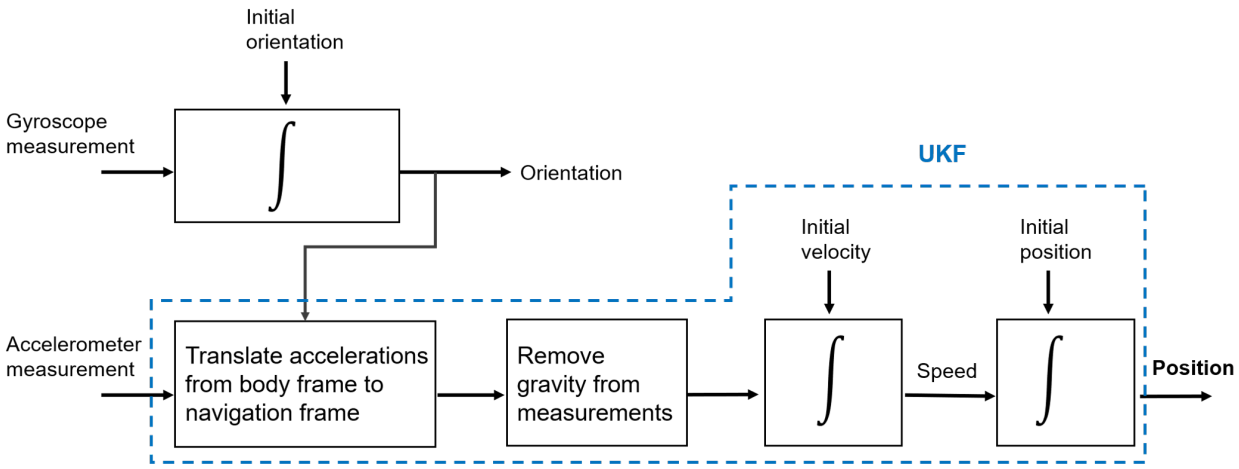

Figure 3.10: The Flow Diagram of the IMU Processing

Therefore, trajectory reconstruction using IMU readings could be considered as a four-step process: 1) calibrate IMU biases before measurement; 2) project measured accelerations and angular rates from the body frame to the navigation frame; 3) estimate the gravity vector and remove it from accelerometer measurements; 4) determine initial orientation and speed of the receiver; 5) trajectory reconstruction by integrating the transformed angular rates and linear acceleration through the UKF. The whole diagram of the UKF with respect to the IMU processing is summarized in Figure 3.10, and each step is explained in more detail following.

IMU Sensor Biases Calibration

The imperfect nature of accelerometers and gyroscopes will introduce biases and noises into their measurements and degrade the performance of UKF [117]. The calibration process aims at finding the bias vector so that true accelerations and angular rates can be found for any movement.

For typical gyroscopes, the measurement model can be defined by:

$$\omega^{\mathbf{b}}(\mathbf{t}) = \omega(\mathbf{t}) + \mathbf{b}_{\mathbf{gyro}}(\mathbf{t}) + \mathbf{n}_{\mathbf{gyro}}(\mathbf{t}) \tag{3.44}$$

where $\omega^{\mathbf{b}}(\mathbf{t})$ is the measured angular rates in body frame, $\omega(\mathbf{t})$ is the true angular rates of the sensor expressed in the sensor frame, $\mathbf{b}_{\mathbf{gyro}}(\mathbf{t})$ is the bias vector, and $\mathbf{n}_{\mathbf{gyro}}(\mathbf{t})$ is the additive measurement noise. The gyroscope bias is temperature-dependent and slowly evolves over time [118]. As the virtual array system only involves motion over short periods of time, the gyroscope bias in this chapter is considered to be a constant. The calibration of gyroscopes is straightforward since when an IMU is standing still, the angular velocity on each axis is zero, so the measured values should be zero. The bias is defined as the average value of raw gyroscope measurement during a standstill.

As for accelerometers, they measure the specific force relative to free-fall, i.e., non-gravitational force per unit mass [119]. Theoretically, the acceleration measured by an IMU during a standstill should be $1g$ (pointing up, as the opposite of gravitational acceleration g). The measurement model for accelerometers have similar noise and bias terms as Eq. (3.44), expressed by:

$$\mathbf{a}^{\mathbf{b}}(\mathbf{t}) = \mathbf{a}(\mathbf{t}) + \mathbf{b}_{\mathbf{acce}}(\mathbf{t}) + \mathbf{n}_{\mathbf{acce}}(\mathbf{t}) \tag{3.45}$$

where $\mathbf{a}^{\mathbf{b}}(\mathbf{t})$ is the acceleration measurements in body frame, $a(t)$ is the true acceleration (with the effect of gravity), $\mathbf{b}_{\mathbf{acce}}(\mathbf{t})$ is the acceleration bias vector and $\mathbf{n}_{\mathbf{acce}}(\mathbf{t})$ is the additive noise vector. To calibrate static biases in accelerometers, a spherical motion fit method is applied by using approaches in [120]. By taking many static measurements with the IMU at different random orientations, as only the gravity vector is present in the accelerometer measurements, the biases can be determined by solving the following set of

equations:

$$\begin{cases} (\mathbf{a}^b_{x_1} - b_x)^2 + (\mathbf{a}^b_{y_1} - b_y)^2 + (\mathbf{a}^b_{z_1} - b_z)^2 = g^2 \\ (\mathbf{a}^b_{x_2} - b_x)^2 + (\mathbf{a}^b_{y_2} - b_y)^2 + (\mathbf{a}^b_{z_2} - b_z)^2 = g^2 \\ \vdots \\ (\mathbf{a}^b_{x_N} - b_x)^2 + (\mathbf{a}^b_{y_N} - b_y)^2 + (\mathbf{a}^b_{z_N} - b_z)^2 = g^2 \end{cases} \tag{3.46}$$

where N is the number of measurements during calibration, $[\mathbf{a}^b_{x_n}, \mathbf{a}^b_{y_n}, \mathbf{a}^b_{z_n}]$ are the accelerometer outputs along IMU body frame at the n-th measurement, and $[b_x, b_y, b_z]$ are the estimated biases. The solution of equations Eq. (3.46) is equivalent to determining the least square error (LSE) centroid and radius of a sphere, as illustrated in Figure 3.11.

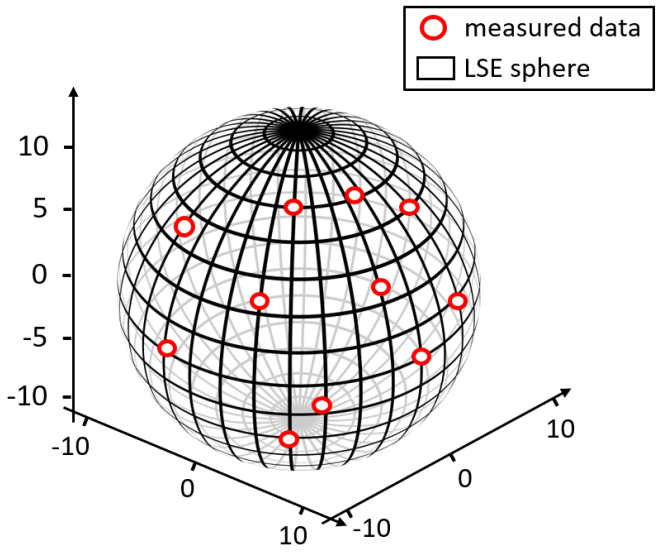

Figure 3.11: Example for IMU Accelerometers Calibration

Frame Transformation

Assuming the calibrated IMU measurements from the triaxial accelerometer and gyroscope are $\left[a^b_x, a^b_y, a^b_z\right]$ and $\left[\omega^b_x, \omega^b_y, \omega^b_z\right]$. The outputs of IMU are in the body frame and should be transferred to the navigation frame. For acceleration measurements, the transformation can be mathematically described by multiplying the rotation matrix C^n_b as:

$$\left[a^n_x, a^n_y, a^n_z\right]^T = C^n_b \cdot \left[a^b_x, a^b_y, a^b_z\right]^T \tag{3.47}$$

where $\left[a_x^b, a_y^b, a_z^b\right]$ are transformed accelerations in the navigation frame [97]. The rotation matrix is defined by the Euler angles ($\boldsymbol{\theta}$, $\boldsymbol{\psi}$, $\boldsymbol{\gamma}$) where $\boldsymbol{\theta}$ represents pitch, $\boldsymbol{\psi}$ represents yaw and $\boldsymbol{\gamma}$ represents roll, expressed by:

$$\mathrm{C}_b^n = \begin{bmatrix} \cos\boldsymbol{\theta}\cos\boldsymbol{\psi} & -\cos\boldsymbol{\gamma}\sin\boldsymbol{\psi} + \sin\boldsymbol{\gamma}\sin\boldsymbol{\theta}\cos\boldsymbol{\psi} & \sin\boldsymbol{\gamma}\sin\boldsymbol{\psi} + \cos\boldsymbol{\gamma}\sin\boldsymbol{\theta}\cos\boldsymbol{\psi} \\ \cos\boldsymbol{\theta}\sin\boldsymbol{\psi} & \cos\boldsymbol{\gamma}\cos\boldsymbol{\psi} + \sin\boldsymbol{\gamma}\sin\boldsymbol{\theta}\sin\boldsymbol{\psi} & -\sin\boldsymbol{\gamma}\cos\boldsymbol{\psi} + \cos\boldsymbol{\gamma}\sin\boldsymbol{\theta}\sin\boldsymbol{\psi} \\ -\sin\boldsymbol{\theta} & \sin\boldsymbol{\gamma}\cos\boldsymbol{\theta} & \cos\boldsymbol{\gamma}\cos\boldsymbol{\theta} \end{bmatrix} \tag{3.48}$$

where the initial value of ($\boldsymbol{\theta}$, $\boldsymbol{\psi}$, $\boldsymbol{\gamma}$) is determined by the initial orientation of the receiver. Sketch map of the transformation between the navigation frame and the body frame is shown in Figure 3.12.

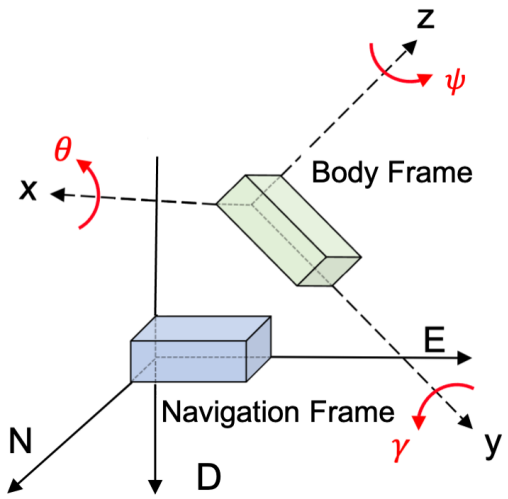

Figure 3.12: The transformation between the navigation frame and the body frame. The navigation frame is fixed and is represented by the North, East, and Down axes. The body frame is aligned with the kinematic axes of the object. The rotation angle around the x, y and z axis is represented by pitch $\boldsymbol{\theta}$, roll $\boldsymbol{\gamma}$ and yaw $\boldsymbol{\psi}$.

Gravity Estimation and Removal

In inertial navigation systems, the raw measurements of the accelerometer usually include components due to gravity, which are not part of the actual receiver accelerations. There-

fore, these gravity components must be manually removed from accelerations in Eq. (3.47). Considering the gravity vector g is constant parallel to the D axis, the compensated accelerations $\left[a_x^{n-}, a_y^{n-}, a_z^{n-}\right]^T$ are calculated by:

$$\left[a_x^{n-}, a_y^{n-}, a_z^{n-}\right]^T = C_b^n \cdot \left[a_x^b, a_y^b, a_z^b\right]^T - [0, 0, g]^T \tag{3.49}$$

After the gravity removal process, the compensated accelerations are processed through the designed UKF and the distance and velocity are then calculated.

Initial Orientation Determination

It is extremely important to accurately estimate the initial orientation of the receiver, as a slight misalignment can integrate into significant trajectory errors. The initial orientation is also used to update the frame transformation matrix in Eq. (3.48). In our proposed virtual array systems, the initial pitch and roll of the IMU are estimated using the technique proposed in [121], which uses observations that during standstill (the accelerometers have measured only the gravitation vector g). The initial state satisfies the following initialization equation:

$$\begin{bmatrix} a_x^b \\ a_y^b \\ a_z^b \end{bmatrix} = \left(\mathrm{C}_b^n\right)^T \begin{bmatrix} 0 \\ 0 \\ g \end{bmatrix} \tag{3.50}$$

By combine Eq. (3.48) and Eq. (3.50), the initial roll $\boldsymbol{\gamma_0^n}$ and pitch $\boldsymbol{\theta_0^n}$ in the navigation frame can be determined by:

$$\begin{cases} \boldsymbol{\gamma_0^n} = \arctan(\frac{a_y^b}{a_z^b}) \\ \boldsymbol{\alpha_0^n} = \arctan(\frac{a_x^b}{\sqrt{\left(a_y^b\right)^2 + \left(a_z^b\right)^2}}) \end{cases} \tag{3.51}$$

The initial yaw cannot be measured using accelerations alone and is manually set to zero in our configuration. Therefore, all yaw expressions are relative to the initial yaw of the

receiver.

UKF Implementation

The trajectory reconstruction formulation considered for this study has states defined by relative positions, relative velocities, and orientations (all in navigation frame). Therefore, the state vector is expressed by:

$$\mathbf{x_k} = \left[\underbrace{P_N, P_E, P_D}_{P_k}, \underbrace{V_N, V_E, V_D}_{V_k}, \boldsymbol{\theta}, \boldsymbol{\psi}, \boldsymbol{\gamma}\right]^T \tag{3.52}$$

and the corresponding state space model is:

$$\mathbf{x}_k = f(\mathbf{x}_{k-1}, \mathbf{u}_{k-1}) \tag{3.53}$$

where $\mathbf{u}_{k-1}$ is the control vector as noisy inputs of the system, defined by:

$$\mathbf{u_k} = \left[\underbrace{(a_x^b)_k, (a_y^b)_k, (a_z^b)_k}_{(a^b)_k}, \underbrace{(\omega_x^b)_k, (\omega_y^b)_k, (\omega_z^b)_k}_{(\omega^b)_k},\right]^T \tag{3.54}$$

For the prediction process, the position is calculated by double integrating the accelerations (after the gravity components removal). The orientation is calculated based on the kinematic relationship, i.e., integrates the angular rates ω^b to derive the relative orientation as IMU begins to move (the rotation of the earth is negligible). The full state equations for

receiver movement can now be expressed as:

$$\begin{aligned}
\dot{P}_k &= V_k \\
\dot{V}_k &= C_b^n \cdot [(a^b)_k] - [0, 0, g]^T \\
\dot{\boldsymbol{\theta}}_k &= (\omega_y^b)_k \cdot cos\boldsymbol{\gamma} - (\omega_z^b)_k \cdot sin\boldsymbol{\gamma} \\
\dot{\boldsymbol{\psi}}_k &= \frac{(\omega_y^b)_k \cdot sin\boldsymbol{\gamma} + (\omega_z^b)_k \cdot cos\boldsymbol{\gamma}}{cos\boldsymbol{\theta}} \\
\dot{\boldsymbol{\gamma}}_k &= (\omega_x^b)_k + ((\omega_y^b)_k \cdot sin\boldsymbol{\gamma} + (\omega_z^b)_k \cdot cos\boldsymbol{\gamma}) tan\boldsymbol{\theta}
\end{aligned} \tag{3.55}$$

where C_b^n is updated by previously estimated orientations. These state equations enable the estimate of the state $\mathbf{x}$ from an initial state $\mathbf{x_0}$ and corresponding sensor measurements a^b and ω^b.

For the correction process, the virtual array system does not implement external sources to get confident observations $\mathbf{y}_k$ to calculate the innovation in Eq. (3.43). In this case, we directly apply the previous predicted state $\hat{\mathbf{x}}_{k|k-1}$ and the previously predicted error covariance matrix $\mathbf{P}_{k|k-1}$ as the updated posterior vectors as:

$$\begin{aligned}
\hat{\mathbf{x}}_k &= \hat{\mathbf{x}}_{k|k-1} \\
\mathbf{P}_k &= \mathbf{P}_{k|k-1}
\end{aligned} \tag{3.56}$$

where the rest of the systems are the same as the standard UKF algorithms.

3.4 The First Proof-of-concept implementation

This section briefly presents the first proof-of-concept implementation of the virtual antenna array system that published in [80]. Figures and results in this section are re-processed based on the original data provided in [80].

3.4.1 Experimental Setup

The proposed architecture is implemented on a software-defined radio (SDR) testbed and tested in an anechoic chamber. Both the transmitter and receiver are equipped with a USRP-N210 SDR and a high-quality OCXO. The transmitter is connected with a horn antenna, and the receiver is connected with a linear antenna. The inertial sensor used in this experiment is a high-accuracy automotive-grade IMU. The receiver antenna and the IMU are attached to the turntable of the anechoic chamber, and the layout of the chamber is shown in Figure 3.13.

The proof-of-concept experimental implementation of the virtual array is shown following: the transmitter sends a periodic 3G PSS sequence every 0.667 ms, and the carrier frequency is set to 1 GHz; the receiver is moved along a semicircular trajectory by using the turntable. The radius of the semicircular trajectory was set to 30, 40, and 50 cm, and 10 measurements were taken for each radius. During each experimental run, the receiver was first standing still for 30 seconds. After the standstill phase, the turntable (also thus the receiver and IMU) rotates 180°, which takes about 5 seconds. The receiver records its received baseband signal packets and the corresponding IMU measurements into a data file for subsequent signal processing. The SNR of the system is around 20 dB.

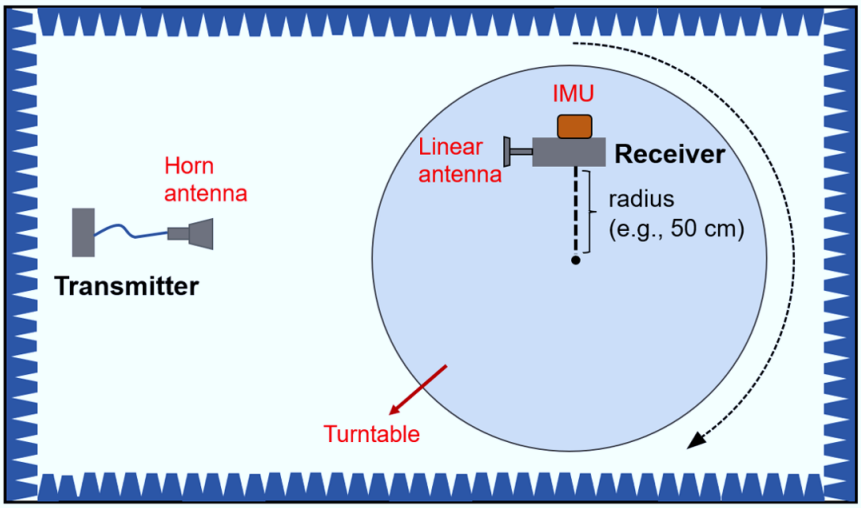

Figure 3.13: Top View of the Experimental Setup in the Anaechoic Chamber

3.4.2 IMU Processing Results

The IMU measurements are transformed to relative positions by using the UKF. The UKF implements the steps illustrated in subsection 3.3.3 and 3.3.4. The initial pitch and roll of the receiver were estimated based on observations during standstill where only the gravitation is measured. The static biases of the accelerometers were estimated before the experiment, and the biases of the gyroscopes were estimated during the standstill phase.

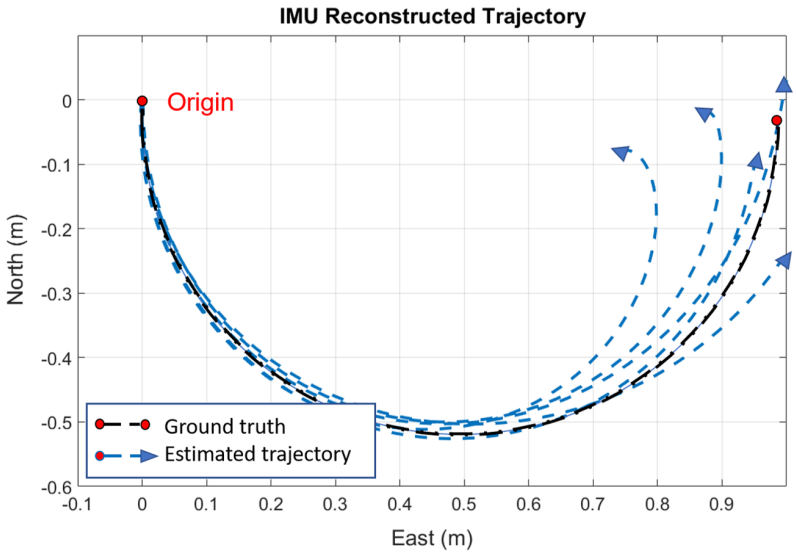

Figure 3.14: Reconstructed Trajectories in Chamber Experiment

Figure 3.14 presents the five trajectories reconstructed using UKF when the radius is set to 50 cm. It is observed that the navigation solution (blue curve) stays close to the ground truth (back curve) at the beginning of the movement but drifts off towards the end of the movement. Similar results were found in other experiments. These drifts are mostly caused by imperfections in the bias calibration or initial orientation determination.

3.4.3 DoA Estimation Results

The two LO frequency offset compensation methods provided in subsection 3.2.2 are implemented in chamber experiments. In this section, we present the DoA estimation results by applying these two methods, respectively.

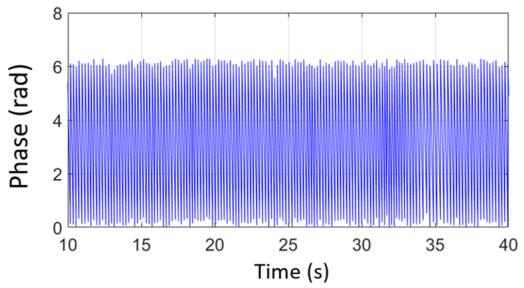

(a) Phase measurements before compensation

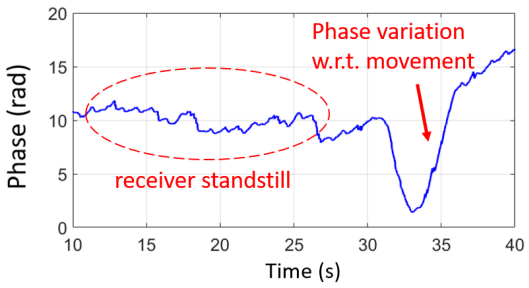

(b) Phase measurements after compensation

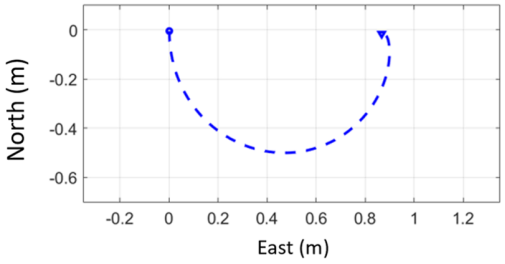

(c) Recontructed trajectory

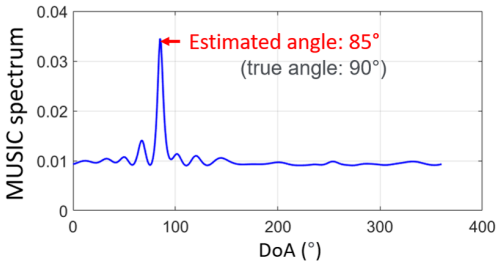

(d) Estimated DoA in MUSIC spectrum

Figure 3.15: Chamber experiment results of the SaS approach [80].

Figure 3.15 presents the results of the SaS approach for one realization of the experiment. The measured raw phase, containing the LO offset distortion, is shown in Figure 3.15a, where the phase shift corresponding to the movement cannot be observed. However, after compensating for the frequency offset, the phase shift due to the movement can clearly be observed, as shown in 3.15b. The phase variations when the receiver standstill (0∼30s) roughly keeps stable and the phase shift due to movement can be observed (30∼35s) after the compensation. The UKF solution for this experiment realization is shown in Figure 3.15c and the MUSIC spectrum is shown in Figure 3.15d. A maximum peak is observed at 85 °, which is close to the true DoA of 90 °.

Figure 3.16 presents the result of the joint estimation approach for one realization of the experiment. In this experiment, the system performs a 2D MUSIC spectrum search (over the LO frequency offset f_0 and the DoA θ) by using the received packets during the movement. A clear peak can be found at 82°, which is close to the true DoA at 90°; the LO frequency offset is simulated simultaneously from the same MUSIC spectrum search.

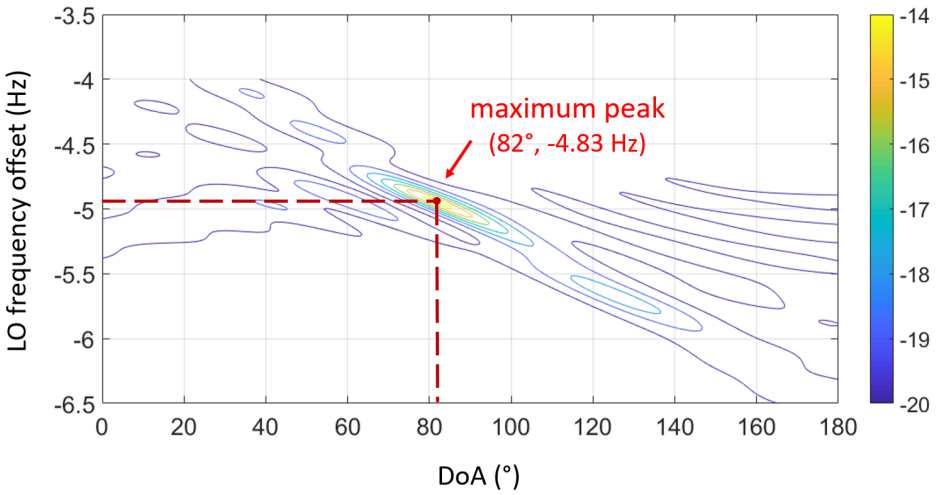

Figure 3.16: Chamber Experiment Results of the Joint Estimation Approach

To summarize, the proof-of-concept implementation and chamber experiments provided in [80] proved the feasibility of the virtual array system. However, this experiment still relies on high-quality OCXO and a high-quality IMU, and the performance of the system when using common, low-quality hardware requires further investigation and experimental verification.

3.5 Conclusion

In this chapter, a novelty DoA estimation method was proposed. Compared with conventional DoA estimation using physical multi-antenna arrays, this method utilized a mobile, single-antenna receiver device to estimate DoA. While the receiver is moving and continuously receiving signals, the DoA can be determined by measuring the intercepted signals at several positions along the receiver's trajectory. The difficulty lies in estimating the relative coordinates of the receiver, and eliminating the phase distortion caused by the imperfect oscillators in both signal source and receiver. The proposed system is implemented and tested in an anechoic chamber by using high-quality IMUs and oscillators. The measurement results proved the feasibility of the virtual array system.

However, the current system remains several main drawbacks: 1) some receiver move-

ments are not able to estimate the DoA, without a theoretical basis to screen feasible trajectories; 2) the virtual array requires precise, relative coordinates of the receiver, which is challenging in reality. In the next chapter, we focus on evaluating and improving the robustness of the virtual array system regarding its drawbacks to account for low-grade IMUs, low-quality LOs, and more flexible trajectories.

CHAPTER 4

OBSERVABILITY ANALYSIS AND EXPERIMENTAL VALIDATION

The previous virtual array system utilized a mobile, single-antenna receiver device to estimate the DoA of an unknown signal source. The system is also implemented and tested in an anechoic chamber which provides satisfying DoA estimation accuracy. However, the system still has two main drawbacks

- The receiver's coordinates are estimated by an embedded inertial measurement unit (IMU), and the accuracy required for trajectory reconstruction is a fraction of the wavelength. Such accuracy is only achievable with high-quality IMUs, as we did in the previous chapter. Thus the feasibility for low-quality IMUs commonly found in commercial mobile devices is questionable.

- The receiver trajectory performed in the chamber is a semicircle, which is challenging to operate without turntables. Discussions in [80] also show that some types of receiver trajectories do not allow to use virtual arrays for DoA estimation, without providing a theoretical basis. Therefore, a theoretical foundation is required to design both feasible and user-friendly trajectories.

In this chapter, we focus on investigating the potential of the virtual array system and improving its robustness by solving the problems above. By studying the observability of the system, we prove that the DoA estimation is not critically dependent on the receiver positions but rather on its acceleration profile. A theoretical basis is also provided for designing effective receiver trajectories. Simulations are conducted to validate these theoretical predictions. The experimental results demonstrate the feasibility of virtual arrays for indoor experiments, with a sufficient number of realistic system uncertainties being taken into account (e.g., LO frequency offsets, IMU errors, manual errors). Note that the

technique in this chapter is assuming a single antenna device, but the approach can also be transferred to multiple-antenna devices. The contributions of this chapter can be summarized as follows:

- An observability analysis is conducted to investigate the potential of the virtual array system and providing the theoretical foundation to determine the set of feasible trajectories.

- The DoA is proven to be observable with naive receiver trajectories, as long as the receiver moves with at least one acceleration. Moreover, if the receiver's initial state and exact position is unknown, the DoA can still be estimated by measuring accelerations only.

- Extensive simulations are conducted by modelling realistic levels of imperfections, to investigate 1) the effect of different measurement functions (to confirm our theoretical predictions), 2) the feasibility to estimate DoA with significant LO phase offsets and multipath.

- The proposed system is implemented and tested on a software-defined radio testbed and serves as the proof of concept. Experiment results in an indoor multipath environment show that good DoA estimation accuracy can be achieved with low-cost off-the-shelf hardware. The complexity and cost of the system are also significantly reduced.

Compared with the conventional virtual array in Chapter 3, the improved system presented in this chapter aims at being feasible with cheap, off-the-shelf hardware (e.g., TCXO), which typically has significant LO frequency offset. The DoA estimation is feasible with user-friendly and simple receiver trajectories without requirements for turntables. Those trajectories can be reconstructed with low-quality IMUs and are thus suitable for portable electronics.

4.1 Concept of Observability

Observability is a notion in control theory that plays a significant role in the field of estimation [122]. A model is observable if it is theoretically possible to infer its internal state by observing its output for an estimation system. The observability serves to determine the existence of relations that bind the state-variables to the inputs, outputs and their time derivatives of a dynamic system, thus uniquely defining them in terms of measurable quantities without the need to know the initial conditions [123]. The observability of linear systems is well defined in [124], and the observability of nonlinear systems is explained in [125]. The concept of locally observable is introduced for the nonlinear system to distinguish two neighbouring states instantaneously. If an estimation system is locally observable, it means that the parameter can be estimated with bounded error.

To investigate the local observability property of the virtual array system, the first mission is to design the system dynamic model, i.e., a set of time-domain formulations that can be utilized to describe the system. In principle, a dynamic model consists of the *input*, the *output*, the *state variable* and the *measurement*. The *input* denotes the external forces affecting the system, which is not enabled here; The *output* is parameters that can be observed directly, e.g., the phase of the received baseband signal ϕ; The *state variable* is the set of variables used to describe the change of the system, e.g., positions of the receiver array elements; The *measurement* refers to the variables among state vectors that can be measured with instruments and is usually used to update system parameters, e.g., the acceleration measured by IMU. The second step is to define the state variable model, which comprises first-order ordinary differential equations (ODEs) that describe time derivatives of the state variables [93]. The number of state variables represents the order of the system. Then, the local observability and so-called observability matrix can be determined by the rank criteria described in [126], i.e. the system is locally observable if its observability matrix is **full column rank**. One thing to note is, in principle, the observability of a system

is irrelevant to the measurement noise. Therefore, the state variable model in observability analysis is usually derived under the noise-free model.

In localization systems with mobile transceivers, some papers showed that the transceivers movements (velocity, acceleration, etc.) impact the observability and, thus, the estimation performance [127, 128, 129]. In some cases, the proper trajectory choice can even change the system from unobservable to observable. Since linear arrays are widely applied in ground direction finding systems, we discuss the case when the receiver moves along a linear trajectory along the x-axis with a constant acceleration and a constant heading, which is easy and naive to perform for most moving objects. Extensions to linear trajectories that are not parallel to the x-axis can be derived by performing a reference frame rotation. In this paper, the objective of observability analysis is twofold: 1) determine whether the localization system is locally observable for different receiver trajectories, especially in the case where the receiver cannot stands still, and the LO frequency offset cannot be estimated separately; and 2) when the system is not observable, determine the observable states if any. Note that the observability theory can also be applied to nonlinear trajectories.

4.2 Observability Analysis Implementation

4.2.1 System dynamic model

Let $r_x(t)$, $v_x(t)$ and $a(t)$ denote the relative position, velocity and acceleration of the receiver along the x axis at time t, as the first three state variables. Then, we can write:

$$\begin{aligned} r_x(t) &= r_x(t_0) + (t - t_0)\, v_x(t_0) + \tfrac{1}{2}(t - t_0)^2 a(t_0) \\ v_x(t) &= v_x(t_0) + (t - t_0)\, a(t_0) \end{aligned} \tag{4.1}$$

where $r_x(t_0)$ and $v_x(t_0)$ denote the initial position and initial velocity vector at initial timestamp t_0. According to (3.14), if the transmitter broadcasts a periodic signal with

period T_0, the phase of the received packets at time $t + T_0$ can be expressed as follows:

$$\psi\left(t + T_0\right) = \psi\left(t\right) + \omega\left(t\right) T_0 + \frac{2\pi}{\lambda} \cdot \cos\left[\theta\left(t\right)\right] \cdot \Delta r_x \tag{4.2}$$

with

$$\Delta r_x = v_x(t) \cdot T_0 + \frac{1}{2} \cdot a(t) \cdot T_0^2 \tag{4.3}$$

being the displacement when the receiver moves from position $r_x(t)$ at time t to position $r_x(t + T_0)$ at time $t + T_0$; $\omega\left(t\right) = 2\pi f_0$ remains constant and it denotes the angular LO frequency offset caused by the frequency mismatch f_0; $\psi\left(t\right)$ here denotes the overall phase offset, including the phase shift due to movement and the time-accumulated phase offset due to $\omega\left(t\right)$. By doing this, the state θ is introduced for tracking the DoA along the trajectory and the state ω is introduced for recording the LO phase offset.

Now we have full state variables to describe the virtual array system. The 6-element state vector $\mathbf{x}$, composed of the observed phase ϕ, the angular velocity for LO phase offset ω, the DoA of the arrived signal θ, the relative position r_x, the relative velocity v_x and the constant acceleration a, given as:

$$\mathbf{x} = \left[\psi, \omega, \theta, r_x, v_x, a\right]^T \tag{4.4}$$

Based on (4.1)-(4.3), we have a complete description of $\mathbf{x}$, and they are referred to as the full dynamical model of the system. The state variable model, consisting of the first-order

differential equations for the vectors in $\mathbf{x}$, is therefore defined as:

$$\begin{cases} \dot{\psi}(t) & = \omega(t) + \frac{2\pi}{\lambda}\cos\left[\theta\left(t\right)\right] \cdot v_x(t) & \triangleq \dot{\mathbf{x}}_1 \\ \dot{\omega}(t) & = 0 & \triangleq \dot{\mathbf{x}}_2 \\ \dot{\cos}\left[\theta\left(t\right)\right] & = 0 & \triangleq \dot{\mathbf{x}}_3 \\ \dot{r_x}(t) & = v_x(t) & \triangleq \dot{\mathbf{x}}_4 \\ \dot{v_x}(t) & = a(t) & \triangleq \dot{\mathbf{x}}_5 \\ \dot{a}(t) & = 0 & \triangleq \dot{\mathbf{x}}_6 \end{cases} \tag{4.5}$$

From a control theory perspective, the objective of the virtual array is to estimate the DoA state θ by observing the received phase while updating the measurements. The measurement function, besides the phase vector ψ, can be chosen among the relative position-related vectors $r_x\left(t\right)$, $v_x\left(t\right)$ and $a(t)$, depending on the available instrument. The phase vector ψ can be measured by correlating the received baseband samples with the known preamble sequence; Precise measurement of the $r_x\left(t\right)$ requires a high-quality IMU with a known initial velocity, which is difficult to achieve with common sensors, or cannot be obtained with sufficient accuracy. Measurement of the linear acceleration $a(t)$, however, is often available with low-cost IMUs that common in commercial electronics.

Therefore, in the following sections, we will discuss these two situations: 1) we include $r_x(t)$ as the measurement; 2) we include $a(t)$ as the measurement. The first case corresponds to scenarios where location information can be measured in the system. For example, the system applies a high-accuracy GPS unit or uses other high-accuracy localization methods (e.g., the ultra-wideband localization). The second case corresponds to scenarios where only IMU data is available.

4.2.2 Measuring the receiver position

We first consider that we can measure the position vector $r_x(t)$ and the observed phase $\psi(t)$, so the measurement function can be written as follows:

$$\begin{cases} h_1(x) &= \psi(t) &= \mathbf{x}_1 \\ h_2(x) &= r_x(t) &= \mathbf{x}_4 \end{cases} \tag{4.6}$$

and the continuous-time nonlinear dynamic systems usually have the general form written as:

$$\sum\nolimits_{NL} : \begin{cases} \dot{x}(t) = f[x(t)] \\ y(t) = h[x(t)] \end{cases} \tag{4.7}$$

where $y \in \mathbb{R}^{\mathrm{m}}$ is the output, f is the analytic vector function and h is the output measurement equation. For nonlinear systems, unlike for linear time-invariant systems, the derivatives of the output cannot be expressed in terms of the arrays [124]. To this end, it is necessary to construct the observability matrix by using the Lie derivatives in [130]. Based on (4.5), we first rewrite the vector-valued function f_i:

$$\begin{cases} f_1(x) = \mathbf{x}_2 + \alpha \mathbf{x}_3 \mathbf{x}_5 \\ f_2(x) = 0 \\ f_3(x) = 0 \\ f_4(x) = \mathbf{x}_5 \\ f_5(x) = \mathbf{x}_6 \\ f_6(x) = 0 \end{cases} \tag{4.8}$$

where $\alpha = \frac{2\pi}{\lambda}$. By definition, the zero-order Lie derivative of the scalar measurement h is the function itself, i.e.:

$$\begin{cases} \pounds_f^0 h_1(x) = h_1(x) = \mathbf{x}_1 \\ \pounds_f^0 h_2(x) = h_2(x) = \mathbf{x}_4 \end{cases} \tag{4.9}$$

The first-order Lie derivative of the measurement function with respect to f_i is defined as:

$$\begin{cases} \pounds_f^1 h_1(x) = \sum_{i=1}^{n=5} \frac{\partial h_1(x)}{\partial \mathbf{x}_i} \cdot f_i(x) = \mathbf{x}_2 + \alpha \mathbf{x}_3 \mathbf{x}_5 \\ \pounds_f^1 h_2(x) = \sum_{i=1}^{n=5} \frac{\partial h_2(x)}{\partial \mathbf{x}_i} \cdot f_i(x) = \mathbf{x}_5 \end{cases} \tag{4.10}$$

where similar calculations hold for higher-order derivatives along with the vector fields. For our model, which has six states, the higher-order Lie derivatives starting from the third derivative are entirely zero vectors.

Given above preliminaries, the vector G can be constructed with the Lie derivatives up to the M-1 order (where M equals to the number of states):

$$G \triangleq \begin{bmatrix} \mathbf{x}_1 \\ \mathbf{x}_4 \\ \mathbf{x}_2 + \alpha \mathbf{x}_3 \mathbf{x}_5 \\ \mathbf{x}_5 \\ \alpha \mathbf{x}_3 \mathbf{x}_6 \\ \mathbf{x}_6 \\ \mathbf{0}_{6\times 1} \end{bmatrix} \tag{4.11}$$

The observability matrix $\mathcal{O}$ is defined from the observability Lie algebra by taking the gradient of G (w.r.t. $\mathbf{x}_1, ..., \mathbf{x}_M$) as:

$$\mathcal{O}_{NL_1} = \begin{bmatrix} 1 & 0 & 0 & 0 & 0 & 0 \\ 0 & 0 & 0 & 1 & 0 & 0 \\ 0 & 1 & \alpha \mathbf{x}_5 & 0 & \alpha \mathbf{x}_3 & 0 \\ 0 & 0 & 0 & 0 & 1 & 0 \\ 0 & 0 & \alpha \mathbf{x}_6 & 0 & 0 & \alpha \mathbf{x}_3 \\ 0 & 0 & 0 & 0 & 0 & 1 \\ & & & \mathrm{O}_{6\times 6} & & \end{bmatrix} \tag{4.12}$$

If $\mathcal{O}_{NL_1}$ is full column rank, then the system is said to satisfy the observability rank condition, which means the system is locally observable. In this case, it is obvious that rank($\mathcal{O}_{NL_1}$) = rank($\mathcal{O}_{NL_1}[1:6;1:6]$), where $\mathcal{O}_{NL_1}[1:6;1:6]$ represents the first 6×6 sub-matrix of $\mathcal{O}_{NL_1}$. Matrix $\mathcal{O}_{NL_1}[1:6;1:6]$ is full-rank when it's determinant is not equal to zero. The determinant of $\mathcal{O}_{NL_1}[1:6;1:6]$ is given by

$$\det(\mathcal{O}_{NL_1}[1:6;1:6]) = -a\mathbf{x}_6 \tag{4.13}$$

Therefore, as long as the acceleration of the system is not zero, $\mathcal{O}_{NL_1}$ has a rank of 6, and the system is locally observable. This finding agrees with our intuition of a virtual antenna array: when the receiver has constant linear velocity, the phase difference in (4.2) does not allow to separate the phase drift caused by the LO offset from the phase shift due to receiver movement. For the system to be observable, the acceleration can be both constant or time-varying, and the direction of acceleration does not have to be parallel to the heading of the receiver. Linear trajectories with non-zero acceleration and any non-linear trajectories caused by unparalleled acceleration all satisfy this requirement.

4.2.3 Measuring the receiver's acceleration

In this case, we will discuss the situation where the position vector $r_x(t)$ cannot be measured and the acceleration measurement is available. Therefore, the measurement function in (4.6) changes to:

$$\begin{cases} h_1(x) & = \phi(t) & = \mathbf{x}_1 \\ h_2(x) & = a_x(t) & = \mathbf{x}_6 \end{cases} \tag{4.14}$$

Following a similar approach, we can easily determine all block elements of observability matrix $\mathcal{O}_{NL_2}$ as:

$$\mathcal{O}_{NL_2} = \begin{bmatrix} 1 & 0 & 0 & 0 & 0 & 0 \\ 0 & 0 & 0 & 0 & 0 & 1 \\ 0 & 1 & \alpha\mathbf{x}_5 & 0 & \alpha\mathbf{x}_3 & 0 \\ 0 & 0 & 0 & 0 & 0 & 0 \\ 0 & 0 & \alpha\mathbf{x}_6 & 0 & 0 & \alpha\mathbf{x}_3 \\ 0 & 0 & 0 & 0 & 0 & 0 \\ & & & \mathrm{O}_{6\times 6} & & \end{bmatrix} \tag{4.15}$$

Obviously, the matrix $\mathcal{O}_{NL_2}$ has rank four and is not full column rank, thus the affine control system with measurement function (4.14) is not locally observable.

While the notion of local observability is a binary property, i.e., it specifies whether the system is observable or not, the question of which state is not unobservable is still of considerable importance. As long as the unobservable state is not the target parameter, i.e., the θ in our case, the system under the current configuration is still functional. In the next section, we develop a methodology for determining the unobservable direction of nonlinear systems by applying the concept of the unobservable space (also called null space) [117, 131].

4.2.4 Finding the unobservable states

When the observability matrix $\mathcal{O}$ is rank deficient, the deficiency is equal to the dimension of its unobservable space $\mathcal{NO}$. In our case, the observability matrix $\mathcal{O}_{NL_2}$ has column rank $n_0 = 4$ and column dimension $n = 6$, so the rank deficiency is $n - n_0 = 2$, as well as the dimension of $\mathcal{NO}$. This result indicates that there are only two vectors satisfying $\mathcal{O}_{NL_2} \cdot q = 0$, where q consists of the basis of $\mathcal{NO}$. We then design a $n \times n$ transformation matrix as:

$$Q_{n\times n} = \begin{bmatrix} q_1 & \dots & q_{n-n_0} & p_{n-n_0+1} & p_n \end{bmatrix} \tag{4.16}$$

where $\{q_i, i = 1, \ldots, n - n_0\}$ are linearly independent vectors in the unobservable space of the observability matrix $\mathcal{O}_{NL_2}$ and $\{p_j, j = n - n_0 + 1, \ldots, n\}$ are arbitrary vectors to keep matrix $Q_{n\times n}$ invertible. The vectors q_i form a basis set of the unobservable subspace of the system. The remaining columns p_j form a basis set of the observable subspace. The transformation matrix allows us to separate the observable subspace from the unobservable subspace and indicate which state is not locally observable as detailed below:

$$\mathcal{O}_{NL_2} \cdot \mathcal{NO} = 0 \tag{4.17}$$

thus, the calculation of q_i is following:

$$[q_1, q_2] = \begin{bmatrix} 0 & -\alpha\mathbf{x}3 & 0 & 0 & 1 & 0 \\ 0 & 0 & 0 & 1 & 0 & 0 \end{bmatrix}^T \tag{4.18}$$

hence the basis vector indicates that $\mathbf{x_1}$, $\mathbf{x_3}$ and $\mathbf{x_6}$ (corresponding to ψ, θ and a) lie within the observable subspace, while $\mathbf{x_2}$, $\mathbf{x_4}$ and $\mathbf{x_5}$ (corresponding to ω, v_x and r_x) span the non-observable subspace. This result indicates that even without the knowledge of initial velocity and the exact position of receiver, we can still extract DoA from the observed phase of the virtual array by measuring the acceleration a only.

The intuition behind this conclusion is the following: DoA is estimated by analysing the phase shift caused by the receiver displacement. Since the displacement in (4.3) is related to the initial velocity v_x and acceleration a, the phase shifts contributed by the initial velocity v_x in (4.2) will be grouped with the LO phase offset $2\pi f_0 T_0$. In other words, combining (4.2) and (4.3), the observed phase of the received signal is:

$$\begin{aligned} \psi\left(t + T_0\right) &= \psi\left(t\right) + 2\pi f_0 T_0 + \frac{2\pi}{\lambda} \cdot \cos\left[\theta\left(t\right)\right] \cdot \Delta r_x \\ &= \psi\left(t\right) + 2\pi \left(f_0 + \frac{\cos\left[\theta\left(t\right)\right]}{\lambda} \cdot v_x \right) T_0 \\ &\quad + \left(\frac{2\pi}{\lambda} \cos\left[\theta\left(t\right)\right] \cdot \frac{a^2}{2} \right) \cdot T_0^2 \end{aligned} \tag{4.19}$$

thus it will be impossible to distinguish v_x from f_0 by measuring a only. However, the last term in (4.19) can still be distinguished as the only quadratic function of T_0, where the DoA θ is the only unknown variable in this term. A joint estimation of DoA and LO frequency offset (as proposed in Chapter 3) will provide the correct DoA, but a fake frequency offset $\acute{f_0}$ (it is barely the sum of f_0 and v_x, i.e. $\acute{f_0} = f_0 + \frac{\cos[\theta(t)]}{\lambda} \cdot v_x$). We verify this theoretical prediction with simulations in Section 4.3 and measurements in Section 4.4, and it could serve as guidelines for trajectory design problems in virtual array systems.

The observability analysis results above can provide two guidelines about the trajectory design in the virtual array, as shown below. Verification of these guidelines are performed with simulations and present in the next section:

1. If the receiver moves with a constant linear velocity, the DoA can only be estimated with the SAS approach. To estimate the DoA with the joint estimation method, the receiver has to have at least one acceleration to make the system observable. Linear trajectories with non-zero acceleration and any non-linear trajectories caused by unparalleled acceleration all satisfy this requirement.

2. In a virtual array system, when the receiver moves with a constant acceleration, even when perfect position information is not available, or we do not know the initial velocity, the DoA can still be estimated as long as we can measure the acceleration of the receiver.

4.3 Validation of Observability-deduced Principles Through Simulation

In this section, we perform simulations to verify the feasibility of the virtual array. We conducted Monte-Carlo simulations to evaluate the DoA estimation performance of the virtual array system under simple linear trajectories with/without knowledge of receiver position and initial velocity. Specifically, we calculated the root mean square error (RMSE) for 5000 trials as a criterion to evaluate the DoA estimation performance. The simulation

configuration also considered real-world system imperfections (e.g., multipath, low-quality LO).

4.3.1 Simulation setup

Simulation of the proposed system is conducted in Matlab. To design the virtual array, we simulate a linear receiver movement with a constant acceleration of 0.95 m/s^2. The initial velocity is set to zero. The receiver's movement lasts for 0.8 seconds, so the length of the linear trajectory is 0.3 m. We consider that the relative positions of the receiver can be calculated from IMU readings and the IMU readings are unbiased. Thus, we have perfect knowledge of the receiver's positions and accelerations. The carrier frequency is set to 1 GHz, and the number of virtual arrays is set to 10. Hence, the array spacing is 0.03 m, which meets the requirement of less than half of the wavelength (0.15 m).

We consider the transmitter is sending periodic packets, i.e., a PSS sequence, every 0.667 ms. The receiver captures the signal and performs correlation between the received baseband signal and the known preamble. The principle of the simulation is to model the received phase and estimate the corresponding DoA. The direct path always exists between the transmitter and the receiver, and the DoA θ of the LoS path is set to a random angle between 0° and 180°. Although the system model in Chapter 3 only considered the LoS propagation, the array measurements in real-world propagation are likely to be corrupted by the multipath component [132]. Therefore, to include the possible multipath distortion, a Rician propagation model is applied to describe the channel condition: in addition to the LoS path, there are a number of multipath paths that arrive at the receiver at different angles. In this case, the channel amplitude is described by the simulated Rician channel impulse response (CIR). The CIR is expressed as follows:

$$h\big[n,m\big] = e^{j\vec{\beta}\cdot\vec{r}[n]} + \sum_{k=1}^{N_{mpc}} \alpha_k e^{j\left(\psi_k + \vec{\beta_k}\cdot\vec{r}[n]\right)} \tag{4.20}$$

where the LoS component is assumed to have a unit amplitude; α_k is the relative amplitude of the k-th multipath component, distributed uniformly over $[0, \alpha_{max}]$; N_{mpc} is the number of multipath path and set to 10 in the simulations; ϕ_k is a random phase term distributed uniformly over $[0, 2\pi]$ and $\vec{\beta_k}$ is the wave vector of the k-th multipath component (corresponding to an incident angle that is distributed uniformly over [0, 2π]). This corresponds to the worst case, showing that the multipath comes from all directions. Also, the total multipath power is set within 10 dB lower of the LoS power. The received signal is considered to contain a zero-mean, additive white-noise with a signal-to-noise ratio (SNR) of 30 dB.

As the propagation scenario is fully characterized, the next step is to simulate the LO phase offset due to the transceiver frequency mismatch f_0 and also the fluctuation of f_0 itself. In principle, the value of f_0 varies continuously with time, and the lower the quality of the oscillator, the more drastic the variation will be. To simulate the received signal distorted by the LO phase shift, we use a discrete two-state state-space model to simulate f_0 between the transmitter and the receiver [133, 134]. The dynamic of the LO is described as $x_k = [\psi_k, \omega_k]^T$, where ψ_k is the LO frequency offset and ω_k is the accumulated angular frequency offset at the time-slot k. The LO offsets of each transmit node relative to the receiver can be modelled as:

$$x_k = F x_{k-1} + n_k\left(Q\right) \tag{4.21}$$

where the state update matrix F is defined as

$$F = \begin{bmatrix} 1 & T_0 \\ 0 & 1 \end{bmatrix} \tag{4.22}$$

and $n_k\left(Q\right)$ is the noise vector that causes the LO phase and frequency drifts from their

nominal value, which is defined as:

$$Q = q_1^2 \begin{bmatrix} T_0 & 0 \\ 0 & 0 \end{bmatrix} + q_2^2 \begin{bmatrix} \frac{T_0^2}{3} & \frac{T_0^2}{2} \\ \frac{T_0^2}{2} & T_0 \end{bmatrix} \tag{4.23}$$

where q_1^2 and q_2^2 are the process noise parameters that correspond to white frequency noise and random walk frequency noise, respectively [134, 94]. For the DoA estimation with virtual array in our simulations and experimental setups, transceivers are generally equipped with low-cost oscillators which contain significant LO phase drift, i.e. TCXO, typical values are $q_1^2 = 8.47 \times 10^{-22}$ and $q_2^2 = 5.51 \times 10^{-18}$.

Finally, the received signal with LO phase drift and channel distortion is calculated and the DoA can be simulated after the effect of LO frequency mismatch is eliminated. The first method is the SAS approach, where the LO phase offset is measured externally. In simulations, we use the average value of f_0 0.8 s before the receiver movement to compensate for the phase shift during the movement; the DoA estimation results are presented. The second method is the joint estimation approach, which separates the phase offset due to LO and the phase shift due to the receiver movement in a 2D MUSIC spectrum search. The feasibility of the joint estimation approach under different measurement information is presented in the next section.

4.3.2 Verification of the observability analysis

One of the objectives of our simulations is to validate the two predictions provided by the observability analysis in Section 4.2.4. The first prediction can be proved easily with simulations. We simulate the condition when the receiver performs a uniform linear motion, and the corresponding MUSIC spectrum is presented in Figure 4.1. Since the phase shift due to receiver movement cannot be separated from the phase shift due to LO offset, the MUSIC algorithm failed to calculate the right noise eigenvalues and reconstruct the corresponding noise subspace. As shown in the figure, the MUSIC spectrum is a diagonal line between

the frequency and angular domains and is also symmetric about 90° due to the DoA ambiguity in uniform linear arrays. Therefore, it does not yield any peaks and leads to incorrect DoA estimates. As a result, if the receiver can only move with a constant linear velocity, the DoA in the virtual array can only be estimated with the SAS approach, as the estimated term f_0 can be considered an extra input into the system.

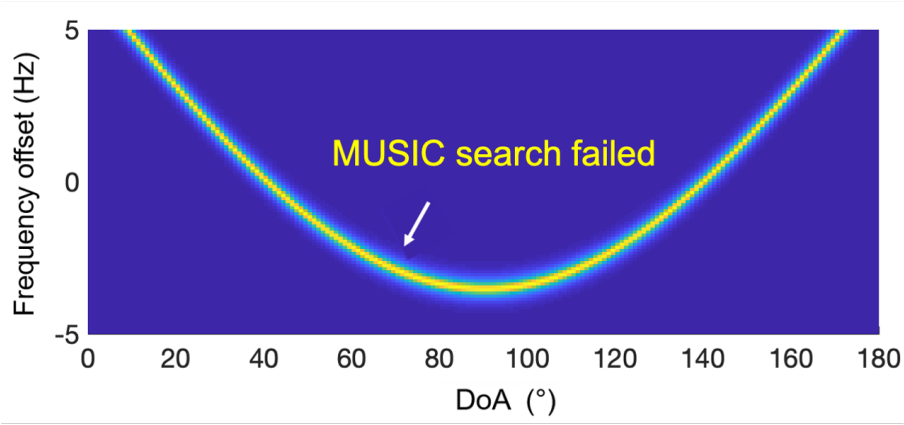

Figure 4.1: MUSIC Spectrum with Uniform Linear Movement

The second prediction is focused on the type of measurement function, i.e., the system is observable when taking position measurements and unobservable when taking acceleration measurements. However, the DoA is observable in both cases. Here we take one realization with $[\theta, f_0] = [45°, 12.2\ Hz]$, generated in our simulation, as an example. When taking the position vector as a measurement function, the steering vector is calculated with unbiased receiver coordinates. The MUSIC spectrum in Figure 4.2a is calculated under this configuration, and the highest main peak indicates the estimated θ and f_0.

When taking accelerations as measurement, the joint approach still needs receiver coordinates to calculate the steering vector. Since the true initial velocity is unknown, we will give a random initial velocity and combine it with the true acceleration value obtained from IMU measurements to create a *"fake"* receiver trajectory. This trajectory deviates from the real position of the receiver. However, it can be applied in the signal model of (4.19) to separate the phase shift caused by the receiver movement as long as the WSSUS assumption and spatial aliasing criterion are still satisfied.

In this case, we assume the initial velocity for the fake trajectory is 0.5 m/s instead of zero (its true initial velocity). With the *"fake"* relative receiver coordinates, the 2D MUSIC search result with this virtual trajectory is shown in Figure 4.2b. It can be seen that the peak of the spectrum still tracked the roughly correct DoA around $46°$, where the estimated LO offset is wrong (0.9 Hz drifts from the correct LO offset). This result verifies our predictions in Section 4.2.4, which states that the DoA is observable when the receiver's acceleration parameters are measured, even though the observability matrix is rank deficient. The estimated LO offset is wrong due to the term f_0, which lies in an unobservable direction.

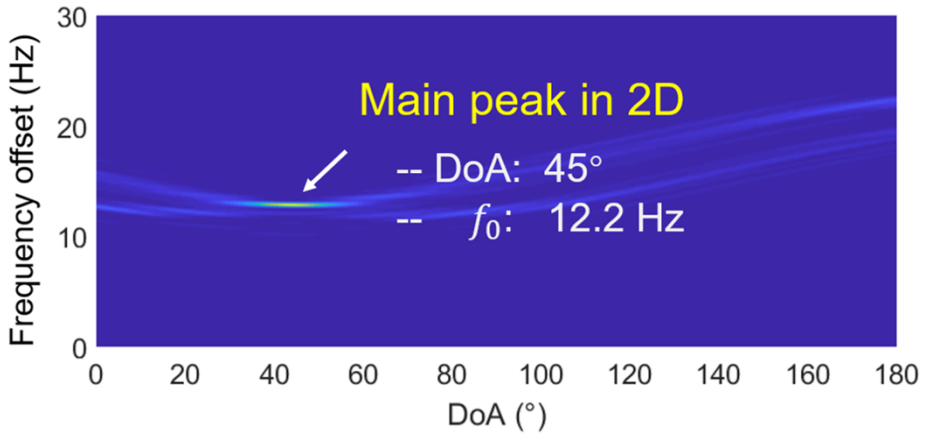

(a) Joint estimation with knowledge of receiver position

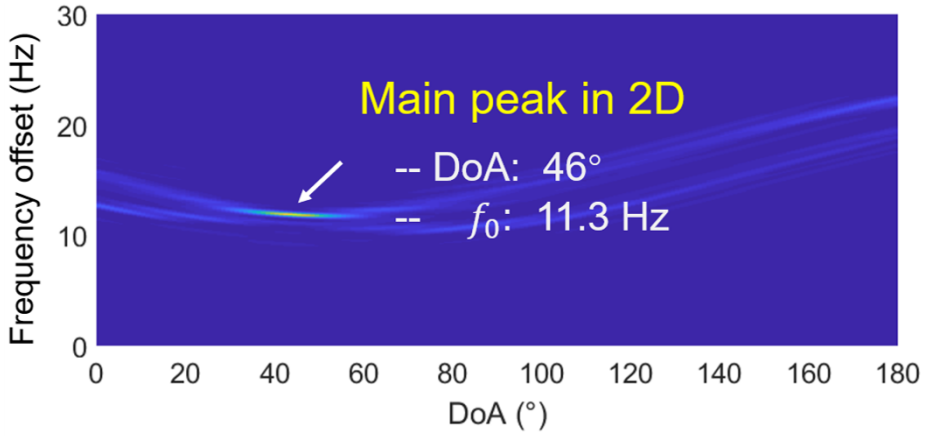

(b) Joint estimation with knowledge of acceleration

Figure 4.2: Simulation for the Joint estimation with different measurement [91].

4.3.3 Verification of the spatial aliasing criterion

Another subject of the simulations in this chapter is to verify the spatial aliasing criterion in the virtual array system. As explained in Section 3.2.4, the distance between the two adjacent array elements must be no larger than $\lambda/2$ to avoid DoA ambiguity, which leads to significant velocity constraints for the receiver. To verify this statement, we perform simulations by observing the corresponding MUSIC spectrum under different element spacing configurations. The results are shown in Figure 4.3.

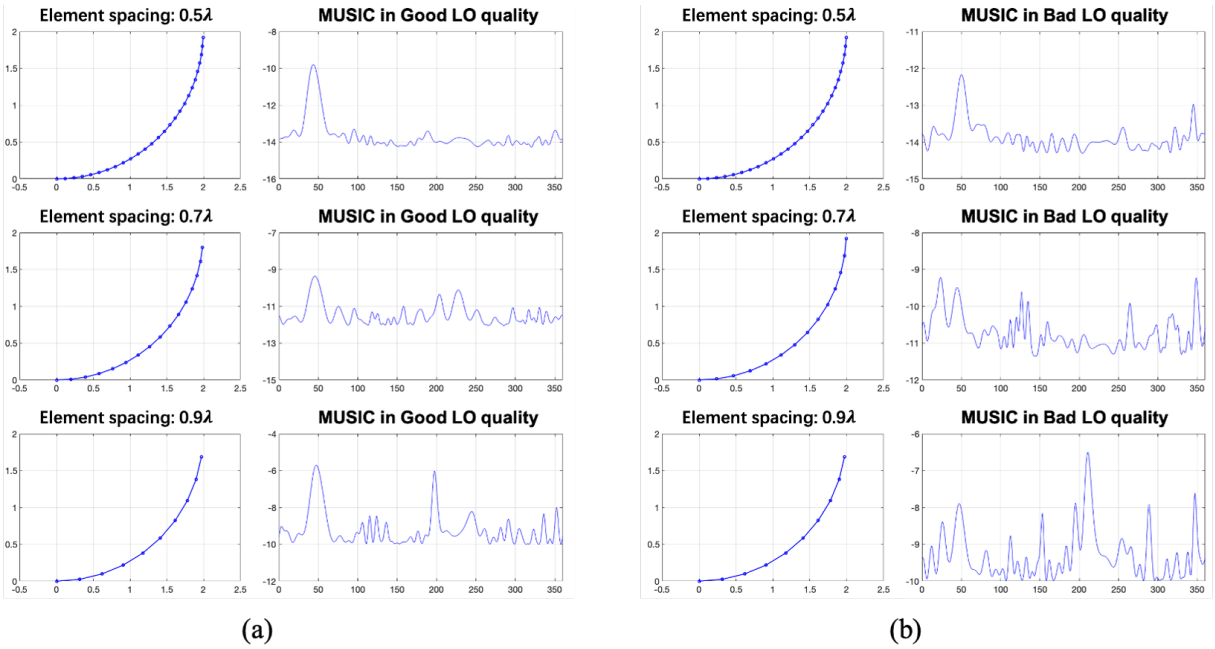

Figure 4.3: MUSIC Spectrum versus Array Element Spacing

It is clear from the figure that additional peaks appear in the MUSIC spectrum when the array elements are spaced more than half a wavelength, which meet our expectations. The reason is straightforward: the objective of estimating a DoA (i.e., θ in Eq.(3.12)) is to extract the spatial frequency (i.e., the term μ=$j\frac{2\pi}{\lambda}\Delta_n$ in Eq.(3.12)) from the signals received by the array; to determine θ uniquely from the spatial frequency μ, the one-to-one correspondence is desired [34]. As a result, it requires the element spacing satisfies $\Delta_n \leq \frac{\lambda}{2}$. When the element spacing does not satisfy this criterion, there will be an ambiguity in DoA determination, i.e., multiple solutions for the angles from a specific value of μ. Such

phenomenon will resulting in the MUSIC spectrum having multiple extra lobes other than the main lobe, as shown in Figure 4.3. When the oscillator stability is good and the element spacing is no more than 0.75λ, the extra lobes are lower than the main lobe, and the right DoA is still possible to be determined. However, if the oscillator stability is bad (e.g., TCXOs), it will add great uncertainty to the system and the DoA is difficult to be recovered from the MUSIC spectrum.

4.3.4 Monte-Carlo simulations

To evaluate the DoA estimation performance for these predictions in a more general case, we performed Monte-Carlo simulations with 5000 independent runs under the configurations above. The time consumption of the simulation is around 50 runs per minute. The DoA θ estimation error and the LO frequency estimation f_0 error are zero-mean for both the SAS approach and the joint estimation approach with true receiver positions. As for the case when applying the joint estimation with unknown receiver positions, the DoA θ estimation error is zero-mean; the estimation RMSE error of f_0 is around 1.35 Hz. This observation confirms to our expectation since the estimated value is actually a combination of the LO frequency offset and the receiver speed.

The simulation results are summarized in Table 4.1. It can be clearly seen from the table that for the joint estimation approach, the position measurement and the acceleration measurement provide very similar DoA estimation accuracy. The virtual array system is feasible to estimate the right DoA as long as the acceleration can be measured. Besides, the joint estimation provides slightly better accuracy than the SAS approach, which can be explained by the fact that, for low-quality oscillators, f_0 changes too much during the receiver's state from stationary to moving.

4.4 Implementation on Software-Defined Radios and Results

Our previous experiments in [80] were performed in an anechoic chamber, where both

Table 4.1: DoA Estimation Simulation Results over 5000 Runs

LO Compensation	RMSE f_0 error	RMSE θ error
Joint (with r_x)	0.32 Hz	8.04°
Joint (with a_x)	1.35 Hz	8.52°
SAS approach	0.34 Hz	9.17°

the transmitter and receiver were equipped with OCXOs containing less LO frequency offset. Also, the receiving antenna was moved by a mechanical turntable with a precise semicircular trajectory. Such a configuration is a luxury in many real-world scenarios, such as portable electronics. Therefore, the objective of experiments in this chapter is to test the feasibility of a virtual array under more realistic conditions. The transmitter and receiver are both equipped with low-quality LOs and off-the-shelf IMUs, which contain significant imperfection. The movement of the receiver was performed manually, following a linear trajectory. The measurement layout is an indoor environment with multipath components. The whole experiment serves as a proof-of-concept, providing DoA estimation results by tracking the positions or accelerations of the receiver.

4.4.1 Measurement setup

We validate the proposed algorithm by conducting experiments on a software defined radio (SDR) testbed. The transmitter is composed of a USRP-B205 SDR, while the receiver is composed of a USRP-E310 SDR. The transmitter is connected to a host laptop, and the receiver USRP contains a field-programmable gate array (FPGA). Both transmitter and receiver are equipped with an omnidirectional antenna VERT900 and a TCXO local oscillator, which will cause a LO frequency offset in the order of 5$\sim$50 Hz. The receiver is embedded with a low-cost IMU chip, model MPU-9150, which combines a triple-axis accelerometer, triple-axis gyroscope, and triple-axis magnetometer. The transmitter sends a periodic PSS sequence every 0.667 ms at a carrier frequency of 1 GHz (similarly to our simulations). The receiver correlates its received baseband signal with the transmitted sequence and detects the peaks in the correlation function, thereby finding the boundaries of

the received packet. This is done in real-time on the receiver's FPGA. Finally, the received packets are recorded by the USRP-E310 embedded microcontroller system for offline processing. The IMU measurement data is recorded in the same data file as the received packets by a separate thread.

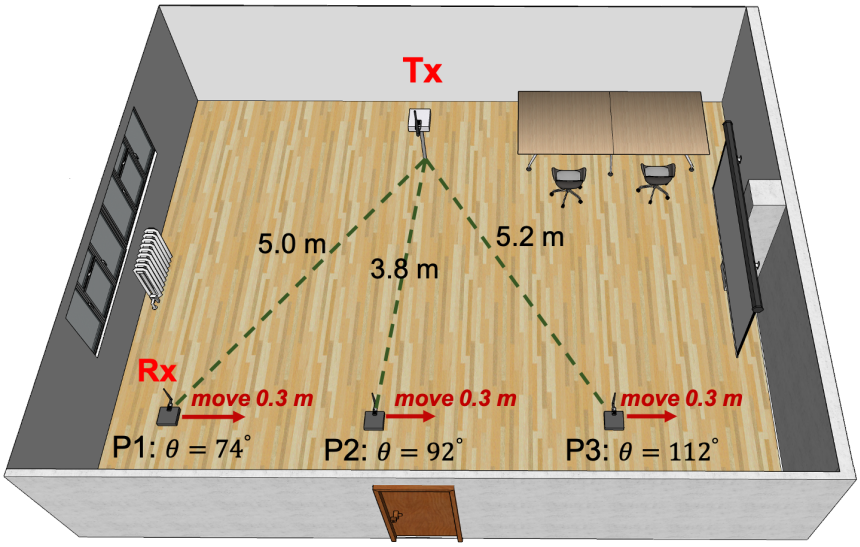

Figure 4.4: The layout of the measurement scenario. The transmitter position is fixed, and the receiver moves along a linear trajectory (0.3 m). The measurements are taken in 3 positions; for each position, the measurement is repeated 15 times [91].

The measurement was performed in a room whose layout is depicted in Figure 4.4. The dimension of the laboratory is approximately 10 m long and 7 m wide. The laboratory is equipped with hardware such as metal cabinets, tables and chairs, which will lead to multipath propagation as scatters. The transmitter is located at a height of 0.5 m. The receiver is placed at three different locations on the other side of the room at the height of 0.1 m, corresponding to the following DoAs: $[\theta_1, \theta_2, \theta_3] = [74, 92, 112]^{\circ}$. The experiment was repeated 15 times for each receiver position. The LoS visibility holds during the measurements and the SNR is around 30 dB. In each experiment run, the transmitter broadcasts the periodic sequences continuously. The receiver is first standing still for 15 s to avoid possible hardware instability. After 15 s, the receiver starts to receive packets, and the USRP is manually moved along a linear trajectory. The trajectory length is around

0.3 m, and the moving process lasts around 0.8 s. The acceleration is provided manually and therefore varies throughout the measurements. The receiver-embedded IMU records its movement states for later reconstruction of the trajectory. The number of the virtual array element is set to 10, so the WSSUS assumption and the spatial aliasing criterion are satisfied. We installed the receiver on a toy-sized trolley. A slide rail is also used to ensure a stable orientation and a consistent ground truth in each experimental run. Besides, although the receiver is moved manually, the corresponding manual errors would not significantly degrade the DoA estimation performance due to limited movement time.

4.4.2 Data Processing

In our experiments, the data processing consists of the trajectory reconstruction (with/without knowing the initial movement state), the LO phase offset compensation and the DoA estimation. For the trajectory reconstruction, the actual initial velocity is zero as the receiver is stationary before moving. In principle, the trajectory can be reconstructed through a UKF with the initial velocity as input. First, we investigate the case where we know the initial velocity. It is observed that some of the estimated trajectories drift off from the ground truth towards the end of the movement, as shown in Figure 4.5, with an RMSE error of 3.2 cm. This error is small enough to be neglected in further processing, since most of the drifts occur at the end of the movements. As for the case where the initial velocity is unknown, we reconstructed a *"fake"* trajectory by giving UKF a false initial velocity of 0.5 m/s and then integrating it with the real measured acceleration. The trajectory length error came to more than 20 cm, as we expected. Both trajectories satisfy the aforementioned motion constraints and will be verified in the DoA estimation. One thing to mention is that when using off-the-shelf IMUs (such as this paper), the movement time should be kept short (about $1\sim2$ s) to avoid large integration errors due to sensor bias.

Two techniques are proposed for eliminating the effect of the LO phase offset: the SAS approach and the joint estimation approach. The LO frequency offset f_0 varies continu-

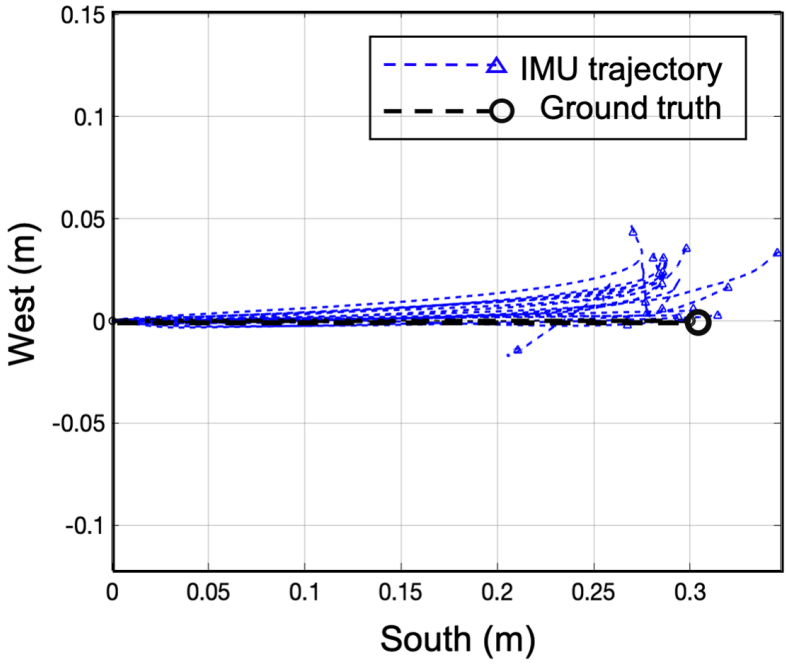

Figure 4.5: Comparisons between the real ground truth and the estimated IMU trajectories. The black dashed line indicates for the ground truth. The 15 blue dashed lines are estimation results of 15 measurements.

ously and independently with time. If the receiver can be stopped before moving, both methods can be applied to estimate the f_0. Otherwise, the joint estimate is more appropriate. For the SAS approach, the f_0 is estimated during the stationary process (0.8 s before moving) and then used for compensation; for the joint estimation approach, the f_0 and the θ are simulated simultaneously in a 2D MUSIC search. The measurement results are presented in the next section.

4.4.3 Results Analysis

Figure 4.6 shows the measured LO phase offset and the phase of the received signal (after compensation) when using the SAS approach. It can be seen in Figure 4.6a that the average LO frequency offset (which can only be estimated at standstill) changes consistently at the moments before and after the receiver moves. The consequence of this LO drift is evident in the observed phase in Figure 4.6b. Towards the end of the movement, it can be seen

that there is a linear drift in the observed phase due to the change in the LO frequency offset. Nevertheless, applying the MUSIC algorithm on the LO offset compensated signals provides an RMSE up to 13°.

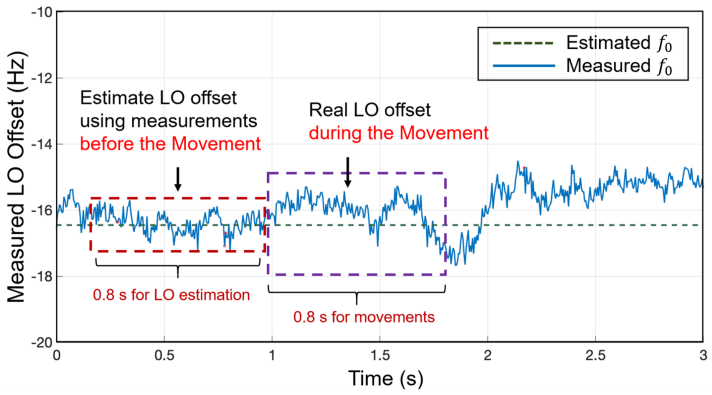

(a) Measured LO offset in real time

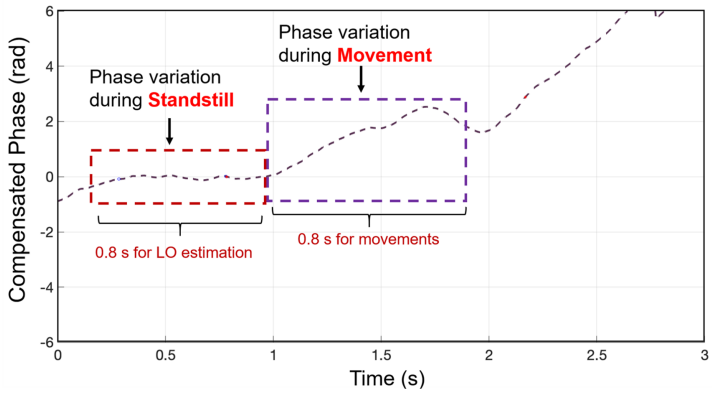

(b) Compensated phase in standstill and movement

Figure 4.6: Experiment results for the SAS approach. (a) LO phase offset measurements during standstill are used for LO offset compensation. (b) Phase variation during standstill after compensation is nearly negligible, and phase variation during movement after compensation can be observed [91].

Figure 4.7a shows an example of a 2D MUSIC spectrum when applying the joint estimation with the true IMU-reconstructed trajectory. A clear peak can be observed at a roughly true DoA of 73° and true f_0 at 14.8 Hz. As for the joint estimation with the fake trajectory, Figure 4.7b indicates a very similar DoA estimation result of 75° with a drifted f_0, which fits our simulation results. Therefore, both measurement and simulation results confirmed that the joint estimation could be applied to any virtual array user cases without

the receiver being at standstill. The DoA estimation is feasible even without knowing the initial movement states (velocity v_x, position r_x, etc.).

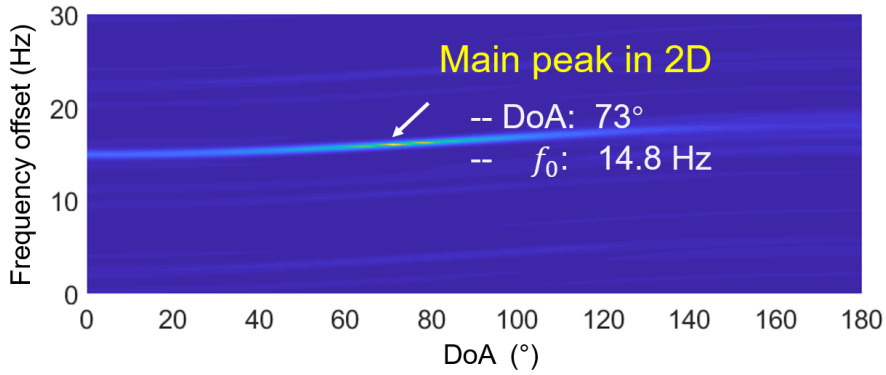

(a) Joint estimation with knowledge of initial velocity

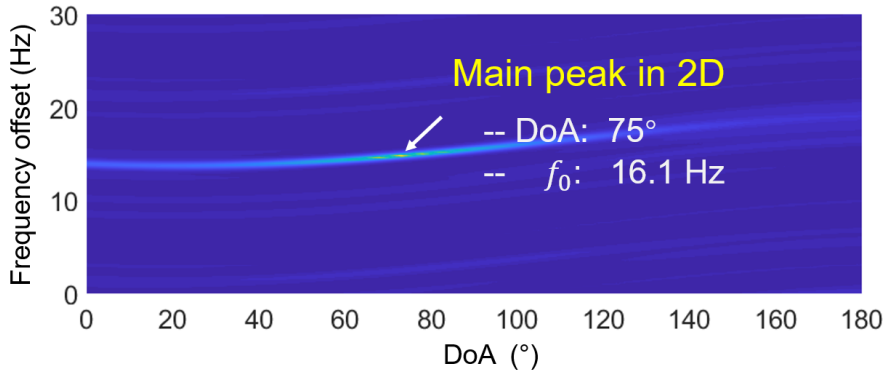

(b) Joint estimation without knowledge of initial velocity

Figure 4.7: Experimental results of the joint estimation approach (a) DoA is estimated with knowledge of receiver position, measured with IMU; (b) DoA is estimated by measuring the acceleration only [91].

The DoA estimation results of the SAS approach and the joint estimation approach are summarized in Table 4.2. First, it can be seen that in the joint approach, DoA estimation with knowledge of the receiver's initial motion state has higher accuracy, as inaccurate coordinates inherently introduce bias into the estimator. Secondly, the accuracy of the joint estimation (with r_x) is higher than in the case of the SAS approach, which also fits our simulation results. This can be attributed to the fact that, for low-quality oscillators, the frequency mismatch f_0 changes too much between the moment where the receiver is

standing still and where the receiver starts moving, which degrades the performance of the SAS compensation method.

Table 4.2: Measurement Errors over 15 Experiment Runs

Compensation Method	Position 1	Position 2	Position 3
RMSE in SAS	11.6°	12.9°	5.9°
RMSE in Joint (with r_x)	8.7°	12.1°	4.2°
RMSE in Joint (with a_x)	9.2°	13.5°	4.9°

While the measurement error can be considered high with respect to conventional physical multi-antenna arrays, it needs to be reminded that the experiment serves as a proof-of-concept to test the feasibility of the virtual array with real-world imperfections (LO offsets, manual errors, multipath distortions, etc.). The proposed system is a fundamental shift from conventional DoA estimation methods: We are trying to estimate the DoA with an off-the-shelf single-antenna device, which requires self-identifying receiver positions/accelerations and compensating LO frequency offsets. In that respect, performance degradation can be expected. We believe that further optimization of the LO frequency offset elimination is possible; better measuring/processing of the IMU data and a larger size of the receiver trajectory can also improve the DoA estimation performances. These will be investigated in our future work.

4.5 Conclusion

In this chapter, we have investigated the feasibility of the virtual multi-antenna array system and improve its robustness to account for real-world applications. We performed a comprehensive nonlinear observability analysis for the system and then provided two theoretical observations: The DoA and the LO frequency offset can be jointly estimated if the receiver's movement contains a certain acceleration; The DoA can be estimated by measuring the receiver's acceleration only, without the knowledge of precise receiver positions. Simulations were conducted to confirm both of these theoretical observations. These

theoretical foundations provide guidance for designing feasible and user-friendly receiver trajectories to meet specific application requirements. Finally, the proposed system was implemented on a software-defined radio that integrates off-the-shelf components such as a low-cost oscillator TCXO and a generic IMU. The experiments show that the DoA can still be estimated with DoA RMSE between 5° and 13° in the presence of hardware biases.

Both simulations and experimental results show that the virtual array can be an alternative for DoA estimation by dispensing with cumbersome and expensive multi-antenna arrays, which simultaneously reduces the cost and increases the practicability of conventional direction finding systems. The proposed technology has great potential in applications with high cost or form-factor constraints, including portable electronics, NB-IoT networks, and indoor localization. As the virtual array exploits the mobility of transmitters, it can also be applied for target tracking in vehicle-to-Everything (V2X) networks, especially for aerial vehicles that more likely to maintain the LoS visibility with ground targets. In the next chapter, we will evaluate the performance of the proposed virtual array system in UAV-based communication scenarios.

CHAPTER 5

VIRTUAL MULTIANTENNA ARRAY IN UAV-ASSISTED NETWORKS

The aim of this chapter is to demonstrate the feasibility and potential benefits of the virtual antenna array systems presented in Chapters 3 and 4 by examining its application in UAV-based communication networks. The two local oscillator frequency offset compensation algorithms are applied to UAV scenarios to explore their performance under different oscillator qualities. Detailed simulations are performed to evaluate some of the channel parameters that may affect the accuracy of the DoA estimation methods. Different types of trajectories have also been investigated to compare their performance.

5.1 Virtual aray system model in UAV communications

Unlike conventional one-dimensional DoA estimation in terrestrial networks (azimuth only), the direction of signals in aerial networks is usually expressed by the azimuth angle ϕ and the elevation angle θ. In general, two-dimensional arrays are required to estimate the azimuth and elevation of a source. Commonly used 2D array geometry includes the uniform circular arrays (UCAs), uniform rectangular arrays (URAs), and uniform planar arrays (UPAs), where detailed information can be found in [135]. For simplicity, the MUSIC algorithm is applied in this chapter for corresponding 2D-DoA estimation problems, where other 2D-DoA estimation algorithms can be found in [136, 137].

The requirement of the 2D array geometry also applies in the proposed UAV-based virtual array systems, i.e., the UAV receiver needs to move along 2D trajectories to estimate azimuth and elevation simultaneously. A simplified diagram of the virtual array system in UAV-based communication networks is shown in Figure 5.1a, and an illustration of directions for the incoming signal is provided in Figure 5.1b.

By reusing the data model described in Chapter 3, we consider that a narrowband signal

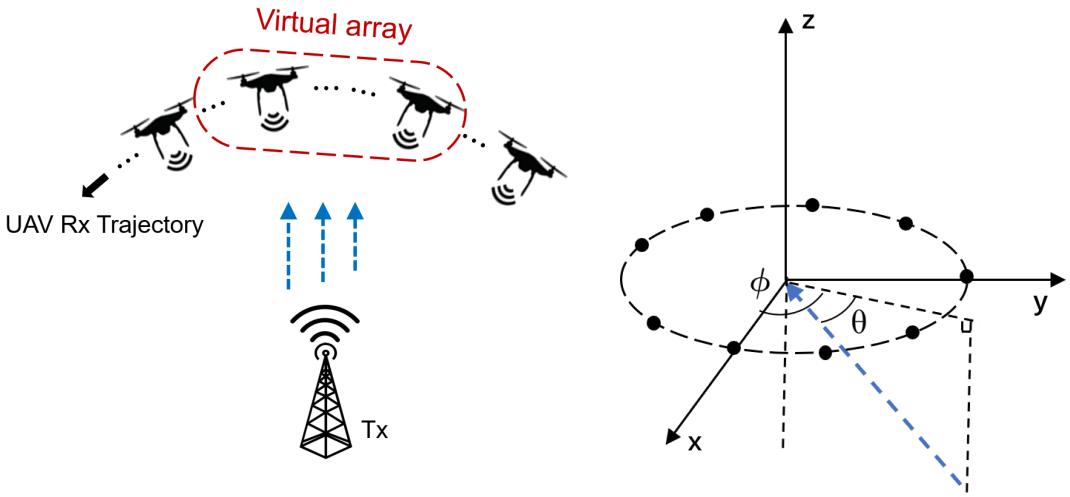

(a) UAV-based virtual antenna array (b) Angular relationship

Figure 5.1: Diagram of the UAV-based virtual array [138].

of wavelength λ is emitted by the ground transmitter. The UAV is equipped with a single omnidirectional antenna and moves along a 2D path when receiving signals. Assume that the position of the UAV when it receives the first packet is the initial position $\vec{r}[0]$; the relative position of the UAV is represented by $[x_n, y_n, z_n]$ for $n = 0, \ldots, N$ when the UAV moves from $\vec{r}[0]$ to $\vec{r}[n]$. Also, since the signal arrives at the UAV from the far-field, the DOA is considered constant at each UAV position. We still denote $s\big[m\big]$ the baseband representation of the transmitted signal (for $m = 1, ..., M$) and $r\big[n, m\big]$ the m-th baseband sample of the received signal when the UAV moves to $\vec{r}[n]$ (with sample period T_s). As a result, the received signal $r\big[n, m\big]$ can be written as:

$$r\big[n, m\big] = h\big[n, m\big] * s\big[m\big] \cdot e^{j(\psi_0 + 2\pi f_0(t_n + mT_s))} + \omega\big[n, m\big] \tag{5.1}$$

where $h\big[n, m\big]$ is the CIR and the $e^{j(2\pi f_0(t_n+mT_s))}$ is the phase drift introduced by the LO frequency offset f_0.

In general, the impulse response $h\big[n, m\big]$ provides details about the temporal, spatial and energy information of multipath components of the channel. We consider that the CIR remains constant from t_n to t_{n+1}, thus $h\big[n, m\big]$ is simplified to $h\big[n\big]$ in the following. When

we consider a LoS channel for simplicity, the $h\big[n\big]$ can be written as:

$$h[n] = \alpha \cdot e^{j\vec{\beta}(\phi,\theta)\cdot\vec{r}[n]} \tag{5.2}$$

where α is amplitude of the channel and $\vec{\beta}(\phi,\theta)$ is the wave vector. The term $e^{j\vec{\beta}(\phi,\theta)\cdot\vec{r}[n]}$ is the corresponding phase drift due to UAV movement, i.e, the phase drift used to perform 2D-DOA estimation in the virtual array system. In the target aerial space, the term $\vec{\beta}(\phi,\theta)\cdot\vec{r}\,[n]$ can be developed as

$$\vec{\beta}(\phi,\theta)\cdot\vec{r}\,[n] = \frac{2\pi}{\lambda}(x\,[n]\,cos(\phi)cos(\theta) + y\,[n]\,sin(\phi)cos(\theta) + z\,[n]\,sin(\theta)) \tag{5.3}$$

where $[x_n, y_n, z_n]$ should be measured by our system.

In practice, phase distortion caused by the LO frequency offset and phase drifts caused by the UAV movement are difficult to separate, although only the latter is useful in virtual arrays. To address this challenge, two LO offset compensation methods are provided in Chapter 3. However, as the signal model expands to a high dimension, both methods need to be modified accordingly.

For the SAS approach, the UAV receiver needs to stand still before moving, then using the estimated f_0 to compensate the phase distortion. As for UAV scenarios, the SAS algorithm needs to perform a 2D MUSIC spectrum search in the azimuth and elevation domains for the compensated signal.

The joint estimation approach needs to rewrite the output of the array in Eq.(5.1) by stacking the N received packets in a column vector as:

$$r\,[m] = a\,(f_0,\phi,\theta)\,X\,[m] + \omega\,[m] \tag{5.4}$$

where $a\,(f_0,\phi,\theta)$ is the 3D steering vector and $X\big[m\big]$ is constant for all virtual antennas,

expressed by:

$$X\left[m\right]=\alpha\cdot s\left[m\right]\cdot e^{j(\psi_0+2\pi f_0 mT_s)} \tag{5.5}$$

and the steering vector $a\left(f_0,\phi,\theta\right)$ represents parameter of interest that causing the phase to change. As a result, the steering vector $a\left(f_0,\phi,\theta\right)$ can be expressed by:

$$a\left(f_0,\phi,\theta\right)=\begin{bmatrix} e^{j(2\pi f_0 t_0+\frac{2\pi}{\lambda}\cdot(x_0 cos\phi cos\theta+y_0 sin\phi cos\theta+z_0 sin\theta))} \\ e^{j(2\pi f_0 t_1+\frac{2\pi}{\lambda}\cdot(x_1 cos\phi cos\theta+y_1 sin\phi cos\theta+z_1 sin\theta))} \\ \vdots \\ e^{j(2\pi f_0 t_{N-1}+\frac{2\pi}{\lambda}\cdot(x_{N-1} cos\phi cos\theta+y_{N-1} sin\phi cos\theta+z_{N-1} sin\theta))} \end{bmatrix} \tag{5.6}$$

Similarly to the previous case in (3.19), the noise subspace E_S is determined by developing the eigen-decomposition for the covariance matrix of $r\left[m\right]$, and the corresponding MUSIC spectrum is defined as:

$$P_{MU}\left(f_0,\phi,\theta\right)=\frac{1}{a^H\left(f_0,\varphi,\theta\right)E_S{E_S}^H a\left(f_0,\phi,\theta\right)} \tag{5.7}$$

where the target parameter can be estiamted simultaneously with a three-dimensional search:

$$\left(\hat{f}_0,\hat{\phi},\hat{\theta}\right)=\underset{(f_0,\phi,\theta)}{\arg\max}\left\{P_{MU}\left(f_0,\phi,\theta\right)\right\} \tag{5.8}$$

To summarize, although the SAS approach and the joint estimation approach can theoretically eliminate the effects of LO frequency offsets in aerial networks, their performance should still be tested and evaluated for the UAV-based scenarios. In addition, the feasibility of the UAV-based virtual array system needs to be investigated by considering the impact of more realistic factors, including LO quality, ATG channel characteristics, SNR levels, and the shape of UAV trajectories.

5.2 Simulation Implementation

5.2.1 Simulation Configuration

Experiments with real aerial platforms are generally time-consuming and costly. Therefore, this chapter investigates the performance of the UAV-based virtual array through detailed simulations. First of all, we consider the problem of interest is to estimate the DoA of a ground transmitter by analyzing the received signal at the UAV-based virtual array under an urban city environment. The received signal follows the description in Eq. (5.1) and is generated by simulating the channel and the LO frequency offset simultaneously.

More specifically, the CIR is provided by the Ray-tracing simulator in Chapter 2. Therefore, the effect of ATG channel characteristics on the accuracy of virtual arrays (e.g., unique multipath distribution, limited angular spread) can be investigated. The phase offset $e^{j(2\pi f_0(t_n+mT_s))}$ due to the LO frequency offset are simulated by applying the state-space model in Chapter 4. Simulations are performed for both TCXO and OCXO configurations to evaluate the performance of the system with respect to different LO qualities. Additional noise is manually added to the signal model, while the effect of the signal-to-noise ratio (SNR) has also been investigated. The SNR in this chapter is defined as the ratio of the total received multipath power to the power of background noise. In addition, the shape and size of the 2D UAV trajectory may also affect the accuracy of the estimation, so we evaluated the performance of four differently shapes of trajectories. We assumed that the UAV coordinates in all four trajectories were known. The carrier frequency is set as 2.4 GHz and the half wavelength is around 0.06 m.

One example from the simulation is depicted in Figure 5.2 where the UAV is flying over the center of a 3D urban city map at an altitude of 80m. The figure shows that the UAV receiver moves in a circular trajectory and implicitly creates a circular array. The array contains 80 antenna elements and each separated by half a wavelength (6 cm) so that the total length of the trajectory is around 4.74 m. There are also 2000 ground transmitters

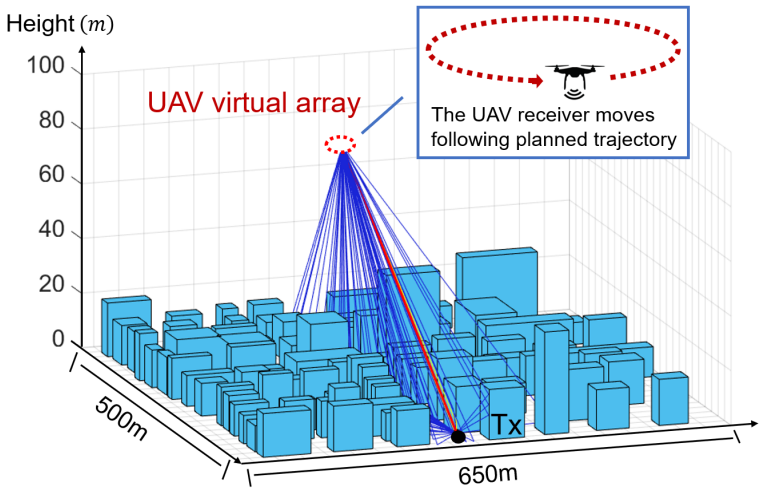

Figure 5.2: One example snapshot from the UAV-based virtual array simulation [138].

distributed over the ground, and half of them have the LoS visibility. For each transmitter, the ray-tracing simulator computes the impulse response $h[n]$ (for $n = 0, 1, ..., 79$) and records the direction and power for each ray. After the received signal is calculated as Eq. (5.1), the 2D virtual array algorithms are applied to estimate the corresponding DOA.

5.2.2 2D-DOA Estimation Result

This subsection provides one DoA estimation realization of the simulated 2D UAV-based virtual array algorithm. In this example, the receiver and transmitter are equipped with an OCXO; the LoS visibility holds and the SNR is 20 dB. Two LO frequency offset compensation techniques are both applied. Similar processes are performed for all the 2000 transmitters under each SNR configuration.

The result of the SAS method is shown in Figure 5.3. In this case, received signals after the frequency offset compensation are used to estimate the azimuth and the elevation angle simultaneously via a 2D MUSIC search. As shown in the figure, a clear peak is observed at azimuth 8° and elevation 56°, which is very close to the true DOA of 12° for azimuth and 52° for elevation.

The result of the Joint Estimation method for the same snapshot is shown in Figure 5.4.

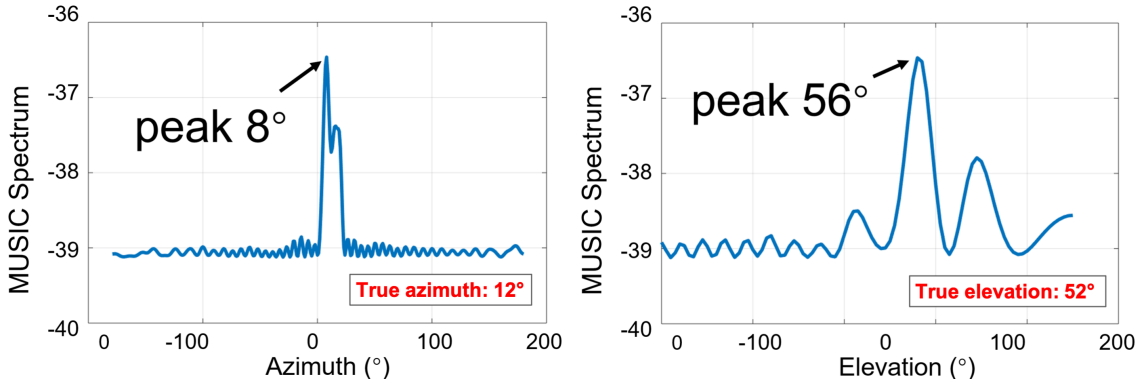

(a) Azimuth estimation for 2D Virtual array (b) Elevation estimation for 2D Virtual array

Figure 5.3: SAS Estimation for the 2D Virtual Array

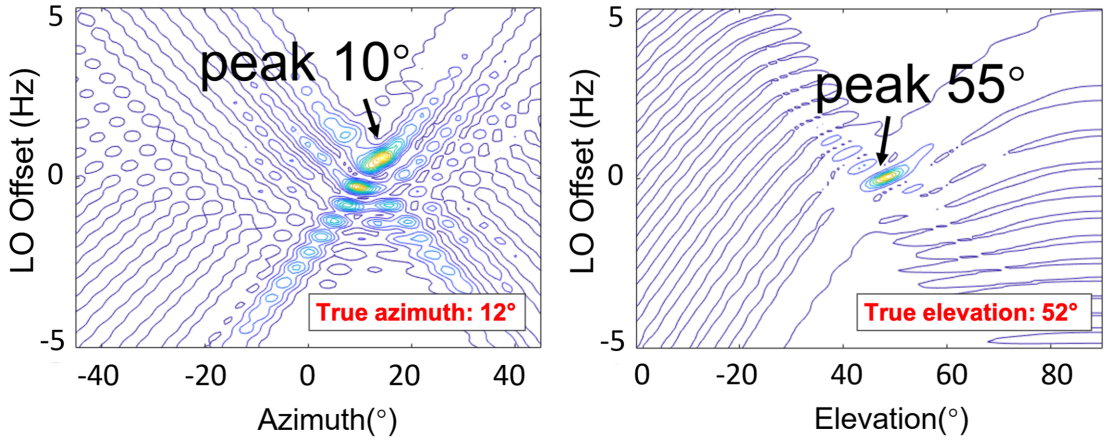

(a) Joint estimation (LO offset & Azimuth) (b) Joint estimation (LO offset & Elevation)

Figure 5.4: Joint Estimation for the 2D Virtual Array

In this case, only the received packets during the UAV movement were used for processing. The peak of the spectrum indicates the estimated LO frequency offset f_0, and also the estimated DOA (azimuth and elevation) corresponding to the peak. A clear peak can be identified at 10° for azimuth and 55° for elevation, close to the true DOA of 12° for azimuth and 52° for elevation.

5.3 UAV-based Virtual Array Performance Evaluation

This section evaluates the performance of the proposed UAV-based virtual array system based on extensive simulation results by considering parameters such as the LoS visibility, LO quality, LO frequency offset compensation method, SNR level, and the impacts of different UAV trajectories. Comparisons between different simulation setups and their effects on the estimation accuracy are discussed in following subsections.

5.3.1 Comparison between different LO qualities

The magnitude and frequency stability of the LO frequency offset between transceivers depends on the quality of their embedded LO oscillators. Low-quality oscillators may cause significant phase distortions that may fail the DoA estimation process. In general, the configuration of LOs in the UAV-based virtual array system can be divided into three categories: 1) both transmitters and receivers are equipped with high-quality LO oscillators, e.g., OCXOs; 2) both transmitters and receivers are equipped with low-quality LO oscillators, e.g., TCXOs; 3) the receiver oscillator is designed to meet the specification of the localization system, thus with good frequency stability; the transmitter to be located are using oscillators that suit their own needs and therefore are not guaranteed to be stable. The last category can be considered as the most common case in real-world applications. The subject of this subsection is to verify the feasibility of the UAV virtual array system regarding different LO quality conditions.

Therefore, we perform extensive simulations by modeling the above three LO quality configurations. The LO frequency offset in different oscillator setups are simulated by using the state-space model described in Eq.(4.21), where the process noise parameters are $(q_1^2 = 8.47 \times 10^{-22}; q_2^2 = 5.51 \times 10^{-18})$ for TCXOs and $(q_1^2 = 5.25 \times 10^{-24}; q_2^2 = 1.77 \times 10^{-21})$ for OCXOs [134, 94]. The trajectory considered in this subsection is the uniform circle in Figure 5.2 and the movement time is 2s. The SNR is set to 20 dB, and the

joint estimation method is applied to resolve the phase distortion due to the LO frequency offset. Simulations are performed for the 1000 ground transmitters with LoS visibilities and the 1000 ground transmitters without LoS visibilities.

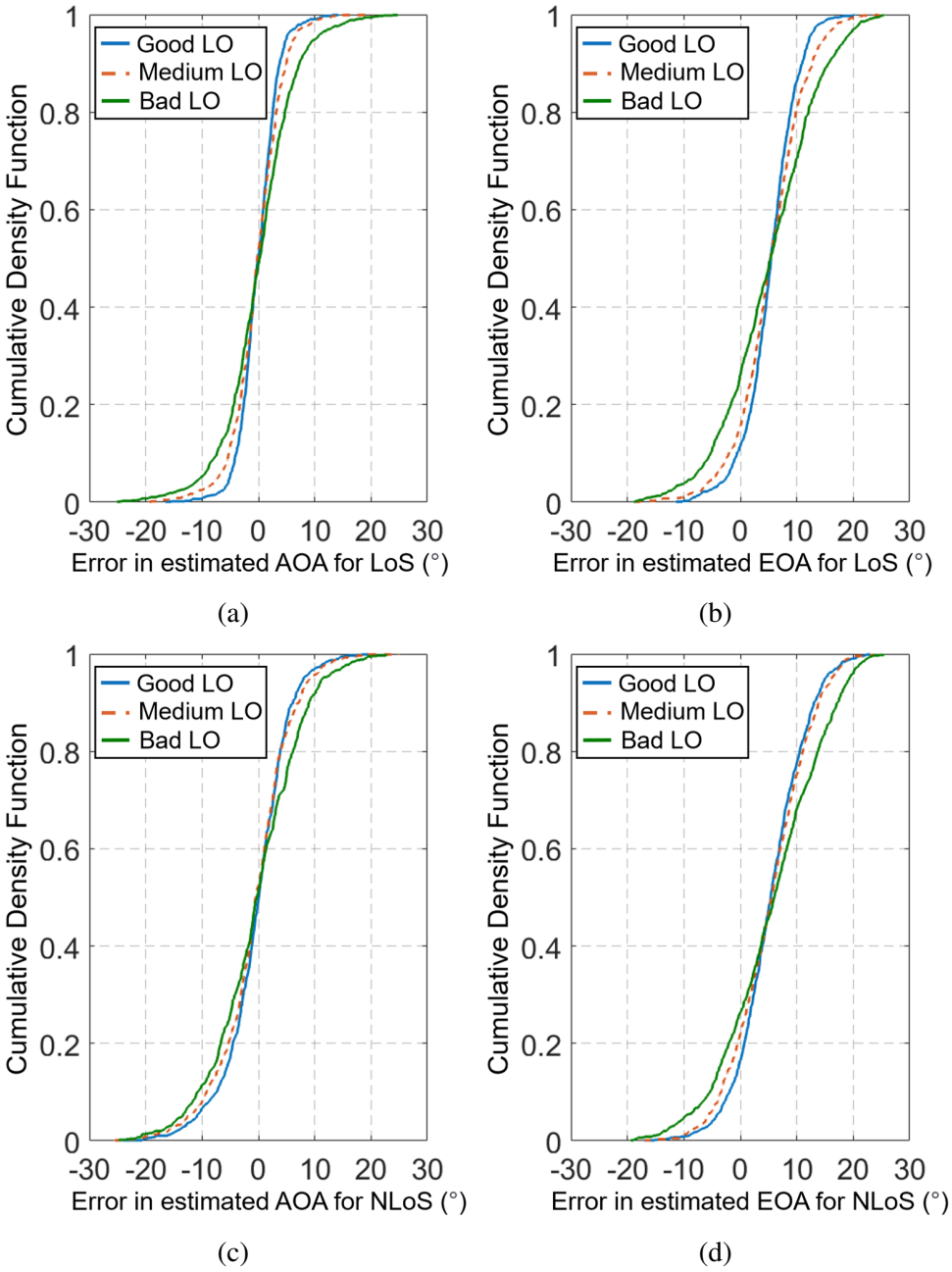

Figure 5.5: Estimation Error *versus* LO Qualities

Figure 5.5 presents the CDF of the estimated error under different LO quality configurations for the joint estimation in all simulation runs. We have also calculated the RMSE

for each configuration, which are summarized in Table 5.1. It is clear from the figure and the table that the estimation accuracy of the virtual array system degrades with worse LO quality configurations. The significant LO frequency offset caused by imperfect oscillators can not be fully compensated, leading to higher estimation errors. However, even in the worst-case scenarios (NLoS propagation, both equipped with TCXOs), the RMSE for both AOA and EOA are still lower than 10°, which means the system remains applicable.

Table 5.1: 2D-DOA RMSE versus LO Qualities

LO quality	AOA		EOA	
	LoS	NLoS	LoS	NLoS
Good LO	3.39°	5.81°	4.58°	6.01°
Medium LO	4.44°	6.51°	5.92°	6.68°
Bad LO	7.41°	8.83°	9.21°	9.73°

The other observation from the simulation results is that the estimation errors in the NLoS scenarios are more significant than in the LoS scenarios since the absence of a LoS path degrades the system performance. However, such DoA estimation accuracy is still satisfying compared to typical DoA estimation techniques in terrestrial NLoS communication scenarios. This observation can be explained by the conclusion in Chapter 2, i.e., the angular spreads at UAV platforms are minimal for both LoS and NLoS scenarios, which has an excellent benefit for DoA-based localizations.

Therefore, simulation results in this subsection proved the feasibility of the UAV-based virtual array system for both LoS and NLoS scenarios. The performance of the proposed DoA estimator improves or degrades with a better or worse LO quality conguration. These results indicate that the UAV-based virtual array system can be feasible with cheap, off-the-shelf hardware, which typically has significant LO frequency offsets.

5.3.2 Comparison between LO offset compensation methods

Two methods are provided in this thesis to address the phase distortion in the virtual array system: the SAS method and the joint estimation method. The feasibility of these two methods relies on a fundamental assumption: the LO frequency offset does not change significantly with time, which is theoretically true if the movement lasts in a few seconds. In this subsection, we aim to evaluate the performance of the SAS method and the joint estimation method in UAV communication scenarios, especially for cases when the motion duration keeps longer and results in the LO frequency offset drifts.

The simulation applies these two LO compensation methods for all 2000 ground transmitters. We consider the transmitter is equipped with a TCXO, and the UAV receiver is equipped with an OCXO. The UAV moves along the circular trajectory with 80 elements, and the movement time is set to 2s, 5s, 8s, respectively. The drift of the LO frequency offset becomes severer over time and is also modeled by the state-space model. The SNR is set to 20 dB. Figure 5.6 presents the CDF of the estimated error for all simulation runs; the RMSEs of both methods with respect to the different movement times are also provided in the figure.

The first observation from Figure 5.6 is that when the UAV movement time is limited to 2s, both the SAS method and the joint estimation method provides pretty good estimation performance. The estimation accuracy of the joint estimation method is slightly better than the SAS method for both LoS and NLoS scenarios. This result can be explained by the fact that the LO frequency offset changes too much when the UAV moves from being standstill, thus reducing its estimation performance. On the contrary, the joint estimation directly applies the received packets during movement to estimate the target DoA, thus provides better estimation accuracy.

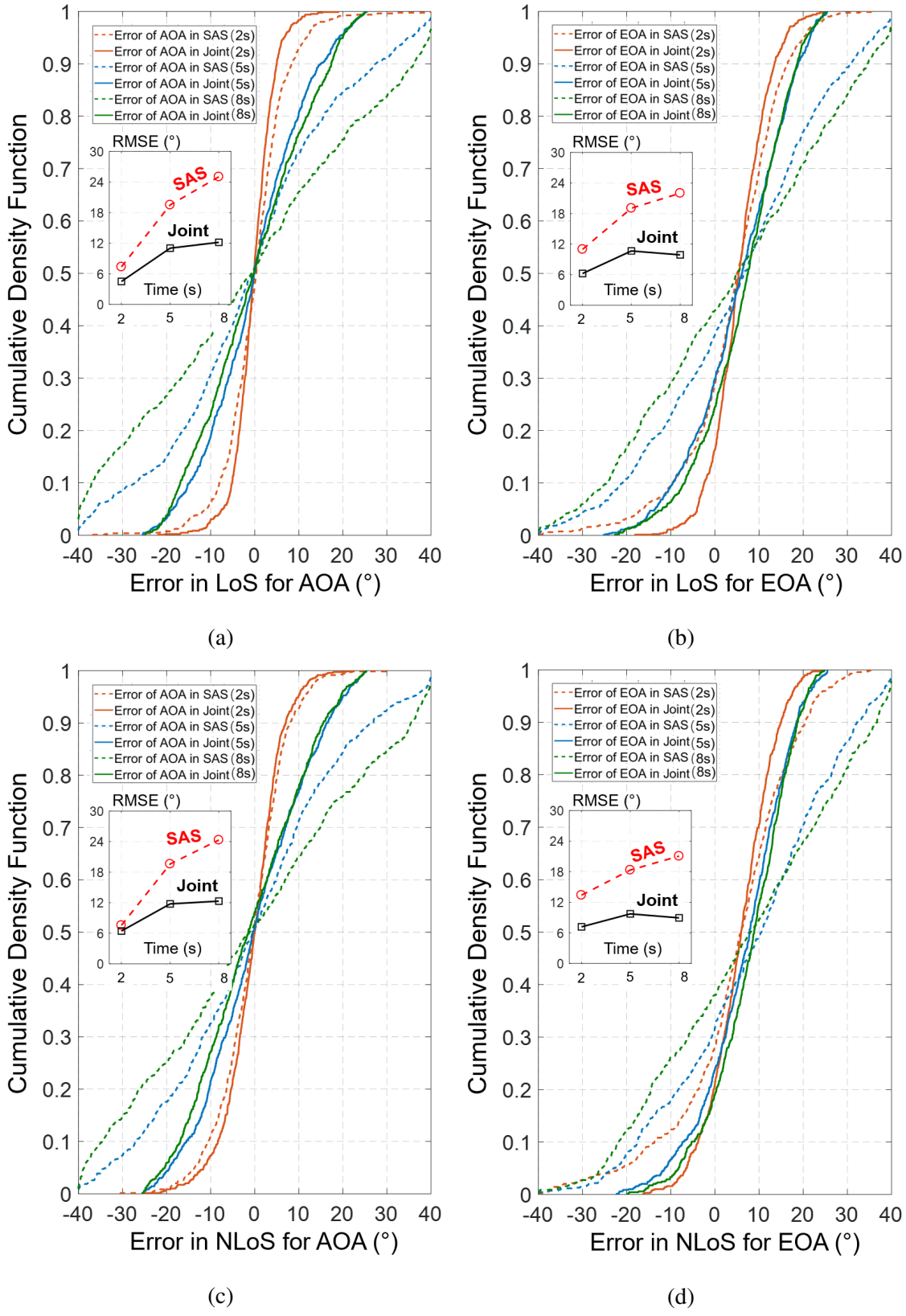

Figure 5.6: Estimation Error *versus* LO Offset Compensation Methods

When the movement time extended to 5s and 8s, apparent performance degradations are observed for both the SAS and the joint estimation method. Such performance degradations are expected since the oscillators considered in this subsection have poor frequency stability, which makes the LO frequency offset drift with time. As a result, the phase distortion in Eq.(5.1) does not accumulate linearly over time, which makes it impossible to be fully compensated with the SAS method. Similarly, the phase of received packets cannot be characterized by the adapted steering vector in Eq.(5.6), which leads to worse DoA estimation accuracy for the joint estimation method. In addition, the degradation of the SAS method becomes more severe over time, which makes it less suitable for DoA estimation when flying UAVs for long periods.

In summary, in the UAV-based virtual array system, both the SAS method and the joint estimation method provide good 2D-DoA estimation performance in a short movement time, where the joint estimation method provides slightly better accuracy. The performance of both methods degrades over longer periods of UAV movement as the LO frequency offset fluctuates over time and cannot be considered as a constant. Therefore, the choice of compensation methods in real-life applications first depends on the movement time. The joint estimation is recommended for systems with longer movement time. If the movement time is short enough to keep the LO frequency offset constant, the choice of compensation methods depends more on the task to be performed by the UAV. The SAS method is straightforward to design and apply; However, it requires the UAV receiver to stand still before the movement, which leads to extra constraints on the UAV flight. The joint estimation method does not require the UAV to stop before moving, but such usage flexibility comes at the cost of more computation power to perform 3D MUSIC searches.

5.3.3 Comparison between different SNR

The performance of conventional subspace-based DoA estimation algorithms is easily affected by the SNR of environments. More specifically, a high SNR leads to more apparent

differences between the signal eigenvalues and the noise eigenvalues, which usually improves the MUSIC estimation performance [139]. On the contrary, a low SNR can lead to misrecognition of the signal source, making it difficult for MUSIC algorithms to estimate DoAs, especially where multiple incident signals come from close directions [87]. To investigate the effect of the SNR on the performance of the virtual array system, we performed extensive simulations in a wide range of SNR conditions (from 0 dB to 35 dB).

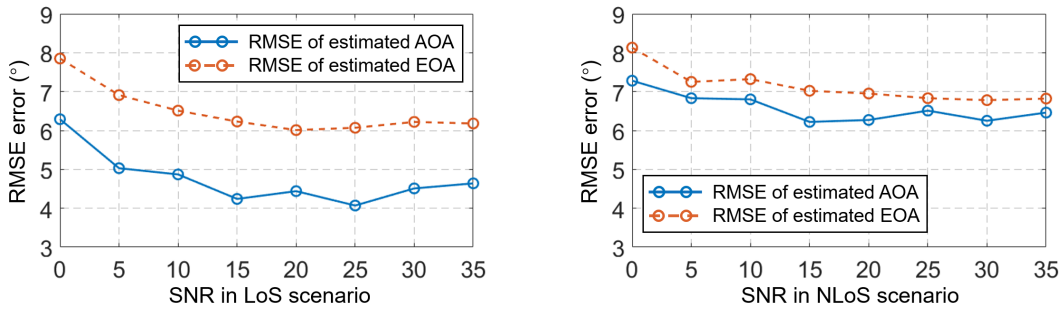

(a) (b)

Figure 5.7: Estimation Error *versus* SNR

Figure 5.9 compares the RMSE values of the estimated AOA and EOA versus the SNR of the system. According to Figure 5.7a and Figure 5.7b, we can see that for both LoS and NLoS scenarios, the RMSE first decreases as the SNR increases; the estimation performance stabilizes when the SNR reaches a certain threshold (at around 15 dB). When the SNR exceeds 15 dB, the RMSE fluctuates without a clear tendency.

The observations above can be explained as follows: At low SNRs, the noise subspace is very difficult to estimate from the received signal packets, and the performance of the MUSIC methods is significantly degraded. Therefore, the increases of SNR offer a significant improvement in DoA estimation accuracy. However, at high SNRs, the error in DoA estimation is dominated by the imperfections due to the LO frequency offset; the effect of improving the SNR on DoA estimation is therefore not obvious.

In summary, the simulation results show that the DoA estimation accuracy of the virtual array system improves as the SNR increases. A high SNR leads to better signal subspace

reconstruction in the MUSIC algorithm. However, such performance improvement is not infinite since when the SNR exceeds a certain threshold, the estimation error will be dominated by the LO frequency offset.

5.3.4 Comparison between different UAV trajectories

In above subsections, we consider that the UAV flies along a full circle and thus creates a uniform circular array, as shown in Figure 5.2. Although the circular array is a widely used structure in conventional 2D-DoA estimation systems, it is still somewhat unrealistic to have the UAV fly in circular trajectories for every mission. Therefore, in this subsection, we investigate the feasibility of the UAV-based virtual array when applying more trajectory shapes.

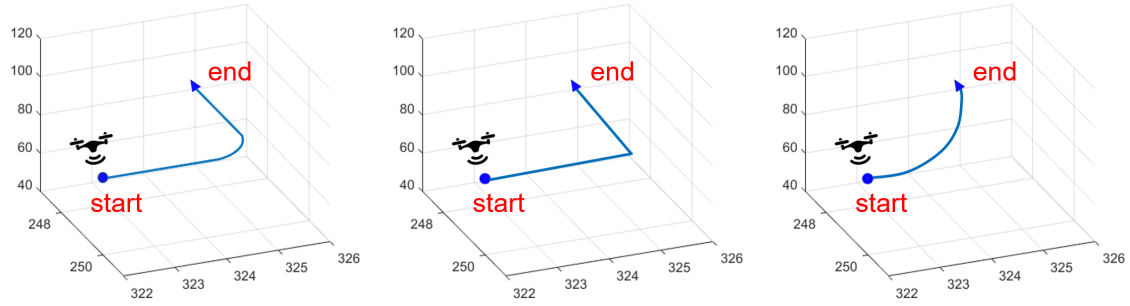

(a) Rounded-rectangle shape (b) Rectangle shape (c) Ellipse shape

Figure 5.8: Extra UAV Trajectories in Virtual Array

As shown in Figure 5.8, three types of trajectories are implemented into the simulation while the rest of the setup stay the same. The SNR is fixed at 20 dB. The RMSE of all four trajectories (including the original circular trahectory) are summarized in Table 5.2.

It can be seen from Table 5.2 that there is no significant difference between different trajectories. This phenomenon can be explained by the fundamental effect of the array geometry in general DoA estimation problems. The array geometry plays a significant role in determining the shape and properties of the array manifold, and most DoA estimation algorithms rely on searching for response vectors over the array manifold that satisfies a

Table 5.2: 2D-DOA RMSE versus UAV Trajectories

	LO quality	AOA		EOA	
		LoS	NLoS	LoS	NLoS
Circular	Good LO	3.79°	5.81°	4.58°	6.01°
	Medium LO	4.44°	6.51°	5.92°	6.68°
	Bad LO	7.41°	8.83°	9.21°	9.73°
Rounded-rectangle	Good LO	4.02°	5.54°	4.43°	6.19°
	Medium LO	4.37°	6.36°	6.01°	8.34°
	Bad LO	6.68°	7.94°	8.83°	9.92°
Rectangle	Good LO	3.37°	5.72°	4.45°	5.88°
	Medium LO	4.51°	6.22°	6.03°	7.06°
	Bad LO	6.90°	8.66°	8.82°	10.17°
Ellipse	Good LO	3.51°	5.65°	4.83°	5.93°
	Medium LO	5.02°	6.28°	5.85°	6.94°
	Bad LO	7.55°	7.94°	8.46°	8.67°

given criterion. For example, in the case of the MUSIC algorithm, the manifold is searched for vectors that are orthogonal to the estimated noise subspace [89]. In 2D-DoA estimation, if the array geometry stays in 1D (i.e., linear shape), some vectors in the array manifold can be written as linear combinations of other vectors, which will result in significant DoA estimation errors. On the contrary, the four non-linear UAV trajectories discussed in this subsection all have large sizes on the x-y plane, which results in good resolution of the corresponding array manifolds. Therefore, the RMSEs provided by these four trajectories are very similar.

In summary, the performance of the UAV-based virtual array system is not dependent on specific trajectories as long as the requirements for a two-dimensional shape are met, which allows users to design customized UAV trajectories for their own needs. The other observation is that the size of the UAV trajectory on a 2D plane may have significant impacts on the estimation performance, which will be investigated in the following subsection.

5.3.5 Comparison between Trajectory sizes

The resolution of conventional DoA estimation algorithms strongly relies on the number of array elements, as well as the size of the array, as each element is usually spaced apart by half a wavelength [34]. For the proposed virtual array systems, the size of an array indicates the length of a 2D UAV trajectory. In the above subsections, the UAV trajectory length is approximately 5 m, and the number of virtual antenna elements is 80. Such configuration is almost prohibitive with realistic physical antennas; however, it is easy to achieve with the UAV platform. Nevertheless, the performance of the UAV-based virtual array system with less number of antenna elements, i.e., shorter 2D trajectories, still needs further investigation. The significance of this subject is to find the shortest flight path that guarantees the accuracy of the DoA estimation, which will save the battery power of the UAV and reduce the computational burden.

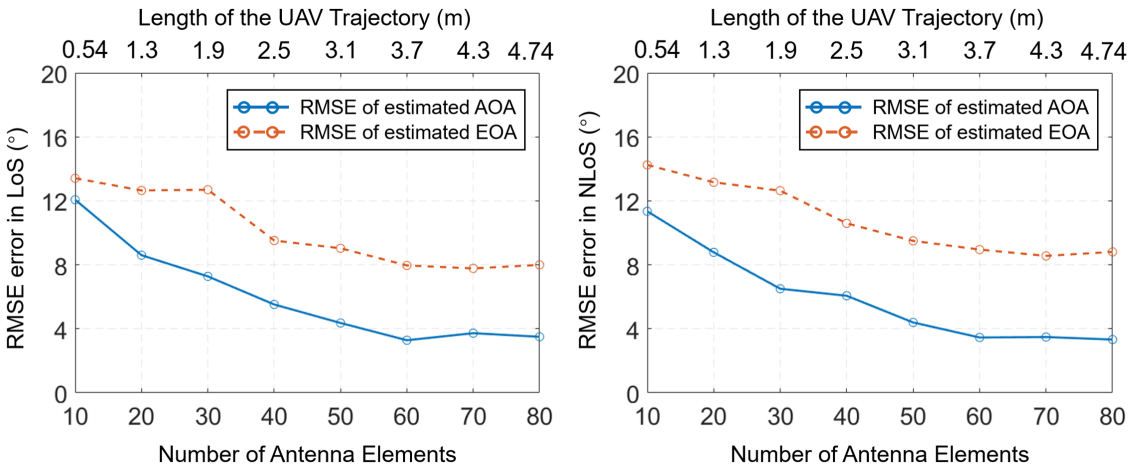

(a) (b)

Figure 5.9: Estimation Error *versus* Trajectory Size

Figure 5.9 presents the RMSE error of the proposed system for different lengths of UAV trajectories, by varying the number of antenna elements in a virtual array. We consider the circular array geometry introduced in subsection 5.2.1. When the number of antenna elements is set to 10, the trajectory is a short arc (one-eighth of a circle) with a length of

$0.6 \times 9 = 0.54$ m. When the number of antenna elements increases to 80, the trajectory is a full circle with a length of $0.6 \times 79 = 4.74$ m.

As can be seen from the RMSE curves, the performance of the virtual array system increases as the number of array elements increases, and the performance improvement stabilizes after the number of array elements reaches 60. The reason for performance degradation when utilizing fewer elements is that the reduction in array size would broaden the main lobe in the corresponding MUSIC spectrum, i.e., making the peak difficult to detect, which significantly degrades the resolution and accuracy of DoA estimation. As a result, larger UAV trajectory sizes yield lower DoA estimation errors, which is consistent with conventional multi-antenna array theory, i.e., physically larger array offers better resolution and improved DoA estimation performance. Therefore, increasing the size of the UAV trajectory while maintaining the far-field regime is a simple strategy to improve the resolution of the proposed system in real-world applications. However, larger trajectories also lead to higher flying time, which caused an interesting trade-off. While the maximum UAV velocity is limited by the spatial aliasing criterion in Eq (3.20), we suggest increasing the UAV velocities to complete their movement in seconds.

5.4 Conclusion

In this chapter, we proved the feasibility of the virtual array concept in UAV-based scenarios through extensive simulations. The problem of interest is to provide high-resolution DoA estimation of a source signal in both the azimuth and elevation planes by creating a virtual array with a single UAV platform. The major difficulty of DoA estimation in 3D space is to estimate AOA and EOA simultaneously, which requires nonlinear UAV trajectories, i.e., creates a 2D virtual antenna array. As the system expands to a higher dimension, extra modifications are also made for the two LO frequency offset compensation methods. The performance of these modified methods and other parameters that may affect the accuracy of the DoA estimates were also evaluated via simulations.

By analyzing the extensive simulation results, we have revealed several characteristics of the UAV-based virtual array system; some design strategies are also provided for practical applications. First of all, as angular spreads at the UAV platform are limited, the system provides good DoA estimation accuracy. The accuracy can be further improved by applying better LO quality configurations. Secondly, both the SAS method and the joint estimation method can be used to solve the phase distortion problem caused by the LO frequency offset. The performance of these two methods is related to the movement time of the UAV. The joint estimation provides more robust accuracy when the movement time of the UAV exceeds 5 seconds. Next, the performance of the proposed estimator improves as the SNR increases, until it reaches a certain threshold (around 15 dB). Finally, simulation results have verified that the proposed method achieves a better accuracy in larger 2D UAV trajectories. Therefore, when implementing the virtual array system, larger trajectories in a 2D plane are more recommended, while keeping the flight time of the UAV short. The advantages and drawbacks of each parameter of interest are summarized in Table 5.3.

Table 5.3: Discussions of Parameter of Interest

Parameters	Description	Recommendations for UAV at 80 m
Local Oscillator Qualities	Poor LO quality will cause significant frequency offset and degrade the estimator	Implement OCXOs on UAV receivers to ensure a reasonable accuracy
Duration of UAV movements	Long UAV movement time will cause the LO frequency offset drifts and cannot be treated as a constant	Keep the UAV movement below 5s is recommended; Apply the joint estimation for longer UAV movement
SNR Level	Low SNR level will degrade the MUSIC algorithm	Keep the SNR level higher than 15 dB at least
Shape of Trajectories	Perform 2D trajectories for 2D DoA estimation and remove the azimuth ambiguity	Trajectories should have a reasonable size (at least 1.5 m) on both axis in a 2D plane
Size of Trajectories	Larger trajectories lead to better resolution in DoA estimation, also requires higher movement time	The 2D Trajectory should longer than 3m to ensure the accuracy; The maximum length is limited by the far-field constraints and the spatial aliasing criterion
Frequency Offset Compensation Methods	The SAS method is straightforward but requires the UAV to standstill before moving; the joint estimation method provides stable accuracy, but consumes more computation power	Both method works fine in good LO oscillator configurations and short movement time; The joint estimation is recommended for scenarios with bad LO oscillators or long movement time

CHAPTER 6
CONCLUSION AND FUTURE WORK

6.1 Summary

This dissertation has proposed a novelty localization method for aerial platforms in UAV communication networks to localize unknown ground emitters by considering the unique air-to-ground channel characteristics and communication requirements. Different from conventional passive localization technologies that require complex time-synchronization or multi-antenna array, this proposed "virtual antenna array" method utilizes the mobility of UAV to estimate the DoA of ground targets, which is both convenient and saves a lot of payloads.

There are multiple challenges in implementing virtual array systems in UAV communication scenarios. First of all, the characteristics of the ATG channel differ significantly from conventional terrestrial channels, thus the efficiency of such DoA-based localization schemes is questionable. The second challenge comes from the phase distortion due to the LO frequency offset between the transmitter and the receiver, which is an inherent limitation of the virtual array system. The last main challenge is to reconstruct the trajectory of the receiver with high accuracy, as the position information is necessary for conventional array processing algorithms.

In response to the first challenge, we have performed detailed Ray-tracing simulations to study the spatial and temporal properties of the ATG channel. Results indicated that signals emitted from ground transmitters would reach the UAV with a very limited angular spread. Most of the received power also comes from the direction near where the transmitter is located. Therefore, DoA-based localization methods are proved to be promising in UAV communication.

For the second challenge, two methods are provided to deal with phase distortions caused by the LO frequency offsets: the SAS method and the joint estimation method. The SAS method requires the receiver to be stationary before moving and then uses the estimated LO frequency offset at stationary to compensate for phase distortion when moving. The joint estimation considers the LO frequency offset and the receiver movement as two independent sources of phase variation, then separates them by a multidimensional MUSIC spectrum search, which offers higher usage flexibility as it does not require stopping the receiver before movement. These two methods are proved to be feasible in both ground-based virtual array systems and UAV virtual array systems.

The third challenge regarding trajectory reconstruction is addressed by using inertial sensors found in many modern electronic devices. Relative positions of the receiver are calculated through dead-reckoning integration algorithms implemented by a nonlinear Kalman filter. By performing a comprehensive nonlinear observability analysis of the system, we have also proved that, even though the system is unobservable without knowing the initial velocity, the DoA can still be estimated by measuring accelerations only. On the other hand, the observability analysis also provides detailed guidelines to design feasible and efficient receiver trajectories, which significantly improved the robustness of the proposed system.

We have validated the proposed virtual array systems by conducting experiments on a software-defined radio testbed. The trajectories are reconstructed using measurements from inertial sensors. Phase distortions due to the LO frequency shift are solved by using the SAS method and the joint estimation method, respectively. The designed proof of concept provides satisfying DoA estimation accuracy in the presence of significant hardware biases.

Finally, since the feasibility and robustness of the proposed virtual array in the ground channel have been proved, we started to apply the system to UAV communication scenarios. As the elevation angle needs to be taken into account for localization in 3D space, both the signal model and the LO frequency offset compensation methods are expanded to a higher dimension. In the end, the performance of the virtual array system in UAV communication

scenarios is evaluated through detailed simulations. Consistent with our conclusions from the ray-tracing simulations, i.e., the ATG channel is beneficial for DOA-based localization approaches, the virtual array system provides excellent estimation accuracy in UAV communication scenarios. We have also provided many designing strategies when implementing the proposed system in real-world UAV communication scenarios by evaluating the simulation results.

In summary, the proposed virtual array system is an alternative for conventional DoA estimation technologies by dispensing with cumbersome and expensive multi-antenna arrays, which simultaneously reduces the cost and increases the practicability of conventional direction finding systems. Therefore, the virtual array system has great potential in applications with high cost or form-factor constraints, especially for UAV platforms with great mobility and payload limitations.

6.2 Future Directions

During this research, we have discovered many interesting questions and research directions. Recommended topics for future directions on UAV virtual array systems to follow up on the work in this thesis are provided in the following.

The first exciting direction is to design a proof-of-concept prototype for the UAV virtual array system and to test its performance in real test flights. We have already done some prior work on this subject: the UAV virtual array is built by installing a USRP E310 SDR receiver module on a DJI Matrix-100 platform; the transmitter is consists of a USRP B205 and a host computer. The UAV receiver converts the received RF signal and the IMU measurements into a data file, then transmits the data file to the host computer through a portable hotspot. By performing some prior flight tests, we found that due to the excellent visibility between the UAV and the satellite, the UAV-embedded GPS sensors provide accurate coordinate measurements. In this case, we are able to design a trajectory reconstruction method by applying data fusion from the various sensors, i.e., reset the IMU

position estimate periodically with an absolute position estimate from the GPS to alleviate accumulated bias in conventional dead reckoning methods. However, we also found that several new challenges emerged. Firstly, the UAV platform is subject to some mechanical vibrations in flight, and these vibrations will interfere with the IMU measurements. In addition, the three radio signals in the virtual array system (the message signal, the remote control signal, and the hotspot signal) all operate in the same 2.4 GHz frequency band, which may cause mutual interference.

Another direction for research is to re-examine the nonlinear observability analysis result that motivates the possibility to estimate DoA by measuring accelerations only. As the virtual array model expands to a higher dimension in UAV communications, its observability properties may also change and provide more information to be investigated, for example, a guideline to design efficient 2D UAV trajectories.

One additional direction to explore is the application of the "virtual MIMO array" to improve the performance of the DoA estimation system. Instead of using a single antenna, the UAV carries multiple antennas to create a mixed real-virtual antenna array. The difficulty lies in estimating both positions and orientations of the UAV, to identify phase shifts between different embedded antennas. Although magnetometers provide some solutions for orientation estimation, their performance also suffers heavily from the influence of electromagnetic fields. Another possible solution is to use the polarization of the received packet to track the orientation of the receiver.

In addition, it is also exciting to develop more localization technologies for UAV-based communication networks by applying other parameters than DoA measurements. In particular, RSS-based methods are promising when the mobility of UAVs can be exploited. For example, the UAV rotates once to make an RSS estimate, then flies to the direction with the strongest transmit power. After a few iterations and rotates, the UAV should move to a better serving position.

BIBLIOGRAPHY

[1] Y. Zeng, Q. Wu, and R. Zhang, "Accessing from the sky: A tutorial on uav communications for 5g and beyond," *Proceedings of the IEEE*, vol. 107, no. 12, pp. 2327–2375, 2019.

[2] H. Shakhatreh, A. H. Sawalmeh, A. Al-Fuqaha, Z. Dou, E. Almaita, I. Khalil, N. S. Othman, A. Khreishah, and M. Guizani, "Unmanned aerial vehicles (uavs): A survey on civil applications and key research challenges," *Ieee Access*, vol. 7, pp. 48 572–48 634, 2019.

[3] K. Namuduri, S. Chaumette, J. H. Kim, and J. P. Sterbenz, *UAV networks and communications*. Cambridge University Press, 2017.

[4] D. Mishra and E. Natalizio, "A survey on cellular-connected uavs: Design challenges, enabling 5g/b5g innovations, and experimental advancements," *Computer Networks*, vol. 182, p. 107 451, 2020.

[5] Y. Zeng, J. Lyu, and R. Zhang, "Cellular-connected uav: Potential, challenges, and promising technologies," *IEEE Wireless Communications*, vol. 26, no. 1, pp. 120–127, 2018.

[6] N. Hosseini, H. Jamal, J. Haque, T. Magesacher, and D. W. Matolak, "Uav command and control, navigation and surveillance: A review of potential 5g and satellite systems," in *2019 IEEE Aerospace Conference*, IEEE, 2019, pp. 1–10.

[7] R. J. Kerczewski, J. D. Wilson, and W. D. Bishop, "Frequency spectrum for integration of unmanned aircraft," in *2013 IEEE AIAA 32nd Digital Avionics Systems Conference (DASC)*, IEEE, 2013, p. 51.

[8] R. Kerczewski, J. Wilson, and W. Bishop, "Assessing spectrum compatibility for beyond-line-of-sight uas control and non-payload communications," in *2014 Integrated Communications, Navigation and Surveillance Conference (ICNS) Conference Proceedings*, IEEE, 2014, K2–1.

[9] M. Zolanvari, R. Jain, and T. Salman, "Potential data link candidates for civilian unmanned aircraft systems: A survey," *IEEE Communications Surveys & Tutorials*, vol. 22, no. 1, pp. 292–319, 2020.

[10] M. A. Khan, A. Safi, I. M. Qureshi, and I. U. Khan, "Flying ad-hoc networks (fanets): A review of communication architectures, and routing protocols," in *2017 First International Conference on Latest trends in Electrical Engineering and Computing Technologies (INTELLECT)*, IEEE, 2017, pp. 1–9.

[11] M. Azari, "Wireless communications with unmanned aerial vehicles," PhD thesis, Katholieke Universiteit Leuven, 2019.

[12] G. Geraci, A. Garcia-Rodriguez, and L. G. Giordano, "Understanding uav cellular communications: From existing networks to massive mimo," *IEEE Access*, vol. 6, pp. 67 853–67 865, 2018.

[13] Y. Zeng, R. Zhang, and T. J. Lim, "Wireless communications with unmanned aerial vehicles: Opportunities and challenges," *IEEE Communications Magazine*, vol. 54, no. 5, pp. 36–42, 2016.

[14] M. Mozaffari, W. Saad, M. Bennis, Y.-H. Nam, and M. Debbah, "A tutorial on uavs for wireless networks: Applications, challenges, and open problems," *IEEE communications surveys & tutorials*, vol. 21, no. 3, pp. 2334–2360, 2019.

[15] V. Sharma, M. Bennis, and R. Kumar, "Uav-assisted heterogeneous networks for capacity enhancement," *IEEE Communications Letters*, vol. 20, no. 6, pp. 1207–1210, 2016.

[16] A. A. Khuwaja, Y. Chen, N. Zhao, M.-S. Alouini, and P. Dobbins, "A survey of channel modeling for uav communications," *IEEE Communications Surveys & Tutorials*, vol. 20, no. 4, pp. 2804–2821, 2018.

[17] G. T. 21.917, "5g enhancement for uavs," Tech. Rep., 2021.

[18] G. T. 38.821, "Solutions for nr to support non-terrestrial networks," Tech. Rep., 2020.

[19] M. M. Azari, F. Rosas, and S. Pollin, "Cellular connectivity for uavs: Network modeling, performance analysis, and design guidelines," *IEEE Transactions on Wireless Communications*, vol. 18, no. 7, pp. 3366–3381, 2019.

[20] T. L. Marzetta, "Noncooperative cellular wireless with unlimited numbers of base station antennas," *IEEE transactions on wireless communications*, vol. 9, no. 11, pp. 3590–3600, 2010.

[21] E. Vinogradov, H. Sallouha, S. De Bast, M. M. Azari, and S. Pollin, "Tutorial on uav: A blue sky view on wireless communication," *arXiv preprint arXiv:1901.02306*, 2019.

[22] Y. Zeng, R. Zhang, and T. J. Lim, "Throughput maximization for uav-enabled mobile relaying systems," *IEEE Transactions on communications*, vol. 64, no. 12, pp. 4983–4996, 2016.

[23] X. Lin, V. Yajnanarayana, S. D. Muruganathan, S. Gao, H. Asplund, H.-L. Maattanen, M. Bergstrom, S. Euler, and Y.-P. E. Wang, "The sky is not the limit: Lte for unmanned aerial vehicles," *IEEE Communications Magazine*, vol. 56, no. 4, pp. 204–210, 2018.

[24] B. Li, Z. Fei, and Y. Zhang, "Uav communications for 5g and beyond: Recent advances and future trends," *IEEE Internet of Things Journal*, vol. 6, no. 2, pp. 2241–2263, 2018.

[25] A. Fotouhi, H. Qiang, M. Ding, M. Hassan, L. G. Giordano, A. Garcia-Rodriguez, and J. Yuan, "Survey on uav cellular communications: Practical aspects, standardization advancements, regulation, and security challenges," *IEEE Communications Surveys & Tutorials*, vol. 21, no. 4, pp. 3417–3442, 2019.

[26] Y. Zeng and R. Zhang, "Energy-efficient uav communication with trajectory optimization," *IEEE Transactions on Wireless Communications*, vol. 16, no. 6, pp. 3747–3760, 2017.

[27] A. Wang, X. Ji, D. Wu, X. Bai, N. Ding, J. Pang, S. Chen, X. Chen, and D. Fang, "Guideloc: Uav-assisted multitarget localization system for disaster rescue," *Mobile Information Systems*, vol. 2017, 2017.

[28] R. Zekavat and R. M. Buehrer, *Handbook of position location: Theory, practice and advances*. John Wiley & Sons, 2011, vol. 27.

[29] F. Zafari, A. Gkelias, and K. K. Leung, "A survey of indoor localization systems and technologies," *IEEE Communications Surveys & Tutorials*, vol. 21, no. 3, pp. 2568–2599, 2019.

[30] Y. Kang, Q. Wang, J. Wang, and R. Chen, "A high-accuracy toa-based localization method without time synchronization in a three-dimensional space," *IEEE Transactions on Industrial Informatics*, vol. 15, no. 1, pp. 173–182, 2018.

[31] E. Xu, Z. Ding, and S. Dasgupta, "Source localization in wireless sensor networks from signal time-of-arrival measurements," *IEEE Transactions on Signal Processing*, vol. 59, no. 6, pp. 2887–2897, 2011.

[32] T. Engin and F. Benjamin, *Classical and modern direction-of-arrival estimation*. Academic Press, 2009.

[33] S. Tomic, M. Beko, and R. Dinis, "Rss-based localization in wireless sensor networks using convex relaxation: Noncooperative and cooperative schemes," *IEEE Transactions on Vehicular Technology*, vol. 64, no. 5, pp. 2037–2050, 2014.

[34] Z. Chen, G. Gokeda, and Y. Yu, *Introduction to Direction-of-arrival Estimation*. Artech House, 2010.

[35] D. J. Pack and G. W. York, "Developing a control architecture for multiple unmanned aerial vehicles to search and localize rf time-varying mobile targets: Part i," in *Proceedings of the 2005 IEEE international conference on robotics and automation*, IEEE, 2005, pp. 3954–3959.

[36] G. M. Hoffmann, *Autonomy for sensor-rich vehicles: Interaction between sensing and control actions*. Stanford University, 2008.

[37] J. T. Isaacs, F. Quitin, L. R. G. Carrillo, U. Madhow, and J. P. Hespanha, "Quadrotor control for rf source localization and tracking," in *2014 International Conference on Unmanned Aircraft Systems (ICUAS)*, IEEE, 2014, pp. 244–252.

[38] G. Duchene and F. Quitin, "Detecting the source of an rf signal with a transceiver-equipped uav," in *14th International Symposium on Wireless Communication Systems (ISWCS 2017), 2017*, 2017.

[39] P Soriano, F Caballero, A Ollero, and C. A. de Tecnologıas Aeroespaciales, "Rf-based particle filter localization for wildlife tracking by using an uav," in *Proceedings of the 40th International Symposium on Robotics, Barcelona, Spain*, 2009, pp. 10–13.

[40] A. Posch and S. Sukkarieh, "Uav based search for a radio tagged animal using particle filters," in *Australasian conference on Robotics and Automation (ACRA)*, 2009.

[41] H. Sallouha, M. M. Azari, A. Chiumento, and S. Pollin, "Aerial anchors positioning for reliable rss-based outdoor localization in urban environments," *IEEE Wireless Communications Letters*, vol. 7, no. 3, pp. 376–379, 2017.

[42] Y. Li, F. Shu, B. Shi, X. Cheng, Y. Song, and J. Wang, "Enhanced rss-based uav localization via trajectory and multi-base stations," *IEEE Communications Letters*, 2021.

[43] S. A. A. Shahidian and H. Soltanizadeh, "Optimal trajectories for two uavs in localization of multiple rf sources," *Transactions of the Institute of Measurement and Control*, vol. 38, no. 8, pp. 908–916, 2016.

[44] A. Shahidian and H. Soltanizadeh, "Path planning for two unmanned aerial vehicles in passive localization of radio sources," *Aerospace Science and Technology*, vol. 58, pp. 189–196, 2016.

[45] H. Jee and J. Lim, "Efficient least squares regression algorithm for autonomous maneuvering uav system," *Journal of Computers*, vol. 29, no. 6, pp. 140–147, 2018.

[46] A. Danjo, Y. Watase, and S. Hara, "A theoretical error analysis on indoor toa localization scheme using unmanned aerial vehicles," in *2015 IEEE 81st Vehicular Technology Conference (VTC Spring)*, IEEE, 2015, pp. 1–5.

[47] S. Lee, W. Lee, and K. You, "Tdoa based uav localization using dual-ekf algorithm," in *International Conference on Control and Automation*, Springer, 2009, pp. 47–54.

[48] J. Tiemann and C. Wietfeld, "Scalable and precise multi-uav indoor navigation using tdoa-based uwb localization," in *2017 international conference on indoor positioning and indoor navigation (IPIN)*, IEEE, 2017, pp. 1–7.

[49] W. Wang, P. Bai, X. Liang, J. Zhang, and L. He, "Performance analysis for tdoa localization using uavs with flight disturbances," in *2017 20th International Conference on Information Fusion (Fusion)*, IEEE, 2017, pp. 1–6.

[50] D. Šoštarić and G. Mester, "Drone localization using ultrasonic tdoa and rss signal: Integration of the inverse method of a particle filter," *FME Transactions*, vol. 48, no. 1, pp. 21–30, 2020.

[51] K. Dogancay, "Uav path planning for passive emitter localization," *IEEE Transactions on Aerospace and Electronic systems*, vol. 48, no. 2, pp. 1150–1166, 2012.

[52] W. Zhonghai, C. Genshe, B. Erik, P. Khanh, and L. Robert, "Jamming emitter localization with multiple uavs equipped with smart antennas," in *Automatic Target Recognition XX; Acquisition, Tracking, Pointing, and Laser Systems Technologies XXIV; and Optical Pattern Recognition XXI*, International Society for Optics and Photonics, vol. 7696, 2010, p. 769 607.

[53] P. Scerri, R. Glinton, S. Owens, D. Scerri, and K. Sycara, "Geolocation of rf emitters by many uavs," in *AIAA Infotech@ Aerospace 2007 Conference and Exhibit*, 2007, p. 2858.

[54] T. Zhao, C. Luo, J. Zhou, D. Guo, N. Chen, and P. Casaseca-de-la Higuera, "Doa prediction based beamforming with low training overhead for highly-mobile uav communication with cellular networks," *Applied Sciences*, vol. 10, no. 13, p. 4420, 2020.

[55] P. Alinezhad, S. R. Seydnejad, and D. Abbasi-Moghadam, "Doa estimation in conformal arrays based on the nested array principles," *Digital Signal Processing*, vol. 50, pp. 191–202, 2016.

[56] X. Lin, X. Zhang, L. He, and W. Zheng, "Multiple emitters localization by uav with nested linear array: System scheme and 2d-doa estimation algorithm," *China Communications*, vol. 17, no. 3, pp. 117–130, 2020.

[57] M. A. Diop, K. Cheikhrouhou, and S. Affes, "Impact of angular spread and doa estimation on the performance of wideband cdma array-receivers," pp. 1–5, 2006.

[58] D. Astely and B. Ottersten, "The effects of local scattering on direction of arrival estimation with music," *IEEE transactions on Signal Processing*, vol. 47, no. 12, pp. 3220–3234, 1999.

[59] S. J. Nawaz, S. Wyne, K. B. Baltzis, S. M. Gulfam, and K. Cumanan, "A tunable 3-d statistical channel model for spatio-temporal characteristics of wireless communication networks," *Transactions on Emerging Telecommunications Technologies*, vol. 28, no. 12, e3213, 2017.

[60] G. T. 38.913, "Technical specification group radio access network; study on scenarios and requirements for next generation access technologies;(release 14)," Tech. Rep., 2016.

[61] R. Verdone and A. Zanella, *Pervasive mobile and ambient wireless communications: COST action 2100*. Springer Science & Business Media, 2012.

[62] J. Meinilä, P. Kyösti, T. Jämsä, and L. Hentilä, "Winner ii channel models," 2009.

[63] G. T. 38.913, "Study on channel model for frequencies from 0.5 to 100 ghz," Tech. Rep., 2016.

[64] R. Zhang, X. Lu, J. Zhao, L. Cai, and J. Wang, "Measurement and modeling of angular spreads of three-dimensional urban street radio channels," *IEEE Transactions on Vehicular Technology*, vol. 66, no. 5, pp. 3555–3570, 2016.

[65] D. He, B. Ai, K. Guan, L. Wang, Z. Zhong, and T. Kürner, "The design and applications of high-performance ray-tracing simulation platform for 5g and beyond wireless communications: A tutorial," *IEEE Communications Surveys & Tutorials*, vol. 21, no. 1, pp. 10–27, 2018.

[66] D. He, B Ai, K Guan, L Wang, Z Zhong, and T Kuerner, "High-performance ray-tracing simulation platform and its application to mobile communications," *IEEE Communications Surveys & Tutorials*, 2017.

[67] K. Guan, X. Lin, D. He, B. Ai, Z. Zhong, Z. Zhao, D. Miao, H. Guan, and T. Kürner, "Scenario modules and ray-tracing simulations of millimeter wave and terahertz channels for smart rail mobility," in *2017 11th European Conference on Antennas and Propagation (EUCAP)*, IEEE, 2017, pp. 113–117.

[68] K. Guan, B. Ai, B. Peng, D. He, G. Li, J. Yang, Z. Zhong, and T. Kurner, "Towards realistic high-speed train channels at 5g millimeter-wave band - part i: Paradigm, significance analysis, and scenario reconstruction," *IEEE Transactions on Vehicular Technology*, vol. 67, no. 10, pp. 9112–9128, 2018.

[69] K. Guan, B. Ai, B. Peng, D. He, G. Li, J. Yang, Z. Zhong, and T. Kürner, "Towards realistic high-speed train channels at 5g millimeter-wave band - part ii: Case study for paradigm implementation," *IEEE Transactions on Vehicular Technology*, vol. 67, no. 10, pp. 9129–9144, 2018.

[70] ITU, "Propagation data and prediction methods for the design of terrestrial broadband millimetric radio access systems," International Telecommunication Union, Tech. Rep., 2003.

[71] A. Goldsmith, *Wireless communications*. Cambridge university press, 2005.

[72] J. Burkardt, "The truncated normal distribution," Florida State University, Tech. Rep., 2014.

[73] J. Cheng, K. Guan, and F. Quitin, "Wireless channel characteristics for uav-based radio access networks in urban environments," in *2019 IEEE Vehicular Technology Conference (VTC 2019 fall)*, IEEE, 2019.

[74] L. J. Greenstein, V. Erceg, Y. S. Yeh, and M. V. Clark, "A new path-gain/delay-spread propagation model for digital cellular channels," *IEEE Transactions on Vehicular Technology*, vol. 46, no. 2, pp. 477–485, 1997.

[75] C. Cheon, G. Liang, and H. L. Bertoni, "Simulating radio channel statistics for different building environments," *IEEE Journal on Selected Areas in Communications*, vol. 19, no. 11, pp. 2191–2200, 2001.

[76] D. Cassioli, L. A. Annoni, and S. Piersanti, "Characterization of path loss and delay spread of 60-ghz uwb channels vs. frequency," in *2013 IEEE International Conference on Communications (ICC)*, IEEE, 2013, pp. 5153–5157.

[77] D. Macii, A. Colombo, P. Pivato, and D. Fontanelli, "A data fusion technique for wireless ranging performance improvement," *IEEE Transactions on Instrumentation and Measurement*, vol. 62, no. 1, pp. 27–37, 2012.

[78] M. A. Yaqoob, F. Tufvesson, A. Mannesson, and B. Bernhardsson, "Direction of arrival estimation with arbitrary virtual antenna arrays using low cost inertial measurement units," in *2013 IEEE International Conference on Communications Workshops (ICC)*, IEEE, 2013, pp. 79–83.

[79] A. Mannesson, M. A. Yaqoob, B. Bernhardsson, and F. Tufvesson, "Tightly coupled positioning and multipath radio channel tracking," *IEEE Transactions on Aerospace and Electronic Systems*, vol. 52, no. 4, pp. 1522–1535, 2016.

[80] F. Quitin, P. De Doncker, F. Horlin, and W. P. Tay, "Virtual multiantenna array for estimating the direction of a transmitter: System, bounds, and experimental results," *IEEE Transactions on Vehicular Technology*, vol. 67, no. 2, pp. 1510–1520, 2017.

[81] F. Comblet, A. Khenchaf, A. Baussard, and F. Pellen, "Bistatic synthetic aperture radar imaging: Theory, simulations, and validations," *IEEE Transactions on Antennas and Propagation*, vol. 54, no. 11, pp. 3529–3540, 2006.

[82] J. Fortuny and A. J. Sieber, "Three-dimensional synthetic aperture radar imaging of a fir tree: First results," *IEEE Transactions on Geoscience and Remote Sensing*, vol. 37, no. 2, pp. 1006–1014, 1999.

[83] A. G. Siamarou and M. Al-Nuaimi, "A wideband frequency-domain channel-sounding system and delay-spread measurements at the license-free 57-to 64-ghz band," *IEEE Transactions on Instrumentation and Measurement*, vol. 59, no. 3, pp. 519–526, 2010.

[84] S. Ranvier, J. Kivinen, and P. Vainikainen, "Millimeter-wave mimo radio channel sounder," *IEEE transactions on Instrumentation and Measurement*, vol. 56, no. 3, pp. 1018–1024, 2007.

[85] S. Wyne, K. Haneda, S. Ranvier, F. Tufvesson, and A. F. Molisch, "Beamforming effects on measured mm-wave channel characteristics," *IEEE Transactions on Wireless Communications*, vol. 10, no. 11, pp. 3553–3559, 2011.

[86] M. A. Yaqoob, A. Mannesson, N. R. Butt, and F. Tufvesson, "Source localization using virtual antenna arrays," in *2015 International Conference on Localization and GNSS (ICL-GNSS)*, IEEE, 2015, pp. 1–6.

[87] A. Paulraj, B. Ottersten, R Roy, A Swindlehurst, G. Xu, and T. Kailath, "16 subspace methods for directions-of-arrival estimation," vol. 10, Elsevier, 1993, pp. 693–739.

[88] R. O. Schmidt, *A signal subspace approach to multiple emitter location and spectral estimation*. Stanford University, 1982.

[89] A. Manikas, *Differential geometry in array processing*. Imperial College Press, 2004.

[90] H. Abeida and J.-P. Delmas, "Music-like estimation of direction of arrival for noncircular sources," *IEEE Transactions on Signal Processing*, vol. 54, no. 7, pp. 2678–2690, 2006.

[91] J. Cheng, K. Guan, and F. Quitin, "Direction of arrival estimation with virtual antenna array: Observability analysis, local oscillator frequency offset compensation, and experimental results," *IEEE Transactions on Instrumentation and Measurement*, 2021.

[92] M. H. Nassralla, M. M. Mansour, and L. M. Jalloul, "A low-complexity detection algorithm for the primary synchronization signal in lte," *IEEE Transactions on Vehicular Technology*, vol. 65, no. 10, pp. 8751–8757, 2015.

[93] V. Magnago, L. Palopoli, A. Buffi, B. Tellini, A. Motroni, P. Nepa, D. Macii, and D. Fontanelli, "Ranging-free uhf-rfid robot positioning through phase measurements

of passive tags," *IEEE Transactions on Instrumentation and Measurement*, vol. 69, no. 5, pp. 2408–2418, 2019.

[94] C. Zucca and P. Tavella, "The clock model and its relationship with the allan and related variances," *IEEE transactions on ultrasonics, ferroelectrics, and frequency control*, vol. 52, no. 2, pp. 289–296, 2005.

[95] P. Zhang, J. Gu, E. E. Milios, and P. Huynh, "Navigation with imu/gps/digital compass with unscented kalman filter," in *IEEE International Conference Mechatronics and Automation, 2005*, IEEE, vol. 3, 2005, pp. 1497–1502.

[96] H. Zhao and Z. Wang, "Motion measurement using inertial sensors, ultrasonic sensors, and magnetometers with extended kalman filter for data fusion," *IEEE Sensors Journal*, vol. 12, no. 5, pp. 943–953, 2011.

[97] D. Gingras, "An overview of positioning and data fusion techniques applied to land vehicle navigation systems," *Automotive Informatics and Communicative Systems: Principles in Vehicular Networks and Data Exchange*, pp. 219–246, 2009.

[98] P. Bello, "Characterization of randomly time-variant linear channels," *IEEE transactions on Communications Systems*, vol. 11, no. 4, pp. 360–393, 1963.

[99] R. Kohno, "Spatial and temporal communication theory using adaptive antenna array," *IEEE personal communications*, vol. 5, no. 1, pp. 28–35, 1998.

[100] E. Dahlman, S. Parkvall, J. Skold, and P. Beming, *3G evolution: HSPA and LTE for mobile broadband*. Academic press, 2010.

[101] C. Oestges and F. Quitin, *Inclusive Radio Communications for 5G and Beyond*. Academic Press, 2021.

[102] K Nirmal, A. Sreejith, J. Mathew, M. Sarpotdar, A. Suresh, A. Prakash, M. Safonova, and J. Murthy, "Noise modeling and analysis of an imu-based attitude sensor: Improvement of performance by filtering and sensor fusion," in *Advances in*

Optical and Mechanical Technologies for Telescopes and Instrumentation II, International Society for Optics and Photonics, vol. 9912, 2016, 99126W.

[103] D. Tedaldi, A. Pretto, and E. Menegatti, "A robust and easy to implement method for imu calibration without external equipments," in *2014 IEEE International Conference on Robotics and Automation (ICRA)*, IEEE, 2014, pp. 3042–3049.

[104] M. S. Grewal, A. P. Andrews, and C. G. Bartone, *Global navigation satellite systems, inertial navigation, and integration*. John Wiley & Sons, 2020.

[105] R. E. Kalman, "A new approach to linear filtering and prediction problems," 1960.

[106] L. A. McGee and S. F. Schmidt, "Discovery of the kalman filter as a practical tool for aerospace and industry," 1985.

[107] M. Hoshiya and E. Saito, "Structural identification by extended kalman filter," *Journal of engineering mechanics*, vol. 110, no. 12, pp. 1757–1770, 1984.

[108] S. J. Julier and J. K. Uhlmann, "New extension of the kalman filter to nonlinear systems," in *Signal processing, sensor fusion, and target recognition VI*, International Society for Optics and Photonics, vol. 3068, 1997, pp. 182–193.

[109] R. Van Der Merwe, "Sigma-point kalman filters for probabilistic inference in dynamic state-space models," PhD thesis, 2004.

[110] R. Van Der Merwe, E. Wan, and S. Julier, "Sigma-point kalman filters for nonlinear estimation and sensor-fusion: Applications to integrated navigation," in *Aiaa guidance, navigation, and control conference and exhibit*, 2004, p. 5120.

[111] Y. Kim and H. Bang, "Introduction to kalman filter and its applications," *Introduction and Implementations of the Kalman Filter, F. Govaers, Ed. IntechOpen*, 2019.

[112] F. M. Mirzaei and S. I. Roumeliotis, "A kalman filter-based algorithm for imu-camera calibration: Observability analysis and performance evaluation," *IEEE transactions on robotics*, vol. 24, no. 5, pp. 1143–1156, 2008.

[113] E. A. Wan and R. Van Der Merwe, "The unscented kalman filter for nonlinear estimation," in *Proceedings of the IEEE 2000 Adaptive Systems for Signal Processing, Communications, and Control Symposium (Cat. No. 00EX373)*, Ieee, 2000, pp. 153–158.

[114] M. Rhudy and Y. Gu, "Understanding nonlinear kalman filters, part ii: An implementation guide," *Interactive Robotics Letters*, pp. 1–18, 2013.

[115] M. Rhudy, Y. Gu, J. Gross, and M. R. Napolitano, "Evaluation of matrix square root operations for ukf within a uav gps/ins sensor fusion application," *International Journal of Navigation and Observation*, vol. 2011, 2011.

[116] X. Yuan, S. Yu, S. Zhang, G. Wang, and S. Liu, "Quaternion-based unscented kalman filter for accurate indoor heading estimation using wearable multi-sensor system," *Sensors*, vol. 15, pp. 10 872–10 890, 2015.

[117] J. A. Hesch, D. G. Kottas, S. L. Bowman, and S. I. Roumeliotis, "Camera-imu-based localization: Observability analysis and consistency improvement," *The International Journal of Robotics Research*, vol. 33, no. 1, pp. 182–201, 2014.

[118] J. Kaiser, A. Martinelli, F. Fontana, and D. Scaramuzza, "Simultaneous state initialization and gyroscope bias calibration in visual inertial aided navigation," *IEEE Robotics and Automation Letters*, vol. 2, no. 1, pp. 18–25, 2016.

[119] S. Hong, M. H. Lee, H.-H. Chun, S.-H. Kwon, and J. L. Speyer, "Observability of error states in gps/ins integration," *IEEE Transactions on Vehicular Technology*, vol. 54, no. 2, pp. 731–743, 2005.

[120] G Artese and A Trecroci, "Calibration of a low cost mems ins sensor for an integrated navigation system," *Int. Arch. Photogramm. Remote Sens. Spatial Inf. Sci*, pp. 877–882, 2008.

[121] S. O. Madgwick, A. J. Harrison, and R. Vaidyanathan, "Estimation of imu and marg orientation using a gradient descent algorithm," in *2011 IEEE international conference on rehabilitation robotics*, IEEE, 2011, pp. 1–7.

[122] D. Fontanelli, F. Shamsfakhr, D. Macii, and L. Palopoli, "An uncertainty-driven and observability-based state estimator for nonholonomic robots," *IEEE Transactions on Instrumentation and Measurement*, vol. 70, pp. 1–12, 2021.

[123] V. R. Marco, J. Kalkkuhl, and J. Raisch, "Ekf for simultaneous vehicle motion estimation and imu bias calibration with observability-based adaptation," in *2018 Annual American Control Conference (ACC)*, IEEE, 2018, pp. 6309–6316.

[124] R. Hermann and A. Krener, "Nonlinear controllability and observability," *IEEE Transactions on automatic control*, vol. 22, no. 5, pp. 728–740, 1977.

[125] Z. M. Kassas and T. E. Humphreys, "Observability analysis of collaborative opportunistic navigation with pseudorange measurements," *IEEE Transactions on Intelligent Transportation Systems*, vol. 15, no. 1, pp. 260–273, 2013.

[126] D. C. Woffinden and D. K. Geller, "Observability criteria for angles-only navigation," *IEEE Transactions on Aerospace and Electronic Systems*, vol. 45, no. 3, pp. 1194–1208, 2009.

[127] B. T. Hinson, "Observability-based guidance and sensor placement," PhD thesis, 2014.

[128] Y. Oshman and P. Davidson, "Optimization of observer trajectories for bearings-only target localization," *IEEE Transactions on Aerospace and Electronic Systems*, vol. 35, no. 3, pp. 892–902, 1999.

[129] E. Fogel and M. Gavish, "Nth-order dynamics target observability from angle measurements," *IEEE Transactions on Aerospace and Electronic Systems*, vol. 24, no. 3, pp. 305–308, 1988.

[130] D. Guo, M. Zhong, and D. Zhou, "Multisensor data-fusion-based approach to airspeed measurement fault detection for unmanned aerial vehicles," *IEEE Transactions on Instrumentation and Measurement*, vol. 67, no. 2, pp. 317–327, 2017.

[131] J. Jackson, J. Nielsen, T. McLain, and R. Beard, "Improving the robustness of visual-inertial extended kalman filtering," in *2019 International Conference on Robotics and Automation (ICRA)*, IEEE, 2019, pp. 4703–4709.

[132] X. Cui, K. Yu, and S. Lu, "Direction finding for transient acoustic source based on biased tdoa measurement," *IEEE Transactions on Instrumentation and Measurement*, vol. 65, no. 11, pp. 2442–2453, 2016.

[133] D. R. Brown, P. Bidigare, and U. Madhow, "Receiver-coordinated distributed transmit beamforming with kinematic tracking," in *2012 IEEE International Conference on Acoustics, Speech and Signal Processing (ICASSP)*, IEEE, 2012, pp. 5209–5212.

[134] F. Quitin, M. M. U. Rahman, R. Mudumbai, and U. Madhow, "A scalable architecture for distributed transmit beamforming with commodity radios: Design and proof of concept," *IEEE Transactions on Wireless Communications*, vol. 12, no. 3, pp. 1418–1428, 2013.

[135] N. Tayem and H. M. Kwon, "L-shape 2-dimensional arrival angle estimation with propagator method," *IEEE transactions on antennas and propagation*, vol. 53, no. 5, pp. 1622–1630, 2005.

[136] S. Liu, J. Zhao, and Y. Zhang, "2d doa estimation with a two-parallel array consisting of two uniform large-spacing linear arrays," *International Journal of Antennas and Propagation*, vol. 2020, 2020.

[137] S. Liu, L. Yang, D. Li, and H. Cao, "Subspace extension algorithm for 2d doa estimation with l-shaped sparse array," *Multidimensional Systems and Signal Processing*, vol. 28, no. 1, pp. 315–327, 2017.

[138] J. Cheng, K. Guan, and F. Quitin, "Virtual multiantenna array for estimating the doa of a transmitter in uav-assisted networks," in *2020 IEEE 31st Annual International Symposium on Personal, Indoor and Mobile Radio Communications*, 2020, pp. 1–6.

[139] D. Rahamim, J. Tabrikian, and R. Shavit, "Source localization using vector sensor array in a multipath environment," *IEEE Transactions on Signal Processing*, vol. 52, no. 11, pp. 3096–3103, 2004.

PUBLICATION LIST

Journal Publications

- **Cheng, Jianqiao**, Ke Guan, and Francois Quitin. "Direction of Arrival Estimation with Virtual Antenna Array: Observability Analysis, Local Oscillator Frequency Offset Compensation, and Experimental Results." *IEEE Transactions on Instrumentation and Measurement* (2021).

Conference Publications

- **Cheng, Jianqiao**, Ke Guan, and Franois Quitin. "A High-Accuracy DoA-Based Localization Method: UAV Virtual Multiantenna Array." *The Seventeenth International Conference on Wireless and Mobile Communications (ICWMC 2021)*. 2021.

- **Cheng, Jianqiao**, Ke Guan, and Franois Quitin. "Virtual Multiantenna Array for Estimating the DOA of a Transmitter in UAV-assisted Networks." *2020 IEEE 31st Annual International Symposium on Personal, Indoor and Mobile Radio Communications*. IEEE, 2020.

- **Cheng, Jianqiao**, Ke Guan, and Franois Quitin. "Wireless Channel Characteristics for UAV-Based Radio Access Networks in Urban Environments," *2019 IEEE 90th Vehicular Technology Conference (VTC2019-Fall)*. IEEE, 2019.

- **Cheng, Jianqiao**, Ke Guan, and Franois Quitin. "Virtual Multiantenna Array for Estimating the Direction of a Transmitter in UAV-based Networks," *2019 Symposium on Information Theory and Signal Processing in the Benelux (SITB 2019)*. 2019.

- **Cheng, Jianqiao**, Ke Guan, and Franois Quitin. "Wireless Channel Modeling for Low-altitude UAV Networks in Urban Environments," *2018 Symposium on Information Theory and Signal Processing in the Benelux (SITB 2018)*. 2018.

- Mezhoud, Sami, **Cheng, Jianqiao**, Ke Guan, and Franois Quitin. "Evaluation of An Efficient Control Strategy for A Multi-user UAV-based Wireless Network," *25th Symposium on Communications and Vehicular Technology in the Benelux (SCVT 2018)*. 2018.

COST (European Cooperation in Science and Technology) - Temporary Documents

- **Cheng, Jianqiao**, Ke Guan, and Franois Quitin. "Observability Analysis of Virtual Multiantenna Array Localization Method," *EURO-COST CA15104 TD(20)13025*. London, UK, September, 2020.

- Mezhoud, Sami, **Cheng, Jianqiao**, Ke Guan, and Franois Quitin. "Ground user localization in UAV-based wireless networks," *EURO-COST CA15104 TD(19)10036*. Oulu, Finland, May, 2019.

Academic Awards

- **The Best Paper Award** in *The Seventeenth International Conference on Wireless and Mobile Communications (ICWMC 2021)*. 2021.

- **The Best Presentation Award** in *2018 Symposium on Information Theory and Signal Processing in the Benelux (SITB 2018)*. 2018.